Development of a Fast Simulation Method for Particle-Laden Fluid Interfaces and Selected Applications to Problems Involving Drops

by

Chuan Gu

A thesis submitted in partial fulfuillment
of the requirements for the degree of
Doctor of Philosophy
of
Queen Mary University of London

School of Engineering and Material Science
Queen Mary University of London

April 2018

Statement of Originality

I, Chuan Gu, confirm that the research included within this thesis is my own work or that where it has been carried out in collaboration with, or supported by others, that this is duly acknowledged below and my contribution indicated. Previously published material is also acknowledged below.

I attest that I have exercised reasonable care to ensure that the work is original, and does not to the best of my knowledge break any UK law, infringe any third partys copyright or other Intellectual Property Right, or contain any confidential material.

I accept that the College has the right to use plagiarism detection software to check the electronic version of the thesis.

I confirm that this thesis has not been previously submitted for the award of a degree by this or any other university.

Signature:

Date:

Abstract

Solid particles tend to adhere to fluid interfaces under the action of capillary force. This adsorption process is robust and has been exploited in lots of applications from stabilisation of emulsions to microfluidic fabrications. The resulting particle-laden fluid interfaces can manifest solid-like behaviours. The modification of the surface tension and the emergence of surface shear elasticity of a particle-covered drops are attributed to the particle-induced surface stress. This stress represents at the continuum level the microscopic effect of particle-particle interactions. Understanding the link between the surface stress and the particle arrangement are crucial for creating novel soft materials in the future.

A challenge remains when carrying out numerical simulations of particle-laden fluid interfaces: the large separation of scales makes the direct numerical simulations extraordinary expensive. Physical features present in the system come from both the liquid meniscus on the surface of each particle and the fluid interfaces containing thousands of particles.

Motivated by the need for a fast simulation method to study problems involving particle-laden fluid interface, this thesis presents a new numerical formulation named Fast Interface Particle Interaction (FIPI) that can be used to simulate a large number of solid particles absorbed on fluid interfaces at a moderate computational cost. The outstanding performance of this new method is attributed to the fact that particle-level phenomena are modelled with analytical or semi-empirical expressions while hydrodynamics and fluid interface morphology at larger scales are fully resolved.

Two important studies of particle-covered drops have been carried out with FIPI. In the first one a particle-covered pendant drop is simulated. The result reveals that the FIPI can successfully capture the modulation of surface tension made by absorbed particles. Moreover, the information of anisotropic surface stress is now directly available on the fluid interfaces. This capability has not been achieved previously in both experiments and simulations. The anisotropic stress emerged on the surface of a pendant drop is caused by anisotropic arrangement of the particles on the interface which in turn is induced by stretching of the interface due to gravity.

Once the surface tension of the fluid interface is reduced below zero, the Laplace pressure inside the drop becomes negative and the drop can buckle like a thin solid elastic shell under compression. In the second study, the behaviours of a particle-covered spherical drop under compression have been explored. The simulation results indicate the possibilities of particle desorption as well as fluid interface buckling. The onset of desorption is highly correlated to small-scale monolayer undulations which can greatly amplify the normal forces pushing particles out of the interface. The behaviours of a particle-covered drop under compression depend on the combination of several parameters related to the properties of the particle and the surface pressure created by the monolayer.

Acknowledgments

Firstly, I would like to express my sincere gratitude to my supervisor Dr. Lorenzo Botto, for all the guidance, patience, motivation and advice he has provided throughout four years of my Ph.D study. With his immense knowledge, he not only helped me tackle the most difficult problems in my research but also made me to think and act in a more systematic and professional way.

Besides my supervisor, I would like to thank Dr. Valeria Garbin, for providing great inspiration and advice for the most important parts of my research.

I thank my fellow groupmates and those whom I have met during my four years life at Queen Mary University of London. The time we spent together will definitely become more memorable as life goes on.

I would like to thank my parents and wife. During all these years, their unconditional supports for me to pursue my dream and career undoubtedly give me the strength and courage to overcome all the difficulties.

Table of Contents

List of Figures

List of Tables

List of Abbreviations

AB	Adam-Bashforth Method
BDF	Backward Differencing Formula
Bijels	Bicontinuous Interfacially Jammed Emulsion Gels
CH	Cahn-Hilliard Equation
CV	Control Volume
DLVO	Derjaguin, Landau, Verwey, and Overbeek
FCM	Force Coupling Method
FFT	Fast Fourier Transform
FIPI	Fast Interface Particle Interaction
IB	Immersed Boundary
LBM	Lattice Boltzmann Method
MAC	Marker-and-Cell
PDE	Partial Differential Equation
VOF	Volume of Fluid

List of Symbols

A	Surface area of drop
A_0	Initial surface area of drop
A_p	Fluid interface area occupied by a particle
A_c	Area of fluid interface within control region
a	Particle radius
Bo	Bond number
$\mathcal{C}$	Local surface curvature
Ca	Capillary number
Cn	Cahn number
d	Distance from a particle centre to fluid interface
D	Taylor deformation parameter
E_p	Packing energy of monolayer of particles
F	Free energy density in phase field
$\mathbf{F}$	Total force exerted from the surrounding fluid on a particle
$\mathbf{F}_h$	Hydrodynamic drag force exerted on a particle by surrounding fluid
$\mathbf{F}_{pi}$	Capillary force exerted on a particle by fluid interface
$\mathbf{F}_{pp}$	Interaction force exerted on a particle by surrounding particles
$\mathcal{F}$	Parameter defining the strength of particle-particle electrostatic repulsion
F_{tot}	Total free energy of the computational domain

$F_\perp$ Force perpendicular to fluid interface

$F_\parallel$ Force parallel to fluid interface

$\mathbf{f}_c$ Force density due to surface tension of bare fluid interface

f Parameter defining the adsorption strength of particles

G Boxcar filter function

K_0 Modified Bessel function of the second kind

k Boltzmann constant

k_c Stiffness constant of the particle-particle solid contact force

L Side Length of computational domain

L_c Radius of control volume sphere

l Average particle-particle distance

l_c Capillary length

M Mobility parameter in Cahn-Hilliard equation

m_p Mass of a particle

N Total number of particles

N_c Local coordination number of a particle

$\mathbf{n}_c$ Normal vector of contact line

n_c Surface number density of particles

R Drop radius

Pe Peclet number

r_c Cut-off distance of particle-particle interaction force

S Nondimensional mobility parameter

T Temperature

T_b Buckling time scale

t_d Diffusive time scale

t_c Convective time scale

t_{sim} Simulation time

$\mathbf{u}_f$	Undisturbed flow velocity at the centre of a particle
$\mathbf{u}_p$	Velocity of a particle
$\mathbf{x}_p$	Location of a particle
Γ	Work of adhesion
γ	Surface tension of bare fluid interface
γ_{eff}	Effective surface tension of particle-laden fluid interface
Δp	Effective Laplace pressure across particle-laden fluid interface
Δp_γ	Laplace pressure caused by bare fluid surface tension
Δp_p	Laplace pressure caused by particle monolayer
Δx	Computational grid size
Δt	Computational time step
ΔV	Volume of a computational cell
δ	Dirac delta function
ϵ	Parameter defining the thickness of fluid interface
θ_c	Contact angle
κ	Mean curvature of fluid interface
κ_ϕ	Curvature along azimuthal direction
κ_s	Curvature along meridional direction
λ	Parameter defining surface tension magnitude
λ_c	Characteristic wavelength of the monolayer wrinkling
μ	Viscosity of fluid
ξ	Chemical potential of phase field
Π_s	Surface pressure created by monolayer of particles
ρ	Density of fluid
$\boldsymbol{\sigma}$	Surface stress tensor
$\sigma_{\phi\phi}$	Azimuthal surface stress
σ_{ss}	Meridional surface stress

$\boldsymbol{\sigma}^D$	Deviatoric surface stress tensor
$\sigma^D_{\phi\phi}$	Deviatoric component of surface stress along azimuthal direction
σ^D_{ss}	Deviatoric component of surface stress along meridional direction
ϕ	Phase field variable
ϕ_s	surface area fraction of particles on fluid interface
Ψ	Sphericity parameter of drop

Chapter 1

Introduction

The presence of fluid interface is common in natural phenomena and industrial processes, ranging from raindrop on leaves to oil-in-water emulsion in food or health care products [6]. The dynamics of multiphase fluid is strongly influenced by surface tension effects [7]. Surface tension is a surface force acting tangentially to a fluid interface that acts to minimise the surface area. Although surface tension is an intrinsic property of the fluid interface, particles of intermediate wettability can strongly adhere to the surface of droplets or bubbles [2, 8, 9], forming a semi-solid "skin" that changes the mechanical and mass transport properties of the fluid interface. The adsorption is driven by capillary effects to minimise the total surface free energy which includes the free energies associated with the solid-fluid and fluid-fluid surfaces.

The adsorption of particles on fluid interface is particularly strong if the contact angle θ_c is in vicinity of 90° [10]. The process of adsorption of a solid particle with $\theta_c = 90°$ onto a fluid interface is qualitatively illustrated in Figure 1.1.

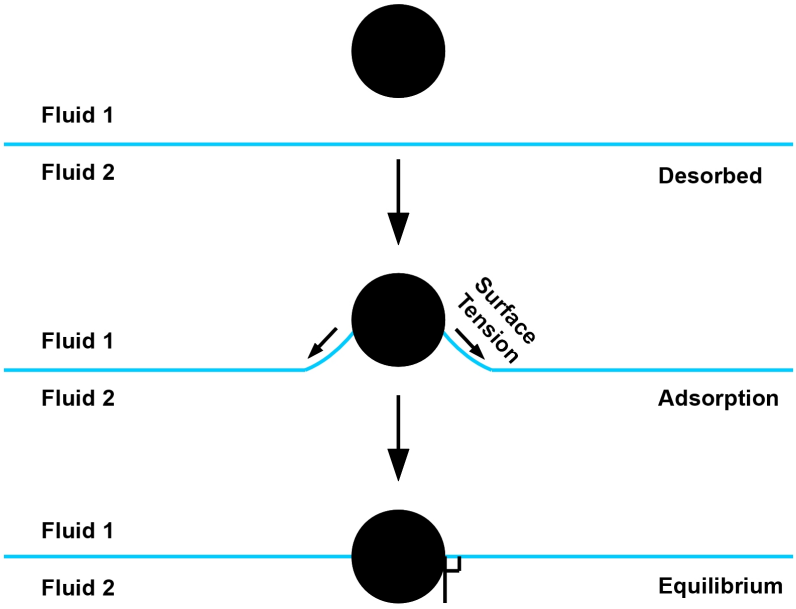

Figure 1.1: The process of adsorption of a solid particle onto fluid interface.

Prior to adsorption, the solid particle is unaffected by capillary forces and the fluid interface is flat (Figure 1.1 top). Once the particle comes into contact with the fluid interface, the fluid interface bends towards the particle (Figure 1.1 middle). The normal component of the surface tension force pulls the particle towards the fluid interface until it reaches an equilibrium position that is dictated by its wettability (Figure 1.1 bottom).

When the absorbed particles on the interface are dense, the modification of fluid interface by colloidal particles can have macroscopic, leading-order effects. For example, due to large adsorption energy, colloidal particles can be used as an alternative of molecular surfactants, to improve the stability of foams and emulsions [6, 8, 11]. The function of stabiliser is to prevent drops or bubbles from coalescencing or breaking up, therefore freezing the fluid interface area within the

fluid. An emulsion stabilised by solid particles is called a Pickering emulsion. It was found in 1907 but only started to draw significant interest in recent decades [1, 12–15]. Figure 1.2 illustrates the comparison between a classical emulsion and a Pickering emulsion.

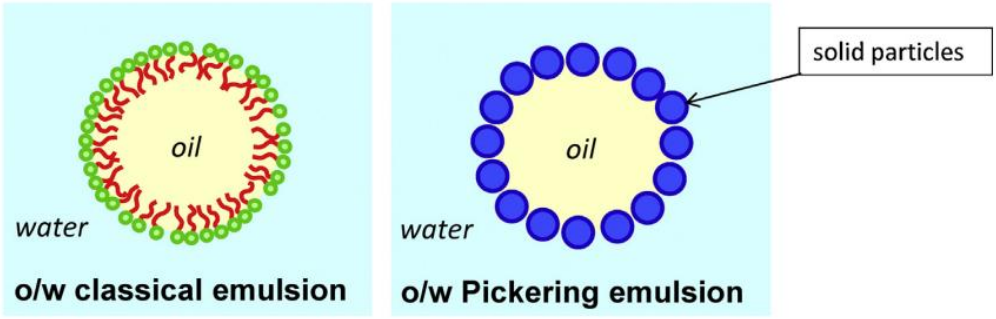

Figure 1.2: Classical (surfactant stabilised) and Pickering (particle stabilised) emulsion stabilised by different additives as emulsifier. The picture is taken from [1].

Besides being employed as emulsifiers, colloidal particles can be used to fabricate capsules with desired permeability and mechanical properties [2]. The fabrication involves assembling solid particles on the surface of liquid drops and draining the liquid inside afterwards. The resulting capsules, called "colloidosomes" as shown in Figure 1.3, can be used for encapsulating active ingredients in drug delivery or other biomedical applications. Exploiting fluid interfaces as templates for particles self-assembly is also used regularly in microfluidic applications [16–18]. In mineral industry, fluid interfaces are often used as agents to separate different ore particles based on their different hydrophobicity [19]. Colloidal particles also display interesting analogies with globular proteins [20], which makes the study of particle stabilised interfaces relevant to the production of food and personal care products.

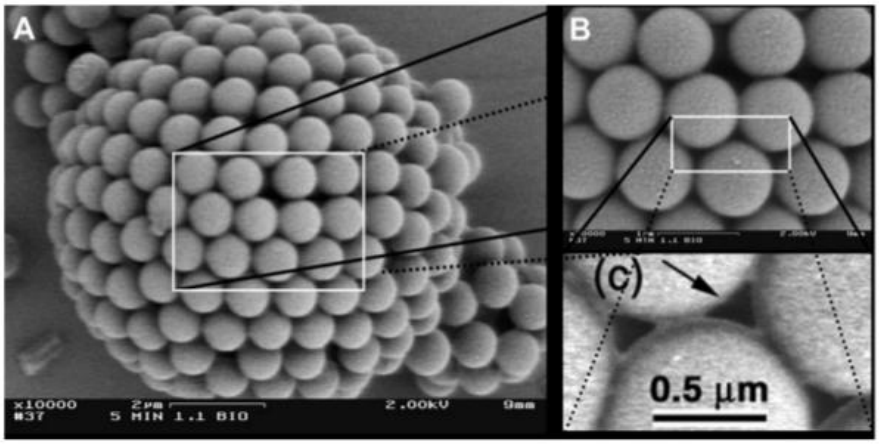

Figure 1.3: Scanning electron microscope image of a dried colloidosome with close-ups. The picture is taken from [2].

Based on the same principle of creating Pickering emulsion, colloidal particles can be used to create novel soft materials by stopping the phase separation process of a binary immiscible fluid or preventing drops from coalescence [21, 22]. The most important application of this mechanism is the development of Bijels which stands for bicontinuous interfacially jammed emulsion gels [3, 23, 24]. Bijels have a stable interconnected bicontinous interface structure (Figure 1.4) because the colloidal particles have jammed the fluid interface preventing further phase separation process.

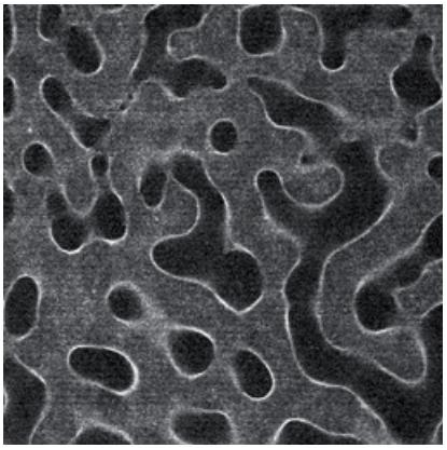

Figure 1.4: A bicontinous interfacially jammed emulsion gels. The picture is taken from [3].

1.1 Physics of Particle-Laden Fluid Interface

To illustrate the equilibrium position of a particle embedded in a fluid interface, let us consider a horizontal air-water interface (Figure 1.5). When the size of the particle is relatively large, for example in millimeter range, the weight of the particle is important and the fluid interface around the particle is strongly deformed because the particle "pushes" the interface in the direction of gravity (Figure 1.5a).

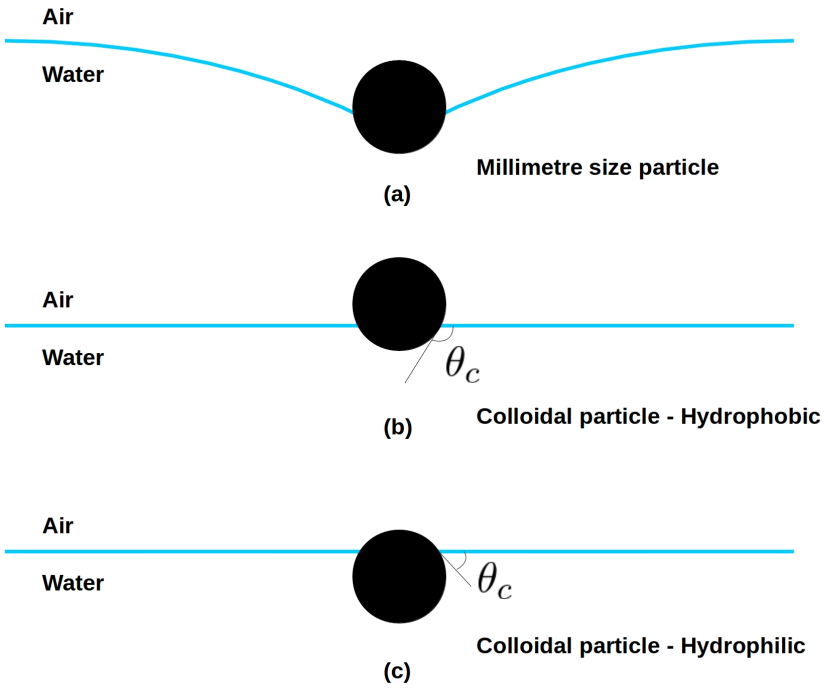

Figure 1.5: Different configurations for a spherical particle absorbed to an air-water interface: (a) millimetre size particles tend to deform a fluid interface significantly due their weight, (b) hydrophobic colloidal particles will reside more in air, (c) hydrophilic colloidal particles will reside more in water.

The importance of gravity over surface tension effects is quantified by the Bond number $Bo = \Delta\rho g a^2/\gamma$, where a is the particle radius, g is gravity acceleration, γ is surface tension of fluid interface and $\Delta\rho$ is the density difference between the solid particles and the heavier fluid (water in this case). Colloidal particles typically have $Bo \ll 1$, therefore the effects of gravity are negligible. The particle is embedded in a flat interface and its position depends on the contact angle θ_c which measures the wettability of the particle [25]. Hydrophobic particles ($\theta_c > 90°$) will reside mostly in the air phase (Figure 1.5b). Hydrophilic particles ($\theta_c < 90°$) will tend to reside more in the water phase (Figure 1.5c).

To understand the reason for choosing colloidal particles as an alternative emul-

sion stabiliser other than molecular surfactants, we need to quantify the robustness of the adsorption of a colloidal particle at a fluid interface. A measure of the ability of a solid particle to adhere to a fluid interface is the single-particle adsorption energy which is the work necessary to remove a particle from a fluid interface in absence of other particles. For a chemically homogeneous spherical particle trapped at a flat fluid interface, the adsorption energy can be calculated as [8]

$$\Delta E = \pi a^2 \gamma (1 \pm \cos\theta_c)^2, \tag{1.1}$$

where a is the particle radius, γ is the surface tension of fluid-fluid interface, θ_c is the contact angle. The sign in the bracket depends on which fluid the particle is about to be inserted into. The single-particle adsorption energy given by (Equation 1.1) is often compared to the thermal energy kT, where k is the Boltzmann constant and T is the absolute temperature, to determine whether a particle will reside firmly in the fluid interface or will desorb on a regular basis. The thermal energy $kT = 4.11 \times 10^{-21} J$ is the energy scale associated with the thermal fluctuation experienced by microscopic entities [26]. Thermal fluctuation will cause small particles to move around in a random manner.

For typical water-oil fluid interface with surface tension around $50mN/m$, the adsorption energy of a micron-size colloidal particle according to Equation (1.1) is of the order of $10^7 kT$. Hence this energy is several order of magnitude higher than the thermal energy, and the adsorption of colloidal particles is essentially irreversible under normal conditions. This constitutes a major difference between molecular surfactants and colloidal particles regarding the interaction with the fluid interface [27]. Molecular surfactants, due to their much smaller sizes, are strongly affected by Brownian motions and prone to desorption over time.

Besides the robustness of adsorption, there are several other advantages of using colloidal particles over molecular surfactants. Colloidal particles can be used at high temperatures [12] and can remain free from chemical hazard since the adsorption relies only on mechanical effects [28]. The properties of the particles can also be modified to respond to a specific external field [15, 29].

Another important distinctive feature of solid particles in comparison to molecular surfactants is the capability to jam the fluid interface, creating shell like fluid interface [30, 31]. This feature is a unique characteristic of rigid objects. With sufficiently high concentrations of colloidal particles, the colloid-laden fluid interfaces can exhibit viscoelastic behaviour [32]. For particles experiencing attractive interactions, the formation of percolating networks of particles can transmit stress through its "backbone" determining the elastic response. The dynamic formation and disruption of the percolating network can determine an effective viscosity [33]. Particles jammed at fluid interface confer the interface with solidlike properties, and can produce irreversible plastic deformation. This feature can result in the existence of stable nonspherical drops or bubbles [34].

1.1.1 Outstanding Problems in the Field

Although the physical mechanism underlying the adsorption of a single solid particle onto a fluid interface is established , the collective behaviour of a whole particle monolayer covering a fluid interface still presents interesting questions [35–37]. A liquid drop fully covered with particles can exhibit different rheological properties under different force loading conditions [30, 38], incorporating viscous effects of fluid and elasticity and plasticity of solid [34]. The presence of dynamic interface deformations, induced by flow or external fields, makes the situation even more

complicated [39]. It is still not clear how surface stresses due to particles are distributed on the fluid interface, especially when the fluid interface has a complex geometry or the effects of shear elasticity become prominent [40].

Understanding the mechanisms by which the particles modify the interfacial properties and developing coarse-grained constitutive models representing the mechanical response of particle-laden fluid interface remain crucial challenges [41]. A full characterisation of particle-laden fluid interface will require not only the knowledge of the particle adsorption, but also the details of the particle-particle interactions along the fluid interface [42].

On the other hand, the arrangement of particles on fluid interfaces is highly dependent on the types of particle-particle interactions. On a 2D surface, particles with attractive interactions will create a monolayer with gel-like structures, exhibiting the process of phase separation and creating large surface area void of particles [43]. When a monolayer is highly compressed or only isotropic repulsions exist between particles, the dominant structure is the hexagonal packing [44]. The packing structures of a monolayer become more complicated on curved surfaces, creating defects and dislocations [45–47]. The implications of particle packing patterns on rheological properties of a monolayer need to be addressed. For 3D bulk suspensions, the mathematical framework bridging particle-level quantities and suspension rheological properties is now quite established [48–51]. In contrast, work on interfacial suspensions where the method of area averaging is adopted is scarce, and limited to theoretical investigations to derive balance equations [52–54].

Regarding the robustness of the adsorption of particle monolayer on fluid interface, a typical argument is that the adsorption is irreversible because $\Delta E \gg kT$ [8]. However, this argument only takes into account the perturbations due to ther-

mal fluctuations, and particles can still be pushed out of the fluid interface under mechanical loading [4, 55, 56]. Such effect of forced particle desorption can in principle occur whenever the particle-covered interface is locally compressed. Local compression can be due to geometric or hydrodynamic effects, for example a change in volume or shape of the region enclosed within the fluid interface [56, 57], or the presence of converging streamlines as in the rear stagnation point of a translating particle-covered bubble or drop [58]. Desorption due to mechanical loading is a rupture process: if the normal force acting on a particle is larger than the critical capillary force holding the particle to the fluid interface, the particle will desorb [55].

An alternative outcome of the compression of a particle-covered interface is the occurrence of monolayer buckling without desorption [44, 59–61]. In this scenario the particle-covered fluid interface behaves as a continuous elastic shell, and buckles when the surface pressure exceeds a threshold value. While the buckling mechanics of the planar or curved particle-covered interfaces have been explored previously [62–65], the physical conditions differentiating the scenarios of desorption of the particles versus buckling of the fluid interface still remain an open question.

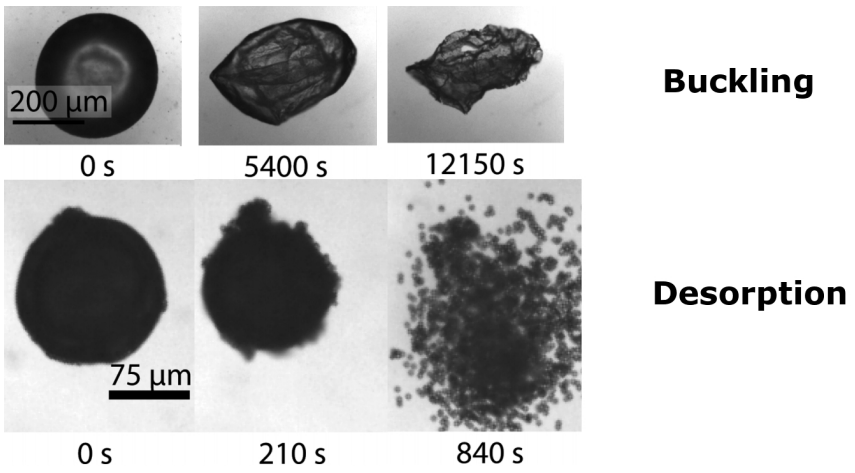

Figure 1.6: Dissolving air bubbles covered with microparticles of different sizes. Top: buckling for $a/R = 0.0012$. Bottom: desorption for $a/R = 0.03$ (From Ref. [4]). The parameter a/R is the ratio between the radius of each particle and the radius of the bubble.

Predicting whether desorption or buckling will occur is an outstanding challenge, as the two scenarios occur under quite similar experimental conditions [4]. Figure 1.6, from Ref.[4], shows an experiment in which a bubble covered by a nominally monodispersed monolayer of hydrophilic polystyrene micro-particles is slowly compressed. The surface compression is obtained by increasing the solubility of the gas in the liquid, with a consequent outward flux of gas and a reduction in the volume of the bubble. In the case illustrated in the top panel of Figure 1.6, the compression of the monolayer produced by the shrinkage of the bubble gives rise to a change in shape of the particle-covered interface with no particle desorption. This scenario is called pure buckling. In the case illustrated in the bottom panel of Figure 1.6, the particles instead are seen to desorb from the surface of the bubble, eventually accumulating at the the bottom of the container ($t = 840s$). The size ratio a/R between the particle and the bubble radii is 0.0012 in the top panel and 0.03 in the bottom panel. This suggest that the transition from buckling to desorption could depend on the relative size of the particle and the bubble. Very

little theoretical guidance is available on the effect of interface curvature on the buckling-to-desorption transition.

Experiments related to the topic are not many, and it is difficult to make definite conclusions regarding the main mechanisms at play because of experimental difficulties. Bordács et al. [66] studied experimentally the compression of flat particle-covered air-water and oil-water interfaces in a Langmuir trough, observing both desorption and buckling. Their work identified the particle wettability as a key variable controlling the transition from buckling to desorption. This conclusion is also supported by more recent experiments [60]. Regarding curved interfaces, particle desorption effects were studied in the context of a deflated drop experiment in Ref. [9]. In that experiment, only desorption was observed, while buckling was observed under quite similar conditions by other investigators [67, 68]: in addition to particle wetting characteristics, the cohesiveness of the particulate layer could be an important factor in these observations [66]. In the analysis of experiments in which bubble shape oscillations were induced by ultrasound waves [69], it was hypothesised that particle desorption could correlate with regions of high surface curvature , but the specific mechanisms of desorption were not established.

1.2 Simulating Particle-Laden Fluid Interface

A liquid system featuring a particle-laden fluid interface is a complex multicomponent system, whose numerical simulation is particularly challenging. In the follows, two groups of established numerical methods are reviewed first: the first group is for simulating interfacial flows (without particles) and the other is for simulating particles in single-phase fluids (without fluid interfaces). Then a few approaches that have been used so far to simulate interfacial flows with solid particles are de-

scribed and the problems regarding the existing simulation methods are discussed.

1.2.1 Numerical Methods for Interfacial Flows

All the numerical methods developed for interfacial flows couple a momentum equation and a continuity equation for the fluids to an equation or a set of equations governing the shape of the fluid interface [70]. The different numerical methods differ mostly in the way the fluid interface is described and the interfacial boundary conditions are applied.

One of the oldest examples of simulation methods for interfacial flows is the marker-and-cell (MAC) method [71, 72]. This method uses a crude approximation of the free surface: marker particles are initially assigned to each computational cell containing fluid and these particles are advected by the local fluid velocity. In the original implementation of the method, the free surface pressures were set only at the centres of the cells containing a portion of a fluid interface, and no boundary conditions were applied at the actual location of the fluid interface inside the cells.

An improvement of the MAC method is the volume of fluid (VOF) method, where a continuous field called the marker function is used instead to label the phase composition of each cell [73]. The VOF method can naturally preserve the mass very well and there is no need of provision for handling the change of interface topology [74]. The exact interface location has to be reconstructed from the marker function value assigned to each cell. There are lots of effort made to improve the reconstruction technique [75–77].

Both VOF and MAC methods are classified as volume-tracking methods. The front-tracking method, on the other hand, is a surface-tracking method. It in-

troduces a group of unstructured boundary fitted markers to explicitly track the location of the fluid interface [78, 79]. The markers move through the a fixed Eulerian grid where the flow field is solved. The front-tracking method offers a better resolution of the interface than the volume-tracking methods, because the surface markers track exactly the location of the fluid interface. Improved accuracy can be achieved in front-tracking method by implementing high-order interpolation schemes to represent the fluid interface [80]. The higher accuracy of front-tracking method comes at the cost of constant surface grid remeshing.

All the methods listed above for resolving fluid interfaces are classified as interface-tracking methods. There is also another class of methods called interface-capturing methods in which the location of fluid interface is implicitly calculated. One of them is the level set method [81, 82]. In this method the fluid interface is implicitly represented by the zero level set of a continuous field, which is governed by a PDE. However this method suffers significantly from loss of mass and additional measures are needed to tackle this problem [83].

Being similar to the level set method, the phase field method is another interface capturing method that can implicitly handle the change of interface morphology [84–87]. It is a diffuse interface method, where a phase field variable that captures the location of the interface varies smoothly across an interface region. The width of the diffuse interface bears no physical meaning and can be larger than the physical thickness of the fluid interface.

With the emergence of lattice Boltzmann method (LBM) for fluid flow, methods for modelling fluid interfaces in LBM started to appear [88]. In LBM, instead of the continuum momentum equation, a discretised Boltzmann equation governing the transport of statistical populations of fluid molecules is solved. A most

noticeable approach for simulating multiphase flows is the Shan-Chen model [89]. The Shan-Chen model incorporates the microscopic interactions that exist between fluid molecules of different fluids to represent the surface tension at macroscopic level. Another method available for LBM [90] makes use of a free energy formulation in a similar way to the phase field method.

1.2.2 Numerical Methods for Particulate Flows

Numerical methods for solving fluid flows with suspended particles can be roughly classified into two categories: particle-resolved methods, in which the flow boundary layers around each particle are fully resolved; and point-particle methods, in which the presence of the particle is replaced by a source term in the fluid momentum equation.

The arbitrary Lagrangian-Eulerian method [91] is one of the approaches for resolving flows around suspended particles. In this method, fluid region is meshed with an unstructured, time-dependent grid that conforms to the surface of each particle. This method is difficult to implement, as it requires constantly adapting the mesh to the changing positions of the particles during the simulations.

The immersed boundary (IB) method is another popular particle-resolved method for the direct simulations of solid particles suspended in fluid flows [92–94]. The advantage of this method is that the governing equations are solved on a nonbody conformal Cartesian grid, greatly simplifying the mesh generation procedures. The surface of a particle is tracked by a group of Lagrangian points in space and the boundary conditions at the particle surface are imposed indirectly by introducing additional forcing terms in the fluid momentum equation. The original IB method by [95] was developed for flows with immersed elastic boundaries. For solid parti-

cles in flows, one popular approach is to make the forcing term to provide feedback control of the flow velocity near the surfaces [96, 97].

Another particle-resolved method is the Lagrange-multiplier based fictitious domain method [98–100]. The key feature of this method is that the explicit calculation of hydrodynamic forces and torques on particles is not required. The rigid-body motion of a particle is enforced by using a distributed Lagrange multiplier.

The above mentioned fully-resolved methods enable the resolution of the flow around each particle. But they are generally complicated to implement or computationally expensive, therefore usually limited to the simulations with a small number of particles. When particle-scale features are not of primary interest, the point-particle method can be a valid alternative.

The point-particle approach is widely used in simulations of turbulent particle-laden flow [101–104]. The fluid momentum equation is solved on fixed Eulerian grid while each particles is treated as a Lagrangian point moving according to a Newton's equation of motion. The Lagrangian-based particle tracking solver is usually coupled with a DNS or LES flow solver. The simplicity of the method allows the simulations of particle-laden flows with one million particles [105]. However, only some of the simulations include the feedback from the particles to the fluid flow [106, 107], most of the applications of the point-particle method are limited to dilute particulate flows where only one-way or two-way coupling is applied [108]. In one-way coupling, only the transport of the particles by the fluid is considered, but the feedback of the particles on the flow is neglected. In two-way coupling approaches, the effect of particles on the fluid flow is included by incorporating forcing terms in the fluid momentum equation but the particle-particle collisions

are neglected. To simulate fluid flow with dense suspension, it is necessary to implement four-way coupling in which particle-particle interactions are included.

In the low Reynolds number regime, several special methods are available based on the green function of Stokes equation such as Stokesian dynamics [109] and the multipole expansion method [110]. The availability of green function enables direct prescription of fluid velocity far away from the particles [111, 112]. However with the presence of the fluid interfaces, the green function of the Stokes equation will depend on the the configuration of the surrounding fluid interfaces hence these green function based methods can not be easily extended to simulate particle-laden interfacial flows.

1.2.3 Numerical Methods for Particle-Laden Fluid Interface

When both solid particles and fluid-fluid interfaces are present, few schemes are available for numerical simulations [113–116]. The difficulties mostly come from accurately tracking moving contact line formed by the fluid interface on the particle surface [117]. The first direct numerical simulation of fluid flows in which particles are embedded in a fluid interface are presented by Singh and Joseph [118]. Their work combines the level set method for interface capturing with the method of fictitious domain for treating the rigid body motions of the solid particles, and the moving contact line is modelled using numerical slip. They were able to simulate the sinking of the solid particles to equilibrium depth in a fluid interface and the evolution to clusters by two or four particles under capillary attraction.

Pozrikidis and collaborators [119] have developed a boundary integral method

that can handle arbitrary particle shapes having rotational symmetry about an axis that is normal to the fluid interface. A regularisation is required by means of slip boundary condition to avoid non-integrable singularity of the traction at the contact line.

For simulations in the regimes of low Reynolds number and low capillary number, Danov and Dimova [120] formulated the problem of a particle straddling in a spherical surface in toroidal coordinate system. The problem was then reduced into a two-variable space and numerically solved by an Alternating-Direction-Implicit method.

For simulations of a large number of particles in a two-phase fluid environment, Stratford et al. [23] have used a lattice Boltzmann method incorporating a free energy formulation for solving the flow field; the inclusion of solid particles is accounted by using the scheme of bounce-back on links originally proposed in [121]. Jansen and Harting [122] have used an LBM Shan-Chen model for resolving fluid interface and a molecular dynamics solver for the dynamics of suspended particles.

Millet et al. [123] have used a diffuse interface approach to handle both fluid-fluid and particle-fluid interface. Their method can be used to simulate spinodal decomposition with moderate number of particles at fluid interface. However, no fluid momentum equation is included in this method and simulations are restricted to quasi-static conditions.

1.2.4 Outstanding Problems in Simulation of Particle-Laden Fluid Interface

Simulation of particle-laden fluid interface is always a challenging task, as the fluid interface can possibly be covered with hundreds of thousands of particles. There is a huge separation between the characteristic length scales of particles arrangement and fluid interfaces [124]. Most of the current numerical packages mentioned previously devote a large amount of resources to solve the particle scale phenomena and enable physical insights into understanding particle adsorption and desorption [125].

On the other hand, there is a demanding need to study collective properties of particle-laden fluid interfaces, for example particle ordering and dynamics in the interface [126, 127], the effect of particle shape on self-assembly [128–130], and the modification of the interfacial morphology by the particles [131, 132]. The current numerical schemes capable of simulating collective dynamics of particle-laden fluid interface are not well feasible for commonly available computing infrastructures, for example the main production runs in Ref.[23] took around 1 week on a 32-processor IBM p690+ system as reported.

It is usually estimated that at least 10 grid nodes are required to properly resolve the hydrodynamic flows around a single particle [133, 134]. Fully resolved simulations of suspension of particles within single phase flow are already expensive. Due to the spatial resolution needed for resolving the liquid meniscus on particle surfaces, the simulations of fluid interfaces interacting with solid particles are even more difficult to realise. During particle desorption narrow fluid necks are formed [135], and it would require grid cells drastically smaller than the particle radius to capture these thin liquid threads. Moreover, the physics associated with moving

contact line involves molecular scale physics, which can not be entirely captured by a continuum mechanics formulation unless models for the motion of contact lines are used. Taking into account these extremely demanding requirements for resolving the particle scale features, It is natural to suspect if the current "fully resolved" methods for large scale particle-laden fluid interfaces can truly resolve everything.

1.3 Aims and Objectives

From the previous review of the simulation approaches to study the problems of liquid-liquid and liquid-gas flows, particle-laden flows and particle-laden interfacial flows, it is clear that achieving fully resolved accuracy in simulations involving both fluid interfaces and a large number of particles is currently enormously expensive from a computational standpoint. This Ph.D project is motivated by the demand for a new simulation framework that can be used to study problems involving particle-laden fluid interfaces having a level of complexity comparable to that of physical experiments, while remaining simple enough to implement and being computationally efficient.

The first aim of this Ph.D project is to develop a new mathematical formulation describing the physics of fluid interfaces, the capillary interactions between particle and fluid interfaces and the dynamics of particles and fluid flows. The corresponding numerical implementation of the new formulation should yield a simulation program that is capable of simulating fluid interfaces covered by a large number of particles.

The second aim is to use the developed simulation code to investigate physi-

cal problems involving liquid drops. The investigation will focus on the effect of surface stress created by particle monolayers on fluid interfaces, in other words the mechanical properties of the "composite" interface. The result should reveal the connection between the particle arrangement on the fluid interfaces and the characteristic behaviours of the particle-laden fluid interfaces.

To achieve the above mentioned two overarching aims, the following objectives are sought:

- Develop a series of assumptions and approximations to model the particle-scale physics that is expensive to resolve but less significant to the overall dynamics of the particles and of the fluid interface.
- Adopt an interface capturing method to describe the time-dependent shape of the fluid interfaces.
- Couple the equation governing the shape of the fluid interface with the fluid momentum equation.
- Develop a model for the particle-interface capillary interactions and implement a particle-tracking solver coupled to the solver for fluid flow and fluid interfaces. At this stage the dynamics of fluid flow, fluid interface and particles should all be coupled.
- Conduct validation studies with the newly developed simulation program.
- Investigate the effect of absorbed particles on the surface tension of the fluid interface and possibly the presence of anisotropic surface stress.
- Investigate the behaviours of a particle-covered drop under compression and the role played by surface pressure created by the particle monolayer.

1.4 Accomplishments

At the end of the Ph.D project, the author have reached the following achievements:

- Starting from ground zero, after numerous revisions, the author has developed a fully working numerical program for simulations of particle-laden fluid interface. The program is written in C++ and is named Fast Interface Particle Interaction, or FIPI in short.

- The FIPI code is capable of producing simulation results on the length scale of the characteristic size of the fluid interface morphology, while the performance of the code allows most simulations to be done in days on a normal desktop computer.

- The simulations carried out in this project have revealed two interesting physics of particle-covered drop which are not possible to simulate before. First, particles with repulsive interactions, whether due to elastic contacts or electrostatics, can not only reduce surface tension of fluid interface but also confer fluid interface with shear elasticity, enabling fluid interface to sustain anisotropic surface stress. Second, under the effect of particles on the surface, the particle-covered drop can sustain negative Laplace pressure by undergoing buckling. The drop can maintain non-spherical shape at steady state. Simulations done with FIPI have not only captured the change of morphology of the fluid interface, but also given information on particle-level features which is challenging to observe in experiments.

- A side project in collaboration with GlaxoSmithKline has been completed by the author. The particle tracking model of FIPI has been used to investigate the fracture fluidisation of cohesive powders inside dry powder inhaler (DPI)

device. The investigation has identified an important factors that have been overlooked in the previous work: the cohesion between powder particles and the channel walls. The simulations done with FIPI particle tracking model hint that the maximum and the distribution of chunk sizes are correlated with the tensile strength and the packing ratio of the powder bed.

- The investigations of particle-covered drops with FIPI have yielded two peer-reviewed publications:
  - Gu, Chuan, and Lorenzo Botto. "Direct calculation of anisotropic surface stresses during deformation of a particle-covered drop." Soft matter 12(2016): 705-716.
  - Gu, Chuan, and Lorenzo Botto. "Buckling vs. particle desorption in a particle-covered drop subject to compressive surface stresses: a simulation study." Soft Matter 14(2018): 711-724.
- The author has also given three presentations at conferences and workshops:
  - "Particle-laden interfaces: direct calculation of interfacial stress from a discrete particle simulation of a pendant drop", 68th Annual Meeting of the APS Division of Fluid Dynamics.
  - "Flow and fracture of a cohesive powder layer: porous media flow analysis of flow-induced stresses inside the solid", 11th European Fluid Mechanics Conference.
  - "Fast Simulation of Particle-laden Interfaces with the FIPI method", Workshop of Structured Soft Interfaces: Caught Between Multi-Scale Simulation and Application, Lorentz Center 2017.

1.5 Structure of the Thesis

The thesis is organised as follows. In chapter 2, the mathematical formulation of FIPI and its numerical implementation will be described complemented with several validation studies. In chapter 3 and 4, the potential of the method for simulating two interfacial problems of interest to experiments will be illustrated. In chapter 3, the results of the simulation of a pendant drop covered with a particle monolayer is given, showing the capability of FIPI to calculate anisotropic surface stresses during the deformation of the pendant drop. In chapter 4, the mechanism underlying buckling and desorption of a particle covered spherical drop is studied by numerical simulations. The report of a side project in collaboration with GlaxoSmithKline regarding fluidisation of cohesive powders will be given in chapter 5 and the conclusion of the thesis is drawn in chapter 6.

Chapter 2

Fast Interface Particle Interaction Method

The motivation of creating the FIPI method is to simulate fluid interfacial structures with presence of colloidal particles. The colloidal particles in the simulations can become absorbed onto fluid interfaces or desorbed into bulk fluid. The simulations carried out by this method should accurately resolve interfacial structures and hydrodynamics on length scales much larger than colloidal particles. On the other hand, the particle-scale physics are modelled to reduce the computational cost.

The current chapter starts by describing the mathematical formulation of the method, followed by a detailed explanation of how FIPI can capture the modulation of surface tension by colloidal particles. The numerical implementation and several validation studies are provided at the end.

2.1 Mathematical Formulation of the FIPI method

The formulation of FIPI is divided into three modules as shown in Figure 2.1: FIPI-Interface, FIPI-Fluid and FIPI-Track, related to describing the fluid interface capturing, the hydrodynamics of the fluid, and the dynamics of the particles, respectively.

Since the objectives of the project involve only investigations of colloidal particles, the current scope of the FIPI method is limited to problems in Stokes flow regime, hence the inertia of both fluid and particles is neglected. However the method can be easily expanded to simulate fluid flows with finite Reynolds number in the future.

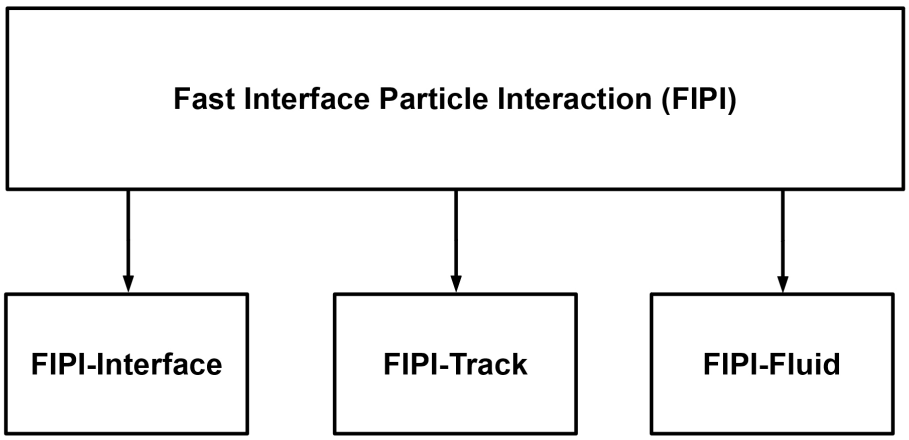

Figure 2.1: Three components of the FIPI method.

2.1.1 FIPI-Interface

To resolve fluid interface created by two immiscible fluids, the phase field method is adopted in FIPI-Interface to capture the structure and movement of fluid interfaces [136]. The phase field method is a diffuse interface method where a phase field variable ϕ is used to identify the fraction of each phase. The dynamics of ϕ is governed by the Cahn-Hilliard equation

$$\frac{\partial \phi}{\partial t} + \mathbf{u} \cdot \nabla \phi = \nabla \cdot M \nabla \xi, \tag{2.1}$$

where $\mathbf{u}$ is the fluid velocity, M is a mobility parameter and ξ is a chemical potential defined as a functional derivative of a total free energy density F with respect to ϕ

$$\xi = \frac{\partial F}{\partial \phi}. \tag{2.2}$$

Adopting the formulation in Ref.[137], F is expressed as

$$F(\phi, \nabla \phi) = \frac{\lambda}{4\epsilon^2} \left(\phi^2 - 1\right)^2 + \frac{1}{2} \lambda \left|\nabla \phi\right|^2, \tag{2.3}$$

where λ and ϵ are two parameters together defines the value of surface tension while the thickness of the fluid interface is independently defined by ϵ. On the right hand side of Equation (2.3), we can see the total free energy density is the summation of two terms: the first term is associated with the bulk fluid and the second term is associated with the fluid mixing.

To find the analytical solution of ϕ in Equation (2.1), we consider a static planar fluid interface in an unbounded environment. An equilibrium is reached

when $\xi = 0$. The one-dimensional solution of Equation (2.1) satisfies

$$\frac{1}{\epsilon^2}(\phi^3 - \phi) = \frac{\partial^2 \phi}{\partial x^2}, \tag{2.4}$$

which yields

$$\phi = \tanh(\frac{x}{\sqrt{2}\epsilon}). \tag{2.5}$$

At steady state, the Cahn-Hilliard equation produces a fluid interface region with a finite thickness across which ϕ changes smoothly from -1.0 to 1.0. The regions marked by $\phi = 1$ and $\phi = -1$ represent the pure bulk phase of each fluid and the exact location of fluid interface is defined as an isosurface where $\phi = 0$.

The surface tension of a planar fluid interface is equal to the integral of the free energy density across the whole fluid interface from one phase to the other [86]:

$$\gamma = \int_{-\infty}^{+\infty} F(\phi, \nabla\phi) dx. \tag{2.6}$$

Using the analytical solution given by Equation (2.5), it can be easily seen that the bulk and the gradient energy terms in Equation (2.3) are identical. Calculating the integration yields

$$\gamma = \lambda \int_{-\infty}^{+\infty} (\frac{\partial \phi}{\partial x})^2 dx = \frac{2\sqrt{2}}{3}\frac{\lambda}{\epsilon}. \tag{2.7}$$

Hence the surface tension of the bare fluid interface is controlled by two parameters λ and ϵ.

2.1.2 FIPI-Track

The FIPI-Track module contains all the formulations related to the dynamics of each particle. Neglecting the rotation of the particle and inertia, the Newton's equation of motion of equation for each particle is

$$\mathbf{0} = m_p \mathbf{g} + \mathbf{F}_{pp} + \mathbf{F}, \tag{2.8}$$

where m_p is the mass of the particle, $\mathbf{F}_{pp}$ represents the force exerted by surrounding particles, e.g., electrostatic force or solid contact force, $\mathbf{F}$ is the force exerted from surrounding fluid on the particle. We have [118]

$$\mathbf{F} = \oint_{CL} \gamma \mathbf{n}_c ds + \oint (-p\mathbf{I} + \boldsymbol{\sigma})\, dA, \tag{2.9}$$

where $\mathbf{n}_c$ is the normal vector lying in the fluid interface and normal to the contact line. On the right hand side of Equation (2.9), the first integral is the total force due to surface tension acting along the contact line if the particle is absorbed onto the fluid interface, the second integral is the total force due to stress generated by motion relative to the surrounding fluid.

Calculation of the integrals in Equation (2.9) is not a trivial task: calculating the force due to surface tension requires the knowledge of the location of the contact line on the particle surface and the corresponding contact angle [118, 138]; calculating the second integral requires the boundary layer around the particle to be resolved. In FIPI, each particle is assumed to be a Lagrangian point and both forces on the right hand side of Equation (2.9) are modelled:

$$\mathbf{F} \approx \mathbf{F}_{pi} + \mathbf{F}_h, \tag{2.10}$$

where $\mathbf{F}_{pi}$ represents the total capillary interaction force exerted on the particle from fluid interface, and $\mathbf{F}_h$ represents the total hydrodynamic drag force. As suggested by [139, 140], for small particle Bond number, the capillary force can be adequately described as a linear function of the displacement of the particle from the interface, and the following linear model is adopted:

$$\mathbf{F}_{pi} = \begin{cases} -f\pi\gamma\mathbf{d}, & \text{if } |\mathbf{d}| < a \\ \mathbf{0}, & \text{if } |\mathbf{d}| > a \end{cases}. \tag{2.11}$$

where f is a non-dimensional parameter independent of the particle size and $\mathbf{d}$ is the minimum distance vector pointing from the centre of particle (j) to the fluid interface. For $|\mathbf{d}| > a$ the particle is assumed to be desorbed from the fluid interface.

The adsorption energy corresponding to Equation (2.11) is $E = \frac{1}{2}f\pi\gamma a^2$. Hence, f represents the ratio of the adsorption energy E to the capillary energy scale γa^2. Comparing $\Delta E = \frac{1}{2}f\pi\gamma a^2$ with the single-particle adsorption energy $\Delta E = \pi\gamma a^2(1 - |\cos\theta_c|)^2$ [8] gives $f = 2(1 - |\cos\theta_c|)^2$. As θ_c varies from $\theta_c = 0°$ (particle residing in the outer liquid) to $\theta_c = 180°$ (particle residing in the inner liquid), f varies from 0 to 2.0 as shown in Figure 2.2. A further dependence on the contact angle can be embedded into the model (2.11), by taking into account that the equilibrium position of the particle in a flat interface is a known function of the contact angle.

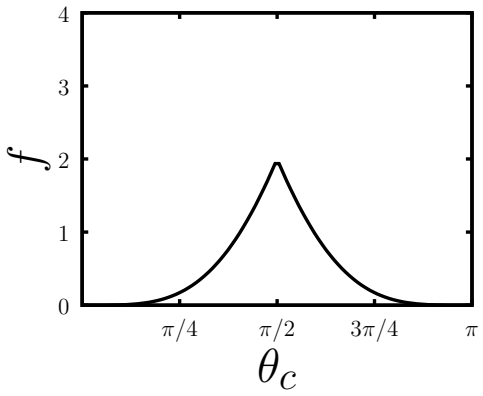

Figure 2.2: Expected dependence, based on the single-particle adsorption energy, of the non-dimensional adhesion strength parameter f on the particle contact angle.

For the hydrodynamic force $\mathbf{F}_h$ in Equation (2.10), the Stokes drag law is adopted:

$$\mathbf{F}_h = -6\pi\mu a \left(\dot{\mathbf{x}}_p - \mathbf{u}_f\left(\mathbf{x}_p\right)\right), \tag{2.12}$$

where $\mathbf{x}_p$ is the displacement of the particle and $\mathbf{u}_f(\mathbf{x}_p)$ is the undisturbed fluid velocity at the location of the particle. Improvements to this model can of course be considered. For example, one can implement a concentration-dependent drag coefficient in Equation (2.12) or introduce lubrication forces when a particle is close to another particle or fluid interfaces.

The last force $\mathbf{F}_{pp}$ in Equation (2.8) is the summation of the forces exerted from all neighbouring particles within a range onto the current particle. For electrostatic repulsion forces between particle i and j in chapter 3, the following inverse-square law is adopted:

$$\mathbf{F}_{pp}^{(ij)} = \begin{cases} \left(\frac{F_0}{r^2}\right)\mathbf{n}_{ij}, & \text{if } a < r \leq r_c \\ \mathbf{0}, & \text{if } r > r_c \end{cases}, \tag{2.13}$$

where F_0 is a parameter determining the strength of the interactions, r is the centre-to-centre distance between two particles and r_c is a cut-off distance.

For all other chapters, the interactions between particles are assumed to be of solid contacts. A linear spring model is adopted following the practice of the discrete element method (DEM) [141, 142]:

$$\mathbf{F}_{pp}^{(ij)} = \begin{cases} -k_c(r - r_c)\mathbf{n}_{ij}, & \text{if } r < r_c \\ \mathbf{0}, & \text{if } r > r_c \end{cases}, \tag{2.14}$$

where k_c is a stiffness parameter. When $k_c \to +\infty$ and $r_c \to 2a$, the perfect hard sphere solid contact model is restored.

For simulations of dense particle monolayers, the value of r_c needs to be large enough to reduce the constraint on time stepping, but also small enough to minimise the interactions of a particle with its second nearest neighbours. The choice of the value of r_c needs to be adjusted according to the surface area fraction ϕ_s of particle monolayer. If we assume that the packing of particles is quasi-hexagonal on a surface, the average particle-particle distance $l \approx (\frac{2\pi}{\sqrt{3}\phi_s})^{1/2}a$. For all simulations adopting Equation (2.14) in the current thesis, we have $\phi_s = 0.5$ which gives $l \approx 2.69a$. The average distance of a particle to its second nearest neighbour is $(\frac{\sqrt{3}+2}{2})l \approx 5a$, therefore setting $r_c = 5a$ is fairly an optimal choice.

A further advantage of using a linear particle-particle interaction model is that the surface pressure depends on the surface fraction ϕ_s, but is independent of a/R, where R is the radius of fluid interface curvature (e.g. drop radius). This property will be very useful to the studies in the chapter 4. The proof is provided in Appendix (A.2).

At the end, the exact equation of motion of a particle used in FIPI-Track is given as:

$$6\pi\mu a\left(\dot{\mathbf{x}}_p - \mathbf{u}_f\left(\mathbf{x}_p\right)\right) = m_p\mathbf{g} + \mathbf{F}_{pi} + \mathbf{F}_{pp}. \tag{2.15}$$

2.1.3 FIPI-Fluid

With the adoption of phase field method, the influence of the surface tension of fluid interface can be represented by continuous normal forces acting at the interface region. By treating each particle as a Lagrangian point, we do no need to enforce no-slip boundary condition at the surface of the particle. Instead, the influence of each particle suspended in the fluid is represented by a delta force acting at the location of each particle. As a result, the effects of both fluid interface and colloidal particles are incorporated into the Stokes equation. Plus the continuity equation we have

$$\mathbf{0} = -\nabla p + \mu\nabla^2\mathbf{u} + \mathbf{f}_c - \sum_{j=1}^{N}\left(\mathbf{F}_{pi}^{(j)} + \mathbf{F}_{h}^{(j)}\right)\delta(\mathbf{x} - \mathbf{x}_p^{(j)}) \tag{2.16}$$

$$0 = \nabla \cdot \mathbf{u} \tag{2.17}$$

where $\mathbf{f}_c$ is the force density due to the surface tension of bare fluid interface and is calculated as [137]:

$$\mathbf{f}_c = \xi\nabla\phi = \left(\frac{\lambda}{\epsilon^2}(\phi^3 - \phi) - \lambda\nabla^2\phi\right)\nabla\phi. \tag{2.18}$$

There are many forms of continuous surface tension forces that are equivalent to each other in phase field methods [143]. The one above is chosen for FIPI-Fluid due to that both ξ and $\nabla\phi$ are readily available from Equation (2.1). Because ξ is a scalar, and isosurfaces of ϕ are parallel to the fluid interface, the force $\mathbf{f}_c = \xi\nabla\phi$ acts along the normal to the fluid interface. In the sharp-interface limit $\epsilon \to 0$, it can be shown [84] that

$$\xi\nabla\phi = -\mathbf{n}\kappa\gamma\delta(z) \tag{2.19}$$

where κ is the mean curvature of the fluid interface, $\mathbf{n}$ is the unit normal vector to the fluid interface pointing towards the convex side, and $\delta(z)$ is the one-dimensional Dirac delta function whose argument z is the coordinate normal to the fluid interface.

It is noted that the two forces in the summation term in Equation (2.16) are exactly the forces exerted on a single particle due to surrounding fluid, hence the minus sign in front of the summation.

Since the fluid interface is implicitly captured by FIPI-Interface and the effects of particles are modelled as point forces, there is no need to enforce any kinds of fluid-fluid or fluid-solid boundary conditions and Equation (2.16) is valid anywhere within the entire domain.

2.1.4 Modulation of Surface Tension by FIPI method

Despite of the modelling at particle scales, FIPI can still capture the modulation of surface tension by absorbed particles. This can be understood by first considering the relation between surface tension and pressure across the surface for a continuous surface tension field, and then considering a similar relation for the case in which the surface tension is due particle-particle interactions along the fluid interface.

Consider a curved patch of fluid interface A bounded by a line contour ∂A. For an homogeneous surface tension γ (acting tangentially to the fluid interface), the surface divergence theorem [144] reads

$$\int_{\partial A} \gamma \mathbf{t} dl = -\int_{A} \gamma \kappa \mathbf{n} dA \tag{2.20}$$

where $\kappa = \nabla \cdot \mathbf{n}$ is the local mean curvature, $\mathbf{t}$ is the unit vector parallel to the

interface pointing out of A, and $\mathbf{n}$ is the unit normal vector perpendicular to the interface and pointing towards the convex side of the interface. Equation (2.20) implies that surface stresses that act tangentially to the fluid interface can be translated into a force normal to the interface, and vice versa. This is the idea behind many one-fluid methods in which surface tension effects are modelled as a distributed normal force, including FIPI. In the field of computational multiphase flow science, the idea was first applied in the pioneering work of Brackbill and coworkers [145]. From Equation (2.20), considering an infinitesimal area element, The force per unit area exerted by capillary forces in the direction $\mathbf{n}$ is

$$\Delta p_\gamma = -\kappa\gamma \tag{2.21}$$

as can be easily seen from Equation (2.20) taking A to be infinitesimal.

Similarly, the surface stress exerted by a monolayer of particles absorbed on fluid interface can be translated into a normal (pressure) force acting on the fluid interface.

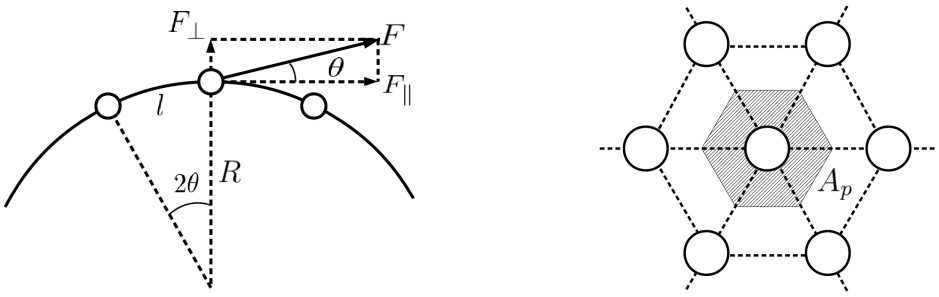

(a) Cross sectional view (b) Top view

Figure 2.3: Sketch of monolayer of particles distributed on curved interface with interaction forces.

To illustrate this point in a simple geometry, consider a monolayer of particles on a spherical interface with radius R. In the follows, we assume particles are ho-

mogeneously distributed on fluid interfaces and the local arrangement of particles is always axisymmetric around the direction normal to the fluid interface. Each particle occupies a surface area A_p (Figure 2.3(b)). Let us assume for simplicity that each particle interacts only with its first neighbours through repulsive forces. In this simple geometry the 2D surface pressure Π_s due to the particles (i.e. the lateral pressure due to tangential inter-particle forces) can be calculated as [146]

$$\begin{aligned}\Pi_s &= \frac{1}{4}\sum_{\alpha\neq\beta}^{N}\left[\mathbf{F}_{\parallel}^{\alpha\beta}\cdot(\mathbf{y}_s^{\beta}-\mathbf{y}_s^{\alpha})\right]G(\mathbf{x}_s-\mathbf{y}_s^{\alpha}) \\ &= \frac{NF_{\parallel}l}{4A_p}\end{aligned} \tag{2.22}$$

where G is the boxcar filter function taking value $1/A_p$ when $\mathbf{y}_s^{\alpha}$ falls inside control area and 0 outside, N is the coordination number, $F_{\parallel}$ is the tangential component of the inter-particle force between the test particle centred inside A_p and each neighbouring particle, l is the arc length distance from the test particle and its first neighbours. Because the inter-particle forces are repulsive, the surface pressure is positive.

Because the fluid interface is curved, the tangential component of the inter-particle forces produces a normal force on the test particle. The ratio of this normal force and A_p, multiplied by the number of nearest neighbours, is the local pressure Δp_p exerted by the particles on the fluid interface. Mathematically, the force per unit area in the direction $\mathbf{n}$ (unit normal towards the convex side) is

$$\Delta p_p = \frac{NF_{\perp}}{A_p}. \tag{2.23}$$

where $F_{\perp}$ is the normal force due to each particle pair. The force $F_{\perp}$ is just the

projection of the tangential forces into the normal. Simple geometry gives

$$F_\perp = \tan\left(\frac{l}{2R}\right) F_\parallel \simeq \frac{l}{2R} F_\parallel. \tag{2.24}$$

where we have assumed, as it is typically the case, that $l \ll R$. Combining Equation (2.22)(2.23)(2.24), and noticing that $\kappa = 2/R$ for a sphere, leads to

$$\Delta p_p = \Pi_s \kappa, \tag{2.25}$$

For $\Pi_s > 0$, Δp_p and Δp_γ have opposite sign (compare equations 2.21 and 2.25). Thus, for repulsive inter-particle forces, the presence of the particles leads, effectively, to a reduction in surface tension (leading to an effective surface tension of the particle-covered fluid interface $\gamma - \Pi_s$ smaller than the bare surface tension γ).

Examining the Stokes equation (2.16), the forcing terms $\mathbf{f}_c$ and $\sum_{j=1}^{N} \mathbf{F}_{pi}^{(j)} \delta(\mathbf{x} - \mathbf{x}_p^{(j)})$ have the same physical meaning of the pressures Δp_γ and Δp_p in the example above, respectively.

While the spherical geometry simplifies the derivation considerably, Equation (2.25) is valid more generally. A proof in 2D is given here to show the equivalence of $\mathbf{f}_c$ and the collection of delta-function forces coming from particles absorbed at fluid interface in Equation (2.16). Considering a general fluid interface in 2D (Figure 2.4), a pillow box control volume V encloses a patch A of the fluid interface. Within the CV the local curvature of the fluid interface is assumed to be $\kappa = 1/R$. A total number of N particles are uniformly distributed within the CV and they are in equilibrium under pairwise repulsive interaction forces with magnitude F_{pp}. Each particle has a number of N_c neighbouring particles.

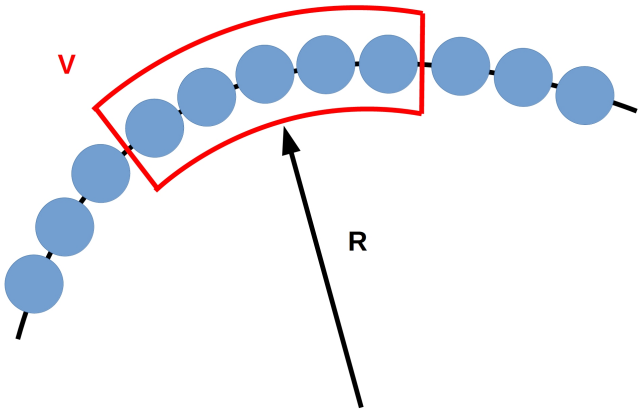

Figure 2.4: A schematic of a general fluid interface in 2D covered with particles. The control volume V is enclosed by red lines. The local fluid interface curvature is $1/R$.

Assuming static conditions for both fluid and particles, the integration of Equation (2.16) over the CV is

$$\mathbf{0} = \int_V \left\{ -\nabla p + \mathbf{f}_c - \sum_j^N \mathbf{F}_{pi}^{(j)} \delta \left(\mathbf{x} - \mathbf{x}_p^{(j)} \right) \right\} dV. \tag{2.26}$$

Neglecting the weight of the particles in Equation (2.15) and knowing that $\mathbf{f}_c = -\gamma\kappa\mathbf{n}\delta(z)$ in the sharp interface limit [78], we have

$$\mathbf{0} = \int_V \left\{ -\nabla p - \gamma\kappa\mathbf{n}\delta(z) + \sum_j^N \mathbf{F}_{pp}^{(j)} \delta \left(\mathbf{x} - \mathbf{x}_p^{(j)} \right) \right\} dV, \tag{2.27}$$

where $\mathbf{n}$ is the normal unit vector of the patch A pointing to the convex side and $\delta(z)$ is the 1D delta function and z is the coordinate normal to the fluid interface. Because $\mathbf{F}_{pp}^{(j)}$ is given by a pairwise interaction with each particle j within the CV,

$$\mathbf{0} = \int_V \left\{ -\nabla p - \gamma\kappa\mathbf{n}\delta(z) + \sum_j^N \sum_i^{N_c} \mathbf{F}_{pp}^{(ij)} \delta \left(\mathbf{x} - \mathbf{x}_p^{(j)} \right) \right\} dV. \tag{2.28}$$

Because the particles are residing on the fluid interface, we have

$$\mathbf{0} = \int_A \left\{ -\Delta p \mathbf{n} - \gamma \kappa \mathbf{n} + \sum_j^N \sum_i^{N_c} \mathbf{F}_{pp}^{(ij)} \delta_A \left(\mathbf{x} - \mathbf{x}_p^{(j)} \right) \right\} dA, \tag{2.29}$$

where Δp is the pressure difference between convex and concave side of the fluid interface, $\delta_A(\mathbf{x} - \mathbf{x}_p^{(j)})$ is a 2D delta function on the patch A. The force from particle i to particle j can be decomposed into

$$\mathbf{F}_{pp}^{(ij)} = \mathbf{F}_{pp}^{(ij),\parallel} + \mathbf{F}_{pp}^{(ij),\perp}. \tag{2.30}$$

At equilibrium, $\mathbf{F}_{pp}^{(j),\parallel} = \mathbf{0}$ because the particles do not translate parallel to the interface. The perpendicular component can be expressed as

$$\mathbf{F}_{pp}^{(ij),\perp} = F_{pp}^{(ij)} \frac{l_{pp}^{(ij)}}{2R} \mathbf{n}^{(j)} = \frac{F_{pp}^{(ij)} l_{pp}^{(ij)}}{2} \kappa \mathbf{n}^{(j)}, \tag{2.31}$$

where $l_{pp}^{(ij)}$ is the distance between centres of particle i and particle j. The integration 2.29 now becomes

$$\mathbf{0} = \int_A \left\{ -\Delta p \mathbf{n} - \gamma \kappa \mathbf{n} + \sum_j^N \sum_i^{N_c} \frac{F_{pp}^{(ij)} l_{pp}^{(ij)}}{2} \kappa \mathbf{n}^{(j)} \delta_A \left(\mathbf{x} - \mathbf{x}_p^{(j)} \right) \right\} dA. \tag{2.32}$$

Since $l_{pp}^{(ij)}$ is constant within the patch because the particles are homogeneously distributed and $F_{pp}^{(ij)}$ depends only on $l_{pp}^{(ij)}$, we have

$$\mathbf{0} = \int_A \left\{ -\Delta p \mathbf{n} - \gamma \kappa \mathbf{n} + \frac{F_{pp} l_{pp}}{2} \sum_j^N \sum_i^{N_c} \kappa \mathbf{n}^{(j)} \delta_A \left(\mathbf{x} - \mathbf{x}_p^{(j)} \right) \right\} dA. \tag{2.33}$$

As long as the summation of supports of all $\delta_A\left(\mathbf{x}-\mathbf{x}_p^{(j)}\right)$ is equal to A, we have

$$\mathbf{0}=\int_A\left\{-\Delta p\mathbf{n}-\gamma\kappa\mathbf{n}+\frac{F_{pp}l_{pp}}{2}NN_c\kappa\mathbf{n}\frac{1}{A}\right\}dA. \tag{2.34}$$

The surface pressure of a particle monolayer in 2D is calculated as

$$\begin{aligned}\Pi_s&=\frac{1}{A}\frac{\sum_i\sum_{j\neq i}F_{pp}^{(ij)}l_{pp}^{(ij)}}{2}\\&=\frac{NN_cF_{pp}l_{pp}}{2A}.\end{aligned} \tag{2.35}$$

Equation (2.34) now becomes

$$\mathbf{0}=\int_A\left\{-\Delta p\mathbf{n}-\gamma\kappa\mathbf{n}+\Pi_s\kappa\mathbf{n}\right\}dA. \tag{2.36}$$

Since the choice of the CV and the patch is arbitrary, we have

$$0=-\Delta p-\gamma\kappa+\Pi_s\kappa, \tag{2.37}$$

which is the Young-Laplace equation when particles are present on fluid interfaces. The above derivation shows that a collection of singular repulsive forces distributed uniformly on a fluid interface can be described by a surface pressure on the fluid interface. The surface pressure is counteracting the surface tension and the effective surface tension $\gamma-\Pi_s$ determines the Laplace pressure across the fluid interface.

2.2 Numerical Implementation

First of all, the system of equations solved in FIPI is listed below:

$$\begin{cases} \textbf{FIPI-Interface:} \\ \dfrac{\partial \phi}{\partial t} + \mathbf{u} \cdot \nabla \phi = \nabla \cdot M \nabla \left(\dfrac{\lambda}{\epsilon^2} \left(\phi^3 - \phi \right) - \lambda \nabla^2 \phi \right) \\ \textbf{FIPI-Track:} \\ 6\pi\mu a \left(\dot{\mathbf{x}}_p^{(j)} - \mathbf{u}_f(\mathbf{x}_p^{(j)}) \right) = m_p^{(j)} \mathbf{g} + \mathbf{F}_{pi}^{(j)} + \mathbf{F}_{pp}^{(j)} \text{ for } j = 1, 2, \cdots, N \\ \textbf{FIPI-Fluid:} \\ \mathbf{0} = -\nabla p + \mu \nabla^2 \mathbf{u} + \mathbf{f}_c \underbrace{- \sum_{j=1}^{N} \left(\mathbf{F}_{pi}^{(j)} + \mathbf{F}_h^{(j)} \right) \delta(\mathbf{x} - \mathbf{x}_p^{(j)})}_{\text{particle forcing terms}} \\ 0 = \nabla \cdot \mathbf{u} \end{cases} \tag{2.38}$$

The entire program is written in C++ from scratch by the author. Currently all simulations by FIPI are set up in 3D periodic physical domain. The uniform and orthogonal mesh is adopted. The Fourier spectral method is used to solve the Cahn-Hilliard equation (2.1) and Stokes equation (2.16). The spectral method offers more accurate numerical solutions for moderate density of meshes than other common numerical schemes [147]. With the readily available numerical package FFTW [148], the multi-threading computation of fast Fourier transform (FFT) can be implemented very easily. Although the spectral method is only applicable to periodic domain on a uniform structured grid, this restriction should not be a big hurdle for the simulations of the homogeneous colloidal suspensions.

With Fourier spectral method, all field variables are transformed into frequency space by performing FFT before further algebraic operations. Taking ϕ as an

example, the FFT is done by

$$\phi_{\mathbf{k}} = \sum_{\mathbf{n}=0}^{\mathbf{N}-1} \phi_{\mathbf{n}} e^{-2\pi i \mathbf{k}\cdot\mathbf{n}/\mathbf{N}} \tag{2.39}$$

where index $\mathbf{n}$ and $\mathbf{k}$ represent the location vector in physical space and wave vector in frequency space respectively, i is the unit complex number and $\mathbf{N} = (N_1, N_2, N_3)$ is the vector representing the total number of grid points in three orthogonal directions. Here we have $\mathbf{n}/\mathbf{N} = (n_1/N_1, n_2/N_2, n_3/N_3)$.

Let us denote $\phi_{\mathbf{k}}$ collectively by $\hat{\phi}$. In the follows the same notation rule will be applied to other transformed field variables.

The continuous field ϕ in Equation (2.1) is spatially discretised in physical space onto the computational grid and then transformed into Fourier space by performing FFT. In Fourier space Equation (2.1) becomes

$$\frac{\partial \hat{\phi}}{\partial t} + \{\mathbf{u}\cdot\nabla\phi\}_k = -k^2 M \left\{ \frac{\lambda}{\epsilon^2}(\phi^3 - \phi) \right\}_k - k^4 M \lambda \hat{\phi} \tag{2.40}$$

where $\{\}_k$ is the Fourier transform of the nonlinear parts inside bracket and $k = |\mathbf{k}|$ is the wave vector magnitude. Calculation of the non-linear terms are carried out in physical space before they are transformed back into the Fourier space.

The time derivative term $\frac{\partial \hat{\phi}}{\partial t}$ is discretised by a second-order backward differencing formula (BDF). The forth-order gradient term is treated implicitly while nonlinear terms are treated explicitly by a two-step Adam-Bashforth (AB) method.

Now Equation (2.40) becomes

$$\frac{3\hat{\phi}^{n+1} - 4\hat{\phi}^{n} + \hat{\phi}^{n-1}}{2\Delta t} = -(2\hat{e}^{n} - \hat{e}^{n-1}) - k^2 M(2\hat{f}^{n} - \hat{f}^{n-1}) - k^4 M\lambda\hat{\phi}^{n+1}$$
$$\hat{e}^{n} = \left\{ \mathbf{u}^{n} \cdot \left(-i\mathbf{k}\hat{\phi}^{n} \right)_{-k} \right\}_{k} \tag{2.41}$$
$$\hat{f}^{n} = \left\{ \frac{\lambda}{\epsilon^2} \left((\phi^{n})^3 - \phi^{n} \right) \right\}_{k}$$

where $()_{-k}$ represents the inverse Fourier transform of the terms inside the bracket.

Due to the presence of the non-linear terms in Equation (2.40), it is expected that aliasing errors may arise during the pseudo-spectral computation. However, the problem is not as severe as in the direct simulation of Navier-Stokes equation [149]. The reason is that in most of the time ϕ will be constant across most of the computational domain and only varies swiftly from -1 to 1 across a narrow interface region. The Fourier transform of ϕ will be approximately similar to that of a sign function which decays extremely fast with increasing wave number. Therefore for simulations with enough separation of scales between length of domain and interface thickness, the nonlinear term is usually well resolved in frequency space. As a result there is no need to eliminate the high frequency components of the nonlinear term in Fourier space. The above explanation is confirmed in the simulations as no anomalies have been encountered even without the use of zero-padding technique.

There are a few important dimensionless parameters for the phase field model. The first one is Cahn number, defined as the ratio of thickness ϵ of the fluid interface and the length scale of interest L (domain size, radius of the interface curvature, etc).

$$Cn = \frac{\epsilon}{L} \tag{2.42}$$

While in reality the fluid interface has atomic thickness, in a phase-field method the numerical thickness of the fluid interface is finite, and often quite large. This feature enables capturing the fluid interface at a less expensive computational cost but at the sacrifice of resolution. The choice for Cn is problem-dependent: the Cahn number has to be reasonably small to accurately reproduce the interfacial features of interest.

The second dimensionless parameter is related to the mobility parameter M in Equation (2.1). The mobility parameter is nondimensionalised as

$$S = \frac{\sqrt{M\mu}}{\epsilon}, \tag{2.43}$$

where S the ratio of the length scale $\sqrt{M\mu}$ characterising the diffusion of the chemical potential ξ to the thickness ϵ of the fluid interface [85, 150, 151]. Choosing S requires addressing competing requirements. Large values of S damp the fluid velocity near the fluid interface and lead to a loss of small scale features in the distribution of ϕ. Small values of S leave the fluid interface vulnerable to thinning or thickening under straining flows [85].

It should be noted that Equation (2.1)) which we are solving is a convection-diffusion equation, and the diffusion here carries a physical meaning at length scales much smaller than the fluid convection. Hence the balance between the convection and diffusion has to be considered. The diffusive time scale can be quantified as $t_d = \frac{\epsilon^3}{M\gamma}$. The convective time scale is $t_c = \frac{L}{U}$ with L being the length scale of interest. The Peclet number for Cahn-Hilliard equation can be defined as

$$Pe = \frac{t_d}{t_c} \tag{2.44}$$

which in turn can be expressed as

$$\begin{aligned} Pe &= \frac{\epsilon^2}{M\mu}\frac{U\mu}{\gamma}\frac{\epsilon}{L} \\ &= \frac{CaCn}{S^2} \end{aligned} \tag{2.45}$$

With Pe and Cn being prescribed for specific fluid problems, it can be noted that $S^2 \propto Ca$. The mobility parameter need to be adjusted according to the surrounding fluid velocity magnitude. This argument is in agreement with the scaling law proposed in [152].

From Equation (2.15), the instantaneous velocity of the particle at time step n can be explicitly calculated as

$$\mathbf{u}_p^n\left(t^n, \mathbf{x}_p^n\right) = \mathbf{u}_f\left(t^n, \mathbf{x}_p^n\right) + \frac{\mathbf{F}_{pi}\left(t^n, \mathbf{x}_p^n\right) + \mathbf{F}_{pp}\left(t^n, \mathbf{x}_p^n\right)}{6\pi\mu a}. \tag{2.46}$$

Evaluation of the undisturbed fluid velocity $\mathbf{u}_f$ at the particle location $\mathbf{x}_p$ is not an easy task. This quantity should account for the velocity disturbances induced by all the other particles and the motion of the fluid interface, but not the self-induced fluid velocity. Excluding the self-induced fluid velocity is possible in unbounded and single phase fluid environment [111, 153, 154], but in problems with fluid interfaces this clearly constitutes a major challenge. In the current thesis, this problem is not completely solved. Rather, it is tolerable to include the self-induced fluid velocity in $\mathbf{u}_f$ in simulations in which the total force $\mathbf{F}$ exchanged between the particle and the fluid (Equation (2.10)) is relatively small or the computational cell size Δx is sufficiently large. This is a common approach adopted in the simulations of particle-laden turbulent flows [102, 103, 155]. This second option, which is to set $\mathbf{u}_f = \mathbf{0}$, was adopted in the quasi-static problems considered in Chapter 4. The

magnitude of the self-induced particle velocity u' can be estimated to scale as $u' \sim \frac{\mathbf{F}}{\mu \Delta x}$. Calling U the flow created by an external field plus the disturbances induced by neighbouring particles, the self-induced fluid velocity does not practically cause problems if $\frac{u'}{U} \ll 1$. For a given fluid viscosity, this condition translates into a constraint on the ratio $\frac{\mathbf{F}}{\Delta x}$.

From Equation (2.11) we know a challenge to compute $\mathbf{F}_{pi}$ is to gain knowledge of the distance of the particle to the interface efficiently. We have found that having at our disposal a phase-field variable is very useful in this respect. The phase field variable at the centre of a particle j, $\phi^{(j)} = \phi(\mathbf{x}_p^{(j)}, t)$, contains information about the particle-interface distance and can be used to compute $d^{(j)} = \left|\mathbf{d}^{(j)}\right|$ if a suitable mapping between $\phi^{(j)}$ and $d^{(j)}$ can be found. A solution used in FIPI is given in the follows.

Assuming the phase field profile ϕ stays at or close to the equilibrium, we can assume $\phi \simeq \phi_{eq} = \tanh(\frac{x}{\sqrt{2}\epsilon})$ in the proximity of the fluid interface. An effective interfacial region (Figure 2.5) can be defined where the distance d to the zero level set of ϕ is $d < 2\sqrt{2}\epsilon$ (this corresponds to $|\phi| < 0.964$). Within this region, the phase field variable at the location of the solid particle can be accurately translated into a distance to the fluid interface. The distance magnitude of the particle j to the local fluid interface can be calculated as

$$d^{(j)} = \left| \frac{\sqrt{2}}{2} \epsilon \log \frac{1 + \phi^{(j)}}{1 - \phi^{(j)}} \right|. \tag{2.47}$$

The unit normal vector to the interface is calculated as $\mathbf{n}^{(j)} = -\frac{\phi^{(j)}}{|\phi^{(j)}|} \frac{\nabla \phi(\mathbf{x}^{(j)}, t)}{|\nabla \phi(\mathbf{x}^{(j)}, t)|}$. Therefore, both the values of ϕ and $\nabla \phi$ at the centre of the particle are needed to determine $\mathbf{d}^{(j)} = d^{(j)} \mathbf{n}^{(j)}$.

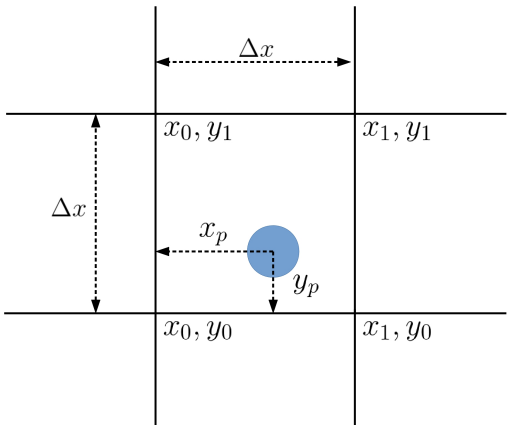

Figure 2.6: Schematic of a particle located arbitrarily within a grid cell.

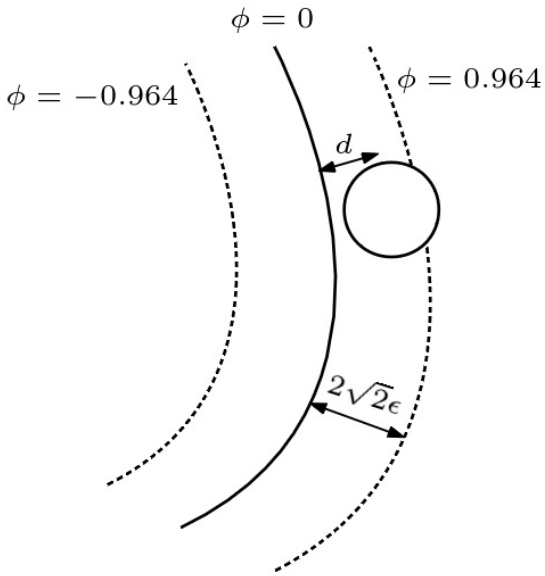

Figure 2.5: Sketch of mapping between local phase field value at particle position and its distance to interface

One requirement for the mapping between $\phi^{(j)}$ and $d^{(j)}$ to work is that the particle radius a must be smaller than the half of the thickness of the interfacial region, $a < 2\sqrt{2}\epsilon$. The reason for this is that as $\phi^{(j)} \to \pm 1$ the distance $d^{(j)}$ diverges to infinity according to Equation (2.47).

The calculation of the value of the fields ϕ and $\nabla\phi$ at the location of the parti-

cle centre requires an interpolation scheme. A trilinear interpolation scheme which was also implemented in [155–157], is adopted. Other higher order interpolation schemes can produce more accurate results, but would increase the computational cost. With reference to Figure 2.6, a 2D version of the interpolation scheme (bilinear) for calculating the value of ϕ at the location $\mathbf{x}_p = (x_p, y_p)$ of a particle centre reads

$$\begin{aligned}\phi(x_p, y_p) = &\left(1 - \frac{x_p}{\Delta x}\right)\left(1 - \frac{y_p}{\Delta x}\right)\phi(x_0, y_0) \\ &+ \frac{x_p}{\Delta x}\left(1 - \frac{y_p}{\Delta x}\right)\phi(x_1, y_0) \\ &+ \left(1 - \frac{x_p}{\Delta x}\right)\frac{y_p}{\Delta x}\phi(x_0, y_1) \\ &+ \frac{x_p}{\Delta x}\frac{y_p}{\Delta x}\phi(x_1, y_1),\end{aligned} \tag{2.48}$$

where Δx is the length of a unit cell edge. All other field variables are interpolated at the location of the particle in the same way.

The last term need to be closed in Equation (2.46) is $\mathbf{F}_{pp}$. For each particle j, it is equal to the sum of all the pairwise interaction forces $\mathbf{F}_{pp}^{(ij)}$ between the current particle j and its neighbours.

Calculating $\mathbf{F}_{pp}$ for each particle j requires the knowledge of the list of particles that are located within the cut-off distance r_c from particle j. A naive pairwise scan over total N particles will give a computational complexity of the order of $\mathcal{O}(N^2)$.

To reduce the computational overhead, a cell-list sorting method is employed [158]. The computational domain is first uniformly subdivided into cells with edge length greater to the cut-off distance of the interaction. All particles are then sorted into these cells. For each particle, a distance check is performed between

the current particle and all particles in the neighbouring cells. Because the edge of the cell is at least equal to the cut-off radius of the interactions, no particles within the cut-off radius are missed during the check. If the distance between two particles is smaller than the cut-off radius, their interaction forces is calculated. A schematics of the cell-list sorting method is shown in Figure 2.7.

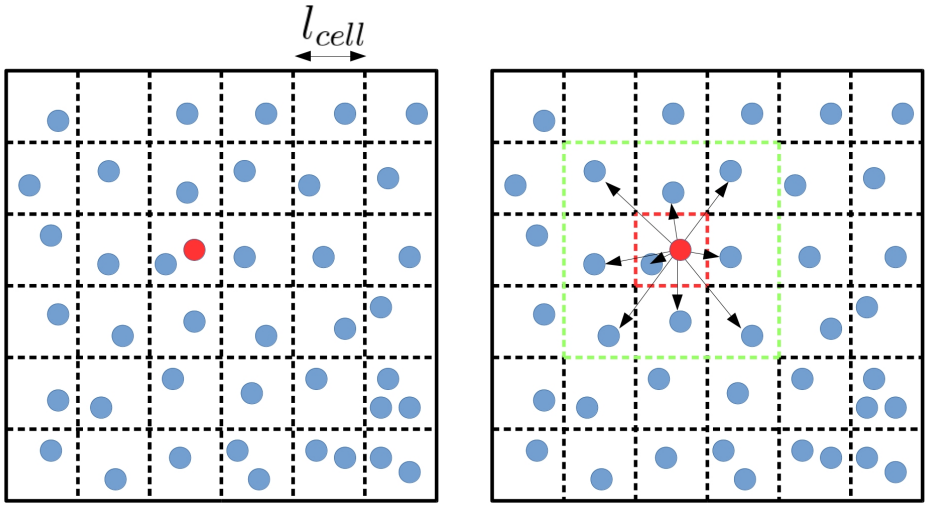

Figure 2.7: Cell-list sorting method. Left: The computational domain is divided into smaller sorting cells (dashed line). The test particle is marked in red. Right: a distance check will be performed between the test particle and all particles in the neighbouring cells (enclosed by green dashed line) and the current cell (enclosed by red dashed line).

The pseudo code of the cell-list method for calculation of interaction forces for a cluster of particles is illustrated in Algorithm (1).

With all the terms in Equation (2.46) closed, particle velocity $\mathbf{u}_p$ is computed and we can proceed to calculate the displacement of the particle. Heun's method

Algorithm 1 Cell-List Sorting

```
Loop over all particles :
    Calculate i_cell, j_cell from the coordinate of current particle
    Append the particle index to the linked list of cell i_cell, j_cell


Loop over all particles :
    Loop over all neigbouring cells of the current particle j :
      Loop over all particles of the current cell :
        Calculate the distance between the two particles
        If distance < r_c :
          Calculate their interaction force
```

is adopted for time marching the displacement. It is essentially a two-stage Runge-Kutta method. In the first stage, an estimate of the particle position at the next time step is given as

$$\bar{\mathbf{x}}_p^{n+1} = \mathbf{x}_p^n + \delta t \mathbf{u}_p^n \left(t^n, \mathbf{x}_p^n\right), \tag{2.49}$$

where δt is the unit time step. In the second stage, the position of the particle is calculated with second-order accuracy using the estimate obtained in the first stage:

$$\mathbf{x}_p^{n+1} = \mathbf{x}_p^n + \frac{\delta t}{2}\left(\mathbf{u}_p\left(t^n, \mathbf{x}_p^n\right) + \mathbf{u}_p\left(t^{n+1}, \bar{\mathbf{x}}_p^{n+1}\right)\right). \tag{2.50}$$

The Stokes equation (2.16) is also solved by spectral method as the Cahn-Hilliard equation (2.1) in FIPI-Interface. After solving the equations in FIPI-Interface and FIPI-Track, two forcing terms on the right hand side of equation (2.16) can already be calculated explicitly. However, an additional step is needed before we can solve the Equation (2.16).

In contrast to the continuous form of the surface tension force (Equation (2.18)), the forcing terms from particles in the Stokes equation (2.16) are delta-function forces that need to be regularised and projected back to the computational grids. As suggested by [159], only when the weights used in the projection scheme are

equal to the weights used in the interpolation scheme, the point-particle algorithm would be consistent. Therefore the same stencil used for the interpolation scheme is adopted for the projection scheme in FIPI. As an example in 2D, the force $\mathbf{F}$ from a particle located at $\mathbf{x}_p = (x_p, y_p)$ is projected onto the nearby grid points (Figure 2.6) in the following way:

$$\begin{aligned}
\mathbf{f}(x_0, y_0) =& \mathbf{F}\frac{1}{\Delta V}\frac{1-x_p}{\Delta x}\frac{1-y_p}{\Delta x} \\
\mathbf{f}(x_1, y_0) =& \mathbf{F}\frac{1}{\Delta V}\frac{x_p}{\Delta x}\frac{1-y_p}{\Delta x} \\
\mathbf{f}(x_0, y_1) =& \mathbf{F}\frac{1}{\Delta V}\frac{1-x_p}{\Delta x}\frac{y_p}{\Delta x} \\
\mathbf{f}(x_1, y_1) =& \mathbf{F}\frac{1}{\Delta V}\frac{x_p}{\Delta x}\frac{y_p}{\Delta x}
\end{aligned} \tag{2.51}$$

where ΔV is the volume of a single computational cell. This projection scheme regularise the delta-function force into a smooth function whose compact support is the region occupied by a computational cell.

Let us denote the total force density from all forcing terms in Equation (2.16) as $\mathbf{f}_{total}$. Applying the divergence operation on Equation (2.16) and combining it with the continuity equation we have

$$\nabla^2 p = \nabla \cdot \mathbf{f}_{total}, \tag{2.52}$$

which after being transformed into Fourier space is

$$-k^2 \hat{p} = i\mathbf{k} \cdot \hat{\mathbf{f}}_{total}. \tag{2.53}$$

The pressure field is expressed as

$$\hat{p} = -\frac{i\mathbf{k} \cdot \hat{\mathbf{f}}_{total}}{k^2}. \tag{2.54}$$

Multiplying both sides of Equation (2.54) by $i\mathbf{k}$ gives

$$i\mathbf{k}\hat{p} = \frac{\mathbf{k}\left(\mathbf{k}\cdot\hat{\mathbf{f}}_{total}\right)}{k^2} \tag{2.55}$$

where the left hand side is the gradient of the pressure in Fourier space, the right hand side is exactly the component of $\hat{\mathbf{f}}_{total}$ that is parallel to the wave vector $\mathbf{k}$. Transforming Equation (2.16) into Fourier space and combining it with Equation (2.55), the fluid velocity field in Fourier space can be computed as

$$\hat{\mathbf{u}} = \frac{1}{\mu k^2}\left(\hat{\mathbf{f}}_{total} - \frac{\mathbf{k}\left(\mathbf{k}\cdot\hat{\mathbf{f}}_{total}\right)}{k^2}\right). \tag{2.56}$$

The flow field is assumed to have zero mean value, therefore we set $\hat{\mathbf{u}} = \mathbf{0}$ when $k = 0$. The fluid velocity in physical space can then be computed by performing an inverse FFT of $\hat{\mathbf{u}}$.

2.3 Validation Studies

A challenge faced during the development of FIPI has been the lack of analytical results that could be used for validating simulations of fluid interfaces populated by particles. Five validation cases are discussed in this section. A simulation case to qualitatively prove that FIPI can capture the jamming of the fluid interface and a code performance study are given at the end.

2.3.1 Test 1: Deformation of a Spherical Drop in a Simple Shear Flow

To validate the Navier-Stokes/Cahn-Hilliard solver, without the particle, I have considered the deformation of a drop in simple shear flow. The deformation of an initially spherical drop in homogeneous shear flow is a classic problem that has been studied extensively in literature [160–162]. A single spherical drop is immersed in another fluid phase. Under the homogeneous shear flow, the drop will deform into an ellipsoid according to the direction and magnitude of the imposed shear. For current studies only the Stokes flow problem is considered.

The set-up of the problem is illustrated in Figure 2.8. The simulations are carried out in 3D, a linear shear flow (Figure 2.8 Right) with a constant shear rate is imposed onto the entire computational domain (Figure 2.8 Left) of size $[2, 2, 2]$. A spherical droplet of radius 0.5 is initially positioned in the centre of the domain. The total grid size is $64 \times 64 \times 64$. Periodic boundary conditions are enforced in all three directions. No particles are included in the current simulations. The density of the drop is the same as that of the surrounding fluid.

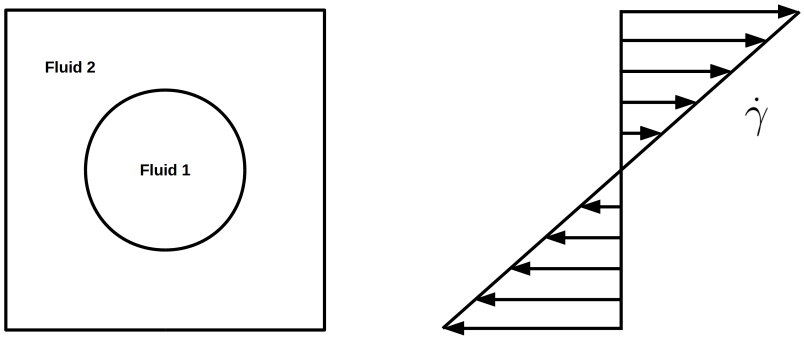

Figure 2.8: Sketch of simulation of droplet under pure shear flow.

The degree of deformation of the drop can be quantified by a deformation

parameter $D = (L - S)/(L + S)$, where L and S are the longest and shortest axes of the ellipsoidal droplet. The relation between D and the capillary number Ca, valid for $Ca \ll 1$, was found analytically by G.I. Taylor [160]. It is given by

$$D = \frac{35}{32} Ca \tag{2.57}$$

The results of the simulations with FIPI are reported in Figure 2.9, and compared to Equation (2.57). The computed deformation parameter D is in good agreement with the theory. The relative error is below 5% in all cases.

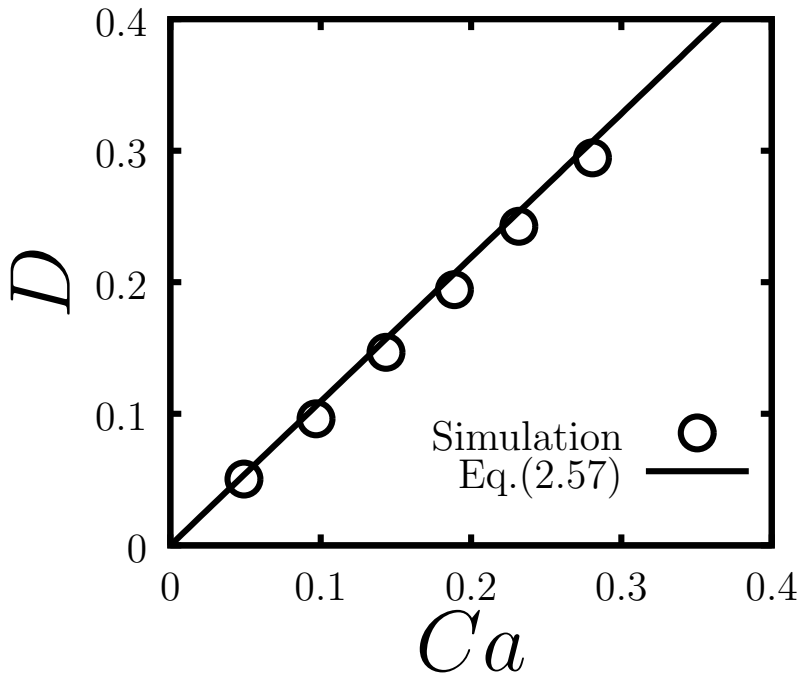

Figure 2.9: Deformation parameter versus capillary number for a initial spherical drop in shear flow. The solid line is the analytical solution valid for $Ca \ll 1$.

2.3.2 Test 2: Modulation of the Surface Tension by a Particle Monolayer Embedded in a Spherical Fluid Interface

In this test, simulations are carried out to show how the Laplace pressure is changed by surface pressure of a particle monolayer covering the surface of a spherical drop.

The simulation set-up is as sketched in Figure 2.10. A spherical drop of radius R is initially put at the centre of the computational domain of size $[2\pi, 2\pi, 2\pi]$ with grid size $64 \times 64 \times 64$. The surface tension of the drop is γ. The particle-particle interaction model in Equation (2.14) is implemented in the current simulations, with $r_c = 5a$ and k_c ranging from 0 to 0.5γ to induce different magnitude of surface pressure Π_s.

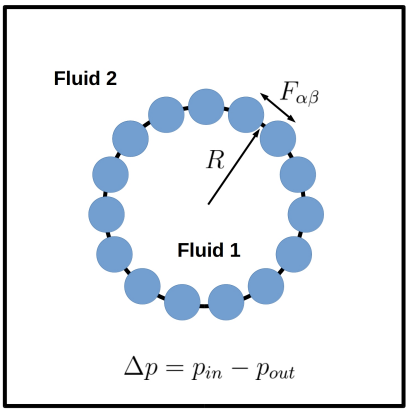

Figure 2.10: Simulation set-up for measuring the Laplace pressure Δp as a function of the surface pressure Π_s created by particle monolayer. The solid particles are coloured in light blue.

The surface pressure Π_s is the isotropic component of the surface stress tensor $\boldsymbol{\sigma}$ originating from the conservative inter-particle forces. The surface stress due to the particles can be decomposed into an isotropic and a deviatoric component as $\boldsymbol{\sigma} = -\Pi_s \mathbf{I} + \boldsymbol{\sigma}^D$. The deviatoric component $\boldsymbol{\sigma}^D$ is associated to the shear elasticity

of the particle monolayer. The surface pressure Π_s is the stress response of a particle monolayer to an isotropic dilatation or compression. In current simulation the surface tension of the bare interface γ affects only the isotropic component of the surface stress of the composite interface. The particles are assumed to be much larger than the molecules composing the bare interface, so the effects of the particles and of the bare interface on the effective surface tension can be taken to be additive.

At a surface point $\mathbf{x}_s$, the stress tensor can be calculated (see Appendix (A.1)) as

$$\boldsymbol{\sigma} = \frac{1}{2}\sum_{\alpha=1}^{N}\sum_{\beta\neq\alpha}^{N}\mathbf{F}_{\alpha\beta}(\mathbf{y}_s^{\beta}-\mathbf{y}_s^{\alpha})G(\mathbf{x}_s-\mathbf{y}_s^{\alpha}). \tag{2.58}$$

In this expression, $\mathbf{F}_{\alpha\beta}$ is the force on particle α due to particle β. The surface position vectors $\mathbf{y}_s^{\alpha}$ and $\mathbf{y}_s^{\beta}$ locate the centers of particles α and β, respectively. The summation is over all the particles in the monolayer. The function G is a smooth surface filter function with compact support which isolates a surface control region around $\mathbf{x}_s$. Typical choices for the filter function suggested by three-dimensional calculations are the box function and the Gaussian filter; the specific choice of filtering should not affect the definition of spatially-average quantities [49].

Our derivation of Equation (2.58) follows from recent work on bulk suspensions by Nott, Guazzelli and Pouliquen [51], who in turn extended work by Anderson and Jackson on suspension stresses due to particle-particle contacts [49, 50]. The derivation assumes pair-wise interactions; however, the formula is expected to hold more generally [51]. Equation (2.58) can be recognised as a version of the Irving-Kirkwood formula, here applied to a system of particles constrained to a curved surface.

In the calculations presented in the current investigation, G is a box function, constant and equal to $1/A_c$ in a curved surface element (the averaging region) of area A_c centred at $\mathbf{x}_s$ and zero otherwise. With G being a box function, we have

$$\boldsymbol{\sigma} = \frac{1}{2A_c} \sum_{\alpha} \sum_{\beta \neq \alpha}^{N} \mathbf{F}_{\alpha\beta} (\mathbf{y}_s^{\beta} - \mathbf{y}_s^{\alpha}). \tag{2.59}$$

where now the index α runs over all the particles within the averaging region, while β indexes particles that can be either inside or outside the averaging region A_c.

Taking the trace of Equation (2.59) and multiplying by $-1/2$ yields the following formula for the surface pressure of a 2D particle monolayer:

$$\Pi_s = -\frac{1}{4A_c} \sum_{\alpha} \sum_{\beta \neq \alpha}^{N} \mathbf{F}_{\alpha\beta} \cdot (\mathbf{y}_s^{\beta} - \mathbf{y}_s^{\alpha}). \tag{2.60}$$

The repulsion between the particles induces a surface pressure $\Pi_s > 0$ that acts to oppose the effect of the bare surface tension. The effective surface tension of the fluid-particle composite interface is given by

$$\gamma_{eff} = \gamma - \Pi_s. \tag{2.61}$$

As a result, the modified Young-Laplace equation for a spherical drop with radius R covered by solid particles can be written as

$$\Delta p = \frac{2\left(\gamma - \Pi_s\right)}{R}. \tag{2.62}$$

The Laplace pressure Δp, namely the difference in pressure between the inside and the outside of the drop, was computed from the simulation result for differ-

ent values of Π_s. The results are shown in Figure 2.11 with comparison to the theoretical prediction by Equation (2.62) and the agreement is excellent.

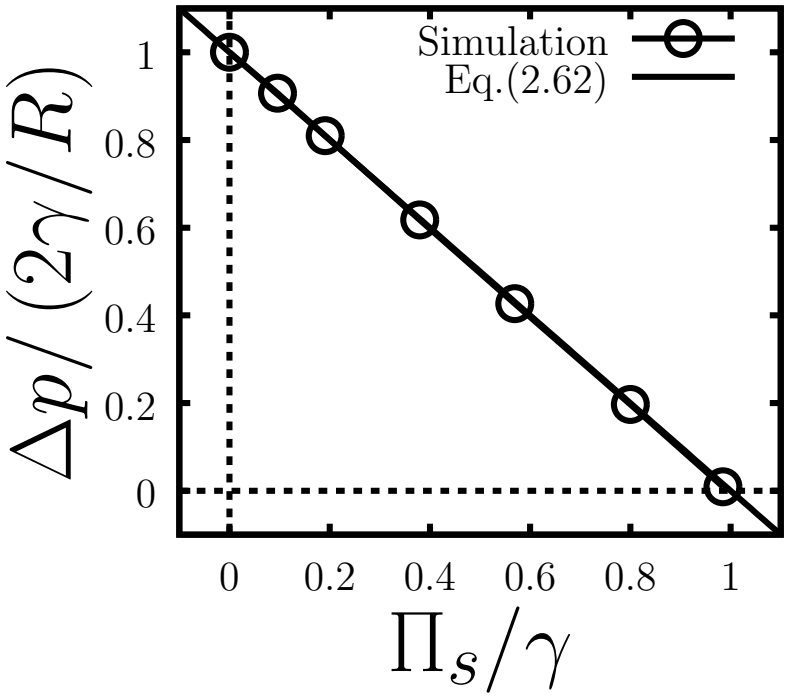

Figure 2.11: Laplace pressure of a spherical drop covered by a particle monolayer vs. particle-induced surface pressure. The solid line is Equation (2.62). The open circles are the simulation results.

2.3.3 Test 3: Deformation of a Flat Fluid Interface by a Single Particle Exerting a Normal Force

Here I simulate the deformation of a flat, horizontal fluid interface when a solid particle embedded in the interface "pushes" down on the fluid interface due to an external force (e.g. gravity). For this problem an analytical solution exists. A schematic of the problem is shown in Figure 2.12. The profile of the perturbed fluid interface is measured at steady state as a function of radial distance from the particle centre.

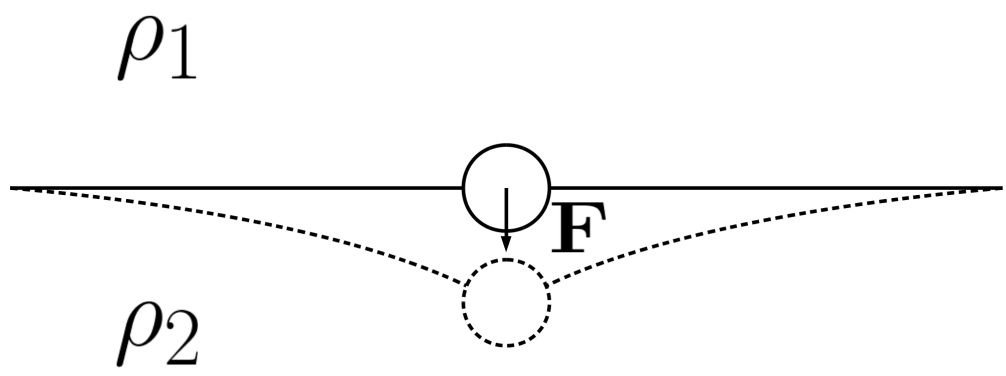

Figure 2.12: Pinching a solid particle away from fluid interface by an external force **F**.

A neutrally buoyant spherical particle of radius $a = \frac{\pi}{32}$ is placed on the flat fluid interface. The fluid above and below the fluid interface have densities ρ_1 and ρ_2, respectively. A constant external force **F** is exerted on the particle. The particle starts to move out of its equilibrium position, deforming the fluid interface. The time history of the maximum dip (at the location of particle) of the fluid interface is shown in Figure 2.13.

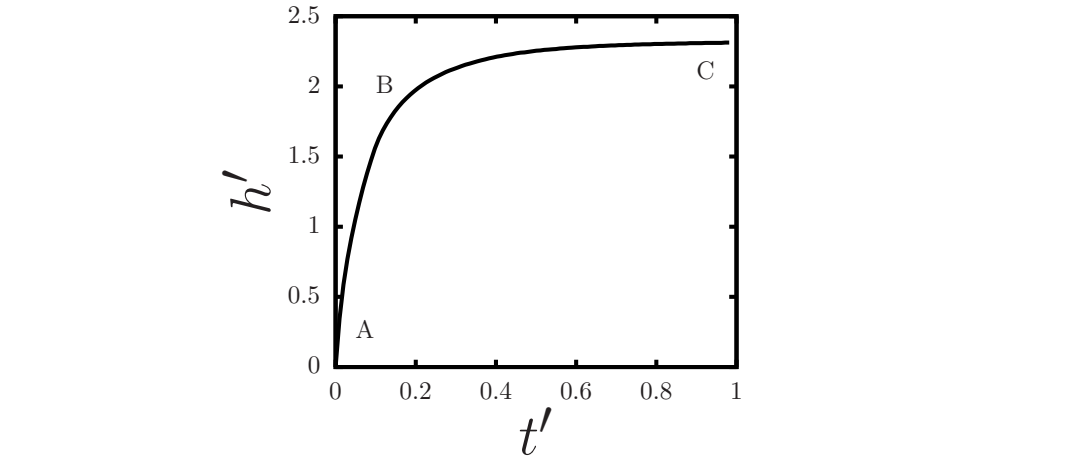

(a)

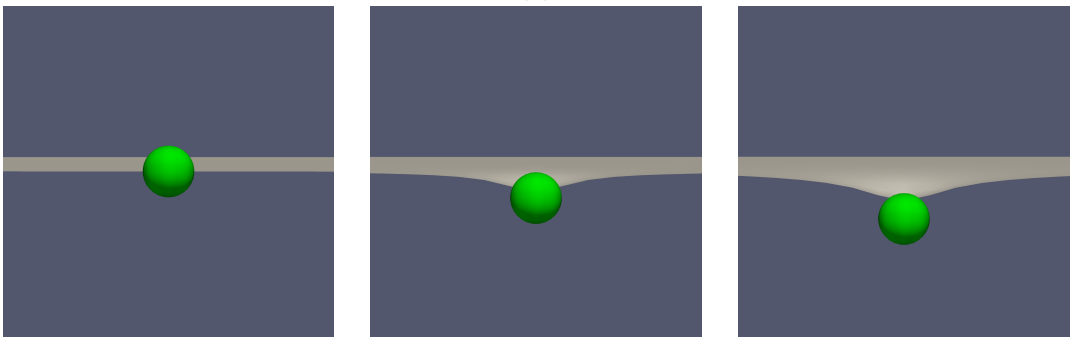

(b) $t' = 0$ (c) $t' = 0.1$ (d) $t' = 0.9$

Figure 2.13: (a)Time evolution of the maximum downward displacement of the fluid interface caused by exerting a downward force of magnitude F on the particle. The displacement of the fluid interface is normalised by $h^\star = \frac{F}{2\pi\gamma}$ and the time is normalised by $t^\star = \frac{\mu}{\Delta\rho g h^\star}$. The pictures of the particle laden interface at three different time instants are shown in (b)-(d), corresponding to A,B,C in (a).

At steady state, the interface profile is described by a screened Poisson equation in 2D,

$$\sigma\nabla^2 h = -\Delta\rho g h + F\delta(x). \tag{2.63}$$

The axisymmetric solution of this equation is

$$h(x) = \frac{F}{2\pi\gamma} K_0\left(\frac{|x|}{l_c}\right) \tag{2.64}$$

where K_0 is the modified Bessel function of the second kind and the screening length l_c is equal to the capillary length $\sqrt{\frac{\gamma}{\Delta\rho g}}$.

The steady state profile of the fluid interface is studied as a function of the two numerical parameters S and Cn.

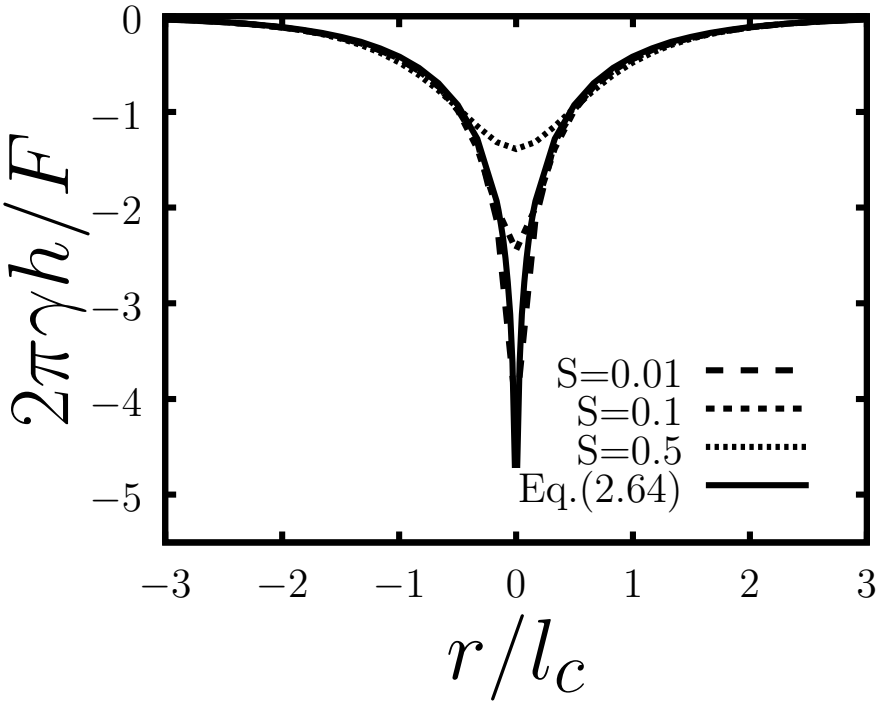

Figure 2.14: Normalised fluid interface profile as a function of s.

Figure 2.14 shows that for all values of S, the fluid interface profile produced by simulations matches the solution given by Equation (2.64) very well except near the location of the particle.

For regions close to the particle, the simulated fluid interface profile is approaching to analytical solution as $S \to 0$. It is evident that a smaller S makes the fluid interface become more "flexible", while a large value of S reduces the deformation.

The theoretical result given by Equation (2.64) suggests $h \to \infty$ as $r \to 0$.

In other words, the curvature generated by a singular perturbation at the point of action goes to infinity according to analytical solution. Within the context of phase field method, since the fluid interface has a finite thickness of the order of ϵ, any interfacial feature with length scales smaller than ϵ cannot be resolved. Near the fluid interface, for length scales of ϵ and below, the diffusion of the phase field due to the diffusion term in Equation (2.1) dominates the convective motions caused by the fluid flow. As a consequence, the singular curvature at the point of perturbation can only be captured by decreasing or eliminating the strength of the diffusion in Equation (2.1).

However, in practical applications it is not advised to reduce S excessively. As suggested by [85], a small mobility parameter will make the fluid interface become thick under external straining flow. Often the value of S has to be chosen pragmatically based on the particular problem at hand (i.e., through a convergence study).

On the other hand, the exact analytical solution can be asymptotically reached by reducing Cn towards zero while keeping S constant. This trend is shown in Figure 2.15. By reducing the fluid interface thickness, a higher curvature of fluid interface can be reproduced in simulation.

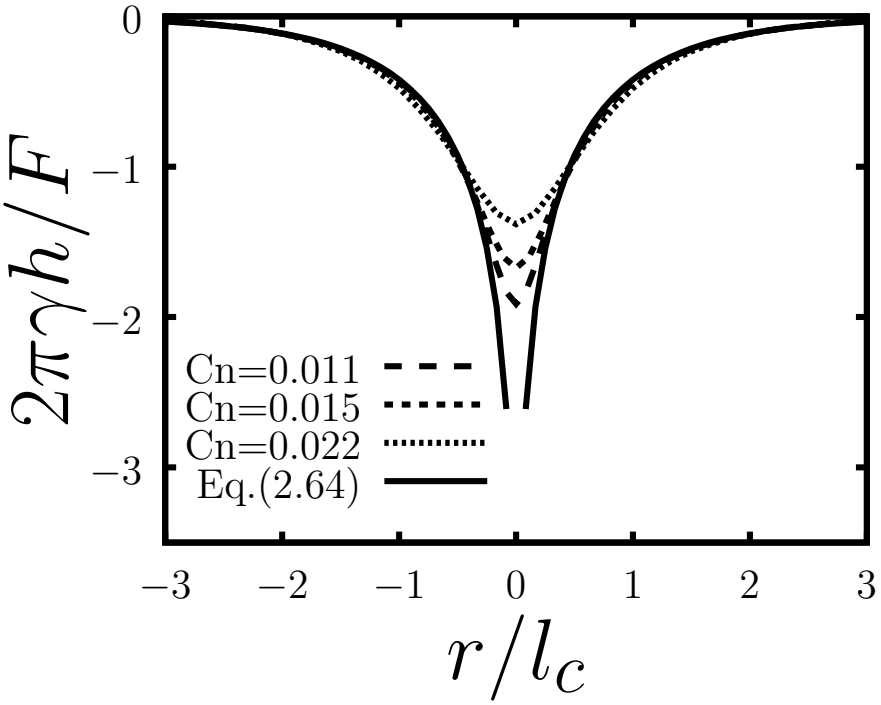

Figure 2.15: Normalised fluid interface profile as a function of Cn

2.3.4 Test 4: Pinching of a Spherical Drop by a Pair of Particles

An analytical solution of the shape of a drop pinched by two particles attached at the opposite ends is available [5]. This physical problem is well suited for studying how a curved fluid interface, compared to the flat fluid interface in previous subsection, deforms under the forces exerted by the attached solid particles. A qualitative schematic of the problem is shown in Figure 2.16.

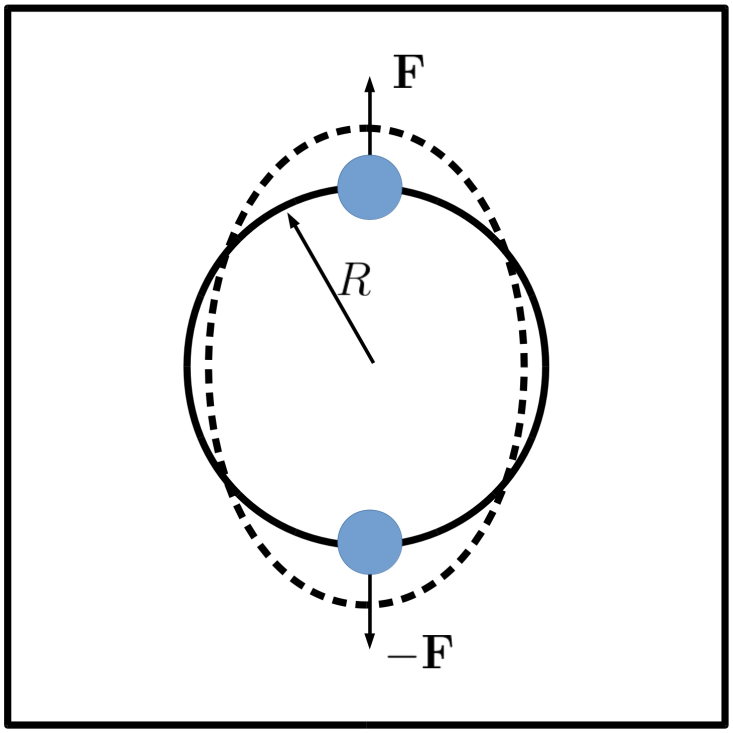

Figure 2.16: Schematic of the deformation of a spherical drop pinched by two solid particles attached at the opposite ends.

The FIPI simulation is set up as follows: a spherical drop of radius R is placed at the centre of computational domain $[2\pi, 2\pi, 2\pi]$, A pair of solid particles with radius $a = 0.1R$ are placed at the top and the bottom of the drop. At the start of the simulation, a force of constant magnitude $F = \pi\gamma a$ is exerted on both particles, either pulling them away or towards each other. At steady state, the equilibrium shape of the drop resembles an unduloid as given by Ref.[5]:

$$z = R_+ E(\psi, k_e) + \frac{cR^2}{R_-} F(\psi, k_e) \tag{2.65}$$

where $E(\psi, k_e)$ and $F(\psi, k_e)$ are incomplete elliptic integral of the first and second

hand respectively, and

$$\sin\psi = \sqrt{\frac{R_+^2 - R^2}{R_+^2 - R_-^2}} \tag{2.66}$$

$$k_e = \sqrt{1 - \frac{R_-^2}{R_+^2}}. \tag{2.67}$$

R_+ and R_- are the longer and shorter radius of the unduloid, respectively. Both radius are linked to an integration constant c as

$$R_+ = \sqrt{\frac{1 - c + \sqrt{1 - 2c}}{2}} R_0 \tag{2.68}$$

$$R_- = \sqrt{\frac{1 - c - \sqrt{1 - 2c}}{2}} R_0 \tag{2.69}$$

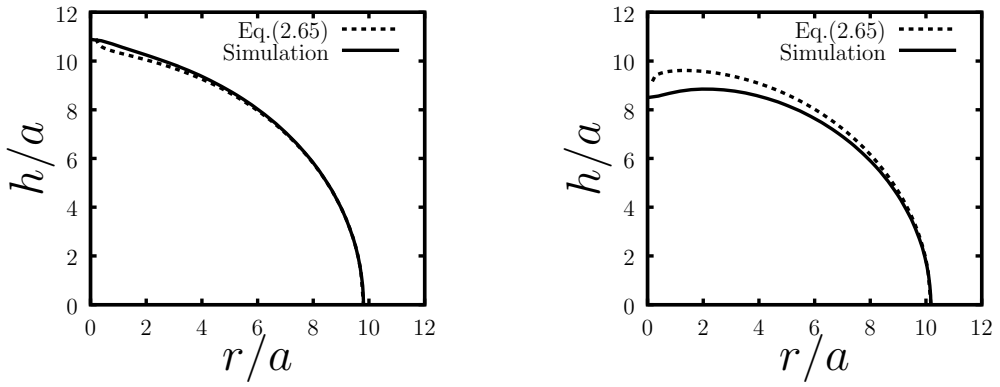

Figure 2.17: A quarter of the middle section of the drop shape when the drop is pinched by external forces acting on attached solid particles. (a) The drop is stretched by the pair of particles. (b) The drop is compressed by the pair of particles. Solid lines are FIPI simulation results and dashed lines are analytical solution of [5].

The simulation results of stretching the drop (Figure 2.17(a)) clearly gives a better agreement with the analytical solution than that of compressing the drop (Figure 2.17b). A significant error occurs near the particle, particularly in the

compression case. The possible reason is that the analytical solution presented here only concerns the minimisation of the free energy due to the presence of the fluid interface only. The discrepancy can possibly originate from the details related to the contact line.

2.3.5 Test 5: Effective Surface Tension of a Pendant Drop

The pendant drop is a drop held at the top (e.g. by the orifice of a pipette) and immersed in a gas or in a liquid that is lighter than the liquid the drop is made of. The shape of the drop is determined by the competition between surface tension and gravity. The pendant-drop tensiometry is a standard method for measuring the surface tension of surfactant-laden or particle-laden drops [163, 164].

A set of simulations of pendant drops covered with a monolayer of repulsive particles are carried out using FIPI. The objective of the current validation test is to demonstrate that FIPI does capture the correct deformation of the drop under different effective surface tension of the fluid-particle composite interface. More simulation results on the pendant drop simulation are included in Chapter 3.

The simulation is done in a rectangular parallelepiped of $[2\pi, 2\pi, 3\pi]$, discretised into $64 \times 64 \times 96$ nodes. Periodic boundary conditions are enforced in the three orthogonal directions. A spherical drop is initially positioned at the centre of domain. The drop is held at the top by a ring of stationary solid particles positioned at $0.95R$ above the centre of the drop with R as the initial radius of the drop. The Bond number calculated by using the surface tension of the bare fluid interface $Bo = \frac{\Delta\rho g R^2}{\gamma}$ is set to 0.1. At the beginning of the simulations, 5000 solid particles with radius $a/R = 0.02$ are uniformly distributed across the surface of the drop. The interactions between particles are set to follow the linear spring model in

Equation (2.14), with $r_c = 5a$. By adjusting the spring stiffness k_c, the particles monolayer can induce different surface pressures.

Once the simulation starts, the spherical drop starts to deform under the effect of gravity before eventually comes to a steady state when gravity and the effective surface tension balance each other. The effective surface tension of the drop at steady state can be calculated by two methods:

- The shape fitting technique of Fordham (See Ref.[165, 166])
- A direct calculation of Π_s using area averaging and $\gamma_{eff} = \gamma - \Pi_s$ (Equation (2.61))

where Π_s is given by Equation (2.60), and the effective surface tension γ_{eff} accounts for the presence of the particle. The results for the comparison between the two methods are reported in Table (2-A).

Pendant Drop Simulation Results			
Case Number	Surface Tension measured by Shape Fitting	Surface Tension measured by Irving-Kirkwood Formula	Relative Error %
1	0.0696	0.07	0.6%
2	0.0543	0.056	3%
3	0.0424	0.0419	1.2%
4	0.0277	0.028	1.0%
5	0.0175	0.0164	6.7%

Table 2-A: Surface tension measured by Fordham's shape-fitting method in comparison with the values calculated by area averaging and using Irving-Kirkwood's formula (Equation (2.60)).

The case 1 is the simulation done without the particles therefore $\Pi_s = 0$. The shape of the pendant drops at steady state is shown for case 1 and 5 in Figure 2.18. It is evident that the shape of the drop is more stretched in case 5, due to the reduction of surface tension caused by the monolayer covering the fluid interface. The relative error between the two methods is small, well within 5% on average. Fordham's technique is based on mapping the shape of the drop calculated through a solution to the non-linear Young-Laplace equation to a surface tension value. The good comparison between Fordham's method and the direct calculation of surface pressure with FIPI indicates that FIPI captures the correct drop shape expected from the solution of the Young-Laplace equation of capillarity (also in the presence of the particles).

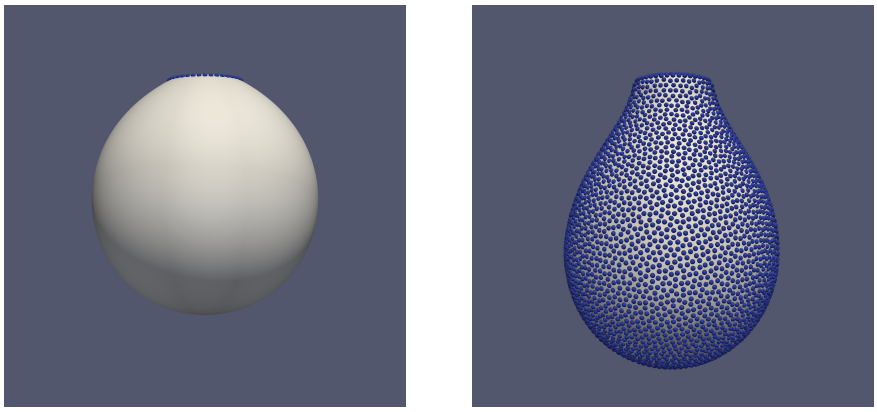

(a) Case 1 (b) Case 5

Figure 2.18: The shape of the pendant drop at steady state. (a) Case 1 (b) Case 5.

2.3.6 Simulation of Arrest of Liquid-Liquid Demixing by Absorbed Particles on Fluid Interface

For an immiscible binary fluid that is initially homogeneously mixed, the mixture will spontaneously undergoes phase separation [136]. The presence of solid parti-

cles absorbed on fluid interface can effectively slow down or even stop the phase separation process [23, 122]. Here some simulations are shown to qualitatively demonstrate that FIPI can capture this physical phenomenon.

The simulation is set up as follows: within a cubic computational domain of size $[2\pi, 2\pi, 2\pi]$, the phase field variable ϕ is initialised using a random uniform distribution of values between -0.1 and 0.1 (this distribution models a homogeneously mixed binary fluid). Isocontours of $\phi = 0$ at the beginning of the simulations are shown in Figure 2.20(a). Three different cases of simulations have been performed. The parameters are listed in Table (2-B).

Case	Condition
1	FIPI-Interface
2	FIPI-Interface + FIPI-Fluid
3	Full FIPI

Table 2-B: Three different simulations for phase separation process. Case 1 is the simulation of the Equation (2.1) without the convection term. Case 2 is the simulation done with the complete Equation (2.1) and the Stokes equation (Equation (2.16)). Case 3 is the simulation with all FIPI components (Including the dynamics of a group of particles).

The non-dimensional mobility parameter s is set to 0.2 for all three cases. The Cahn number $Cn = \epsilon/L$ is set to 0.017, with L being the length of the cubic computational domain. The total simulation time is non-dimensionalised by the characteristic time $t_c = L\mu/\gamma$, where μ is the viscosity. The non-dimensional simulation length is set to 114. For case 3, a total number of 7000 particles with radius of $a/L = 0.016$ are randomly distributed with uniform probability within the computational domain at the beginning. The corresponding volume fraction of the solid particles is 12.2%.

The total free energy of the phase field of the entire volume, being a characteristic indicator of the phase separation process, is calculated as

$$F_{tot} = \int_{\Omega} F, \tag{2.70}$$

where the free energy density F is defined in Equation (2.3). The time evolution of the total free energy F_{tot} for the simulations of all three cases is shown in Figure 2.19.

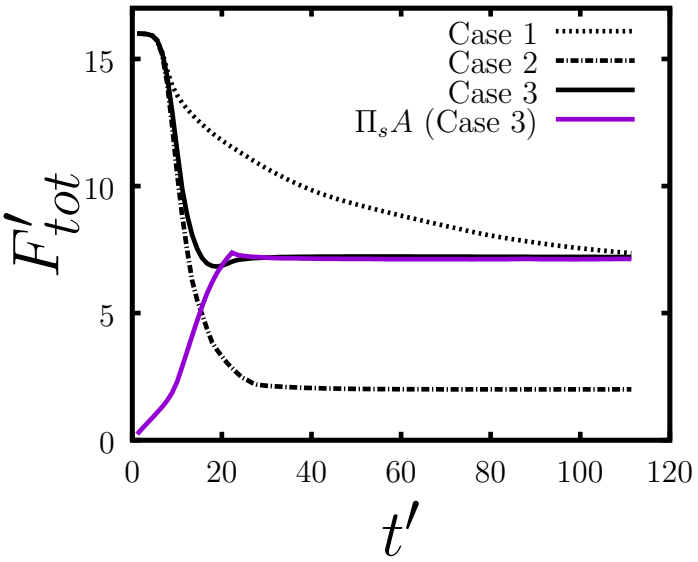

Figure 2.19: The free energy of the entire domain versus time during the phase separation process for three simulation cases. The total free energy F_{tot} is normalised as $F'_{tot} = F_{tot}/\gamma L^2$. The time is normalised by the capillary time scale $t_c = \frac{L\mu}{\gamma}$ as $t' = t/t_c$.

At the initial condition, the binary fluid can be considered as homogeneously mixed (Figure 2.20(a)). After the simulations started, the initial separation process was mostly driven by the diffusion term in the Cahn-Hilliard equation for all three cases.

For case 1, after the fluid interface was formed (ϕ approximately follows the

profile of $\tanh(x/\sqrt{2}\epsilon)$ across the fluid interface), the diffusion process began to slow down. By the end of the simulation (Figure 2.20(b)) the free energy still did not reach a steady state value. As the time scale of the simulations with only diffusion is significantly longer [136], the simulation in case 1 was made not to proceed further.

For case 2 that includes FIPI-Fluid, the flow induced by the surface tension force started to become dominant once the fluid interfaces were clearly formed. The surface tension flow is essentially a mean curvature flow that tries to minimise the interface area. Hence the surface tension flow introduced an additional driving force for the reduction of the total free energy. This is evidenced by a faster decline rate of the total free energy for $t' > 10$ in case 2 compared to case 1. At steady state, $F'_{tot} \approx 2$, corresponding to the formation of two planar fluid interfaces (Figure 2.20(c)).

However, in case 3 in which the solid particles are included, the particle monolayer formed at the fluid interface started to jam the fluid interface when the interface area was reduced below a critical value. The jammed particle monolayer effectively froze the phase separation process. The total free energy was kept constant at a value much larger than the steady state value in case 2 (as shown in Figure 2.19 for $t' > 20$). In experimental settings, the resulting meso-porous structure is called a "Bijel" [23]. The simulated structure is shown in Figure 2.20(d).

It is interesting to note that in case 3 the surface energy created by the particle monolayer $\Pi_s A$ (purple line in Figure 2.19) exactly matches the total free energy of the phase field at steady state. Since the free energy is concentrated at the fluid interface and $F_{tot} = \gamma A$, this implies $\Pi_s = \gamma$. The surface tension is balanced by the surface pressure of the particle monolayer. As a consequence the capillary

force driving fluid-fluid demixing is reduced to negligible values.

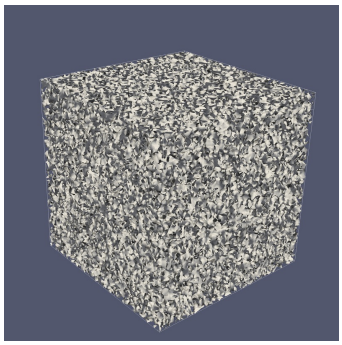

(a) Initial fluid interface contour ($\phi = 0$).

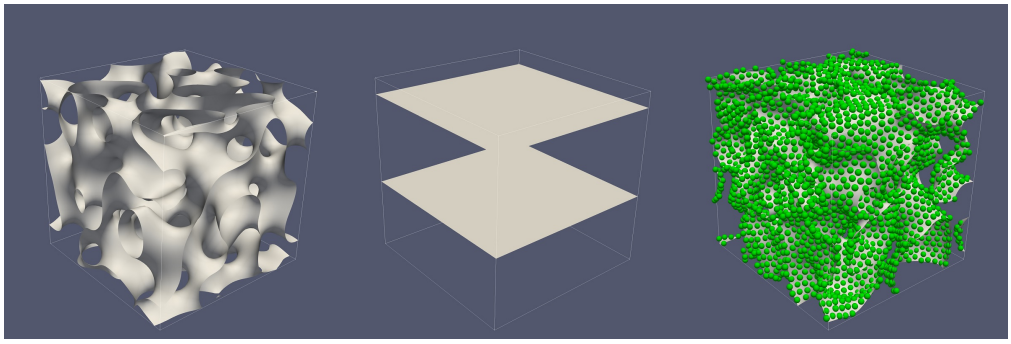

(b) Case 1 (c) Case 2 (d) Case 3

Figure 2.20: The fluid interface contours at (a) the start and (b-d) the end of simulation.

2.4 Performance Considerations

To test the efficiency of the FIPI, the simulation in section 2.4.6 is repeated with a smaller particle radius $\frac{a}{L} = 0.004$ to accommodate more particles inside the computational domain. The simulation is performed for 1000 time steps corresponding to a physical time of $11.1\frac{L\mu}{\gamma}$. The wall-clock time spent by each simulation is measured against the number N of particles in the simulation. The results are shown in Figure 2.21.

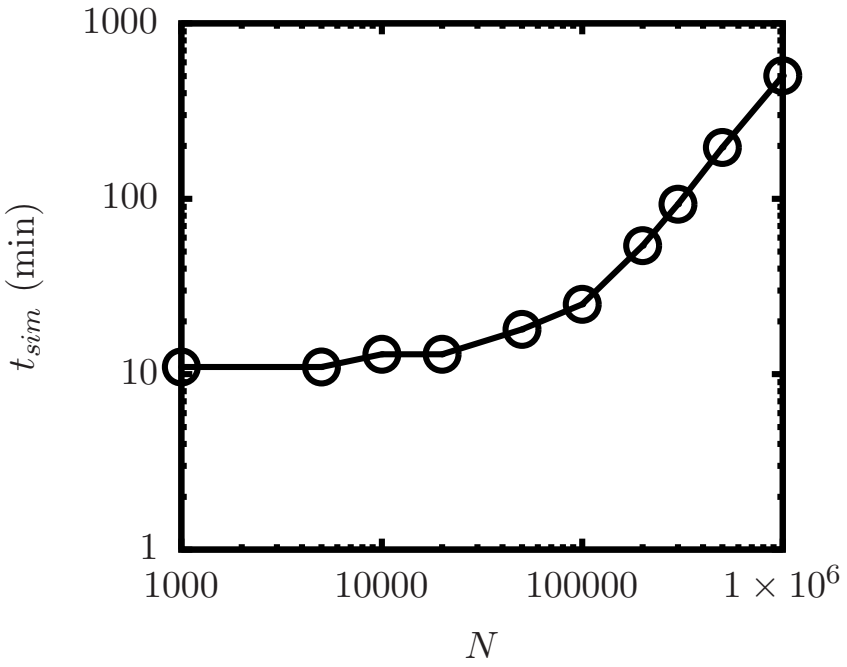

Figure 2.21: Simulation time (in minutes) versus number of particles present in the computational domain.

For simulations with $N < 10^6$, the order of magnitude of t_{sim} is approximately constant. This indicates that most of the computational cost is attributed to the solvers of FIPI-Fluid and FIPI-Interface when the solid particles are relatively sparse. When $N > 10^5$, the order of magnitude of t_{sim} increase dramatically . The slope of the $\log(t_{sim})$ versus $\log N$ remains approximately constant at 1.38 for $N > 10^5$. In the current version of FIPI, the scaling of computational cost with number of particles is thus only slightly super-linear. As far as particle-tracking code is concerned, this good performance is mostly due to the implementation of an efficient neighbour search algorithm.

Chapter 3

Numerical Experiments with FIPI: I-Investigation of Surface Stress Anisotropy in a Particle-Covered Pendant Drop

In this chapter, surface stresses are investigated in a simulation of a pendant drop in which the interface is covered by a monolayer of repulsive colloidal particles forming a curved 2D colloidal crystal. Colloidal crystals at fluid interfaces have been used as model systems to study topological defects on curved manifolds [45, 46]. Colloidal crystals of varying degree of micro structural order often form in systems when the particles are charged [167]. In the current simulations, the particle-particle interaction force model is designed to mimic a screened repulsive Coulomb interaction between charged particles. From a fundamental perspective, considering purely repulsive interactions lays the basis for understanding the interplay

between repulsive and attractive forces.

The main aim of this investigation is to elucidate the spatial distribution and anisotropy of the surface stresses. Among other effects, the presence of anisotropic surface stresses is associated with the formation of wrinkles and other buckling phenomena in drops or bubbles bearing structured interfaces [40, 60, 168–171]. Non-uniform stresses have been shown to play a fundamental role in the mechanics of jammed fluid interfaces [57]. In contrast to previous pendant drop simulations, in which the complex interface is treated as a continuum [68], the particles are treated as discrete objects. Surface stresses due to particles have been investigated for flat [63, 63, 172, 173] or spherical interfaces [146]. The current work aims to highlight challenges in measuring surface stresses from interfaces presenting geometrically complex and potentially time-dependent morphologies.

To calculate surface stresses resulting from particles absorbed at the surface of the drop, two main approaches can be adopted. For static problems, the conventional approach is to fit the shape of the composite interface to a numerical solution of the non-linear Young-Laplace equation. Since in general the surface stresses are non-uniform and locally anisotropic, this approach provides a "best-fit" to the properties of the entire drop surface. It is worthwhile to note that in Ref.[40], a shape-fitting procedure that enable to calculate anisotropic stresses has been recently proposed. A second approach is to calculate the local surface stress directly by local spatial averaging, using an extension of Irving-Kirkwood's expression (Eq.(2.59)). It is possible to utilise this approach even when the particle arrangement or the drop shape are time dependent. In the current investigation, both approaches will be adopted and the results are compared when possible.

In experiments the interfacial curvature is rarely uniform or isotropic, and this

affects the particle distribution in a non-trivial way. On a surface of non-uniform curvature the particles will redistribute on the surface, adopting after surface stress relaxation a concentration distribution consistent with the condition of zero tangential forces on the particles. In addition, while in the case of uniform interfacial curvature and homogeneous particle packing one can average over the entire surface, non-uniformity necessarily requires applying local averaging.

It is demonstrated through numerical experiments that the isotropic contribution to the stress calculated from the Irving-Kirkwood expression converges to the surface tension calculations based on fitting the shape of the interface to the Young-Laplace equation. In addition, the Irving-Kirkwood formula enables the direct calculation of the anisotropic component of the surface stress, which is related to the surface shear elasticity. The spatial distribution and the magnitude of the anisotropic surface stresses in static and transient simulations are investigated. As it was recently demonstrated with the use of principles of interfacial continuum mechanics, anisotropy and uniformity are intimately linked, as surfaces with non-uniform stress should also display non-isotropic stress, and vice versa [40].

3.1 Simulation Method

Simulations have been done for a pendant drop covered with a monolayer of identical spherical particles. As in classical pendant drop experiments, the drop is held at the top and deforms under gravity. The momentum equation, which is treated in the low-Reynods number limit, now includes a gravitational term $\rho\mathbf{g}$,

$$-\nabla p + \mu\nabla^2\mathbf{u} + \rho\mathbf{g} + \xi\nabla\phi + \sum_{i=1}^{N}\mathbf{F}_i\delta(\mathbf{x}-\mathbf{x}_i) = \mathbf{0} \tag{3.1}$$

Following the model of capillary force between particle and fluid interface $F_{pi}^{(i)}$ in equation (2.11), the physics of particle adsorption requires $f = O(1)$ [5, 128, 174, 175]. For static simulations $f = 1$ is used. When using $f = 1$ in transient simulations, under certain conditions (typically for large surface coverage) the particles are expelled from the interface in correspondence to the top edge of the drop. This phenomenon seems to be quite sensitive to the way the drop is pinned. To limit the complexity of the simulations, in transient simulations the particles are constrained to the surface of the drop by choosing $f = 10$.

The particle-particle interaction force $F_{pp}^{(ij)}$ on particle i due to particle j is assumed to be a screened Coulomb interaction force. The model of particle-particle interaction force F_{pp}^{ij} in equation (2.14) is adopted, where r_c now can represent a finite Debye length of the screened Coulomb interaction between two charged colloidal particles. Coulomb and dipole-dipole electrostatic interaction forces between colloids at fluid-fluid interface can be approximated by r^{-2} and a r^{-4} power laws, respectively [45, 176–178]. In addition to be relevant to experiments with strongly charged particles, the r^{-2} law makes particle-particle interaction effects more marked, and therefore was chosen for the current work. It is expected that the qualitative features of the results presented in the current investigations will not depend significantly on the value of the power-law exponent.

The governing equations are solved in a triply-periodic domain by a pseudo-spectral method. Spectral methods enables accurate evaluation of spatial derivatives owing to the Fourier series representation and a fast solution. To pin the drop at its top portion, a ring of stationary particles is used to exert forces in the upward direction, opposite to gravity. For these particles, the particle-interface capillary adhesion was tuned so that the particle ring could sustain the total weight of the drop.

3.2 Simulation Parameters and Procedure

The physical parameters related to the fluid and the bare interface are the gravity constant g, the density difference $\Delta\rho$ between the drop and the surrounding fluid, the surface tension of the bare interface γ, and the initial radius of the drop R. The parameters associated to the particles are the particle radius a, the number of particles N, the inter-particle force parameter F_0, and the cut-off length r_c. These parameters enable to build the following non-dimensional groups: the area fraction ϕ_s, the Bond number $Bo = \Delta\rho g R^2/\gamma$ of the drop without the particles, the non-dimensional interaction strength parameter $\mathcal{F} = F_0/(\gamma a^3)$, the interaction range parameter r_c/a, and the ratio of the particle size to the drop size a/R. For all current simulations, the ratio of the particle radius to the initial drop radius is fixed to $a/R = 0.02$.

The area fraction values reported in the current investigations are calculated as $\phi_s = N\pi a^2/A_0$, where $A_0 = 4\pi R^2$. Being based on the initial drop radius, the values of ϕ_s should be interpreted as nominal area fractions. By calculating the local area fraction at the drop apex by area averaging it is verified that the values of ϕ_s based on the initial drop area are very close numerically to those measured with the deformed drop.

At the start of each simulation, the particles are randomly arranged on the surface of the drop and the inter-particle force is switched off. After enabling the interparticle interactions, the monolayer quickly relaxes to adopt a particle distribution consistent with the instantaneous drop shape. The observed time scale over which the particles relaxed in the interface was found to be much smaller than the time scale of droplet deformation. The microstructure can therefore be assumed to change quasi-statically as the drop deforms. Unless otherwise specified,

the Bond number is set to $Bo = 0.223$.

3.3 Results

In the work of current chapter, an orthogonal coordinate system is adopted, where the subscript s and ϕ denotes the meridional and azimuthal coordinate respectively [40]. Lines at constant s are circles lying in planes perpendicular to the axis of the drop. The local stress due to the particles in the azimuthal and meridional directions corresponding to Equation (2.59) are given by

$$\sigma_{\phi\phi} = \frac{1}{2A_c} \sum_{\alpha} \sum_{\beta \neq \alpha} F_{\alpha\beta,\phi} \left(y^{\beta}_{s,\phi} - y^{\alpha}_{s,\phi} \right) \tag{3.2}$$

and

$$\sigma_{ss} = \frac{1}{2A_c} \sum_{\alpha} \sum_{\beta \neq \alpha} F_{\alpha\beta,s} \left(y^{\beta}_{s,s} - y^{\alpha}_{s,s} \right), \tag{3.3}$$

respectively.

In the current simulations, the surface stress tensor is diagonal in the local orthogonal coordinate system. In other words, principle directions of surface stress are azimuthal and meridional directions. In the local basis adopted here, $\sigma_{\phi\phi}$ and σ_{ss} are thus the only non-zero elements of the 2D surface stress tensor. The surface pressure satisfies $\Pi_s = -(\sigma_{\phi\phi} + \sigma_{ss})/2$. The deviatoric components of the surface stress in the azimuthal and meridian directions are given by $\sigma^D_{\phi\phi} = (\sigma_{\phi\phi} - \sigma_{ss})/2$ and $\sigma^D_{ss} = -\sigma^D_{\phi\phi}$, respectively.

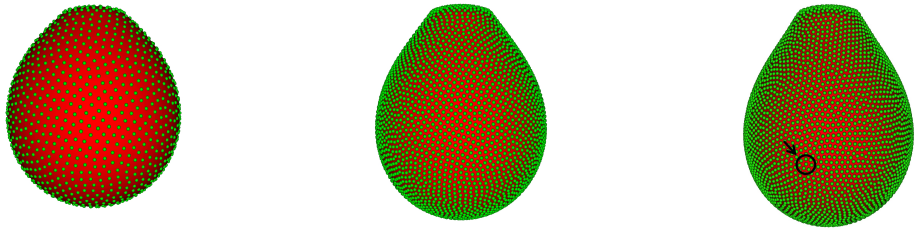

(a) $\phi_s = 0.15$ (b) $\phi_s = 0.4$ (c) $\phi_s = 0.45$

Figure 3.1: Steady-state drop shapes for different values of the area fraction ϕ_s and fixed $\mathcal{F} = 0.707$ and $r_c/a = 15.6$.

Simulated equilibrium drop shapes for different values of the area fraction up to $\phi_s = 0.45$ are shown in Figure 3.1. As the number of particles increases (for a fixed particle size), the drop assumes a more elongated shape, suggesting a reduction in the effective surface tension of the composite interface. For the values of area fraction shown, the particles are seen to be arranged in a dominant hexagonal order, forming a 2D colloidal crystal. A disclination in the crystal structure in which one particle is surrounded by 7 particles is indicated by a circle in Figure 3.1(c). Topological defects such as disclination and dislocations are important features of hexagonal crystals on curved surfaces [45, 46, 179, 180].

3.3.1 Effective Surface Tension by Shape Fitting

Denoting by κ_ϕ and κ_s the local curvatures of the interface along the azimuthal and meridian directions, respectively, the normal stress balance for the composite interface (treated as a two-dimensional continuum) reads

$$\gamma_s \kappa_s + \gamma_\phi \kappa_\phi = p_s. \tag{3.4}$$

Here γ_ϕ and γ_s are the interfacial tensions in the azimuthal and meridian directions, respectively, and p_s is the pressure difference between the inside and the outside of the drop. When the tension is isotropic, $\overline{\gamma} = \gamma_\phi = \gamma_s$ and Equation (3.4) reduces to the standard form of the Young-Laplace equation:

$$\overline{\gamma}(\kappa_s + \kappa_\phi) = p_s. \tag{3.5}$$

Since the change in p_s along the composite interface is due to gravity, we have

$$p_s = p_0 - \Delta\rho g z, \tag{3.6}$$

where p_0 is the pressure difference across the interface at the drop apex. The curvatures in the meridional and azimuthal directions can be expressed as

$$\kappa_s = \frac{d\theta}{ds} \text{ and } \kappa_\phi = \frac{\sin\theta}{r}, \tag{3.7}$$

where $\theta = \frac{dz}{dr}$ is the slope angle and r is the radial distance of from the symmetry axis. Combining equation (3.5)(3.6)(3.7) gives

$$\frac{d\theta}{ds} = -\frac{\sin\theta}{r} + \frac{p_0}{\overline{\gamma}} - \frac{\Delta\rho g z}{\overline{\gamma}}. \tag{3.8}$$

This equation, together with $dr = \cos\theta ds$ and $dz = \sin\theta ds$, constitute a closed non-linear system of equations. This system of equations can be solved numerically [165]. The numerical solution for the drop shape is at the basis of standard pendant drop measurements [181, 182].

Fordham [166] showed that when $\overline{\gamma}$ is constant, only two geometric parameters are needed to calculate the surface tension: the maximum diameter of the drop,

D_e, and the diameter of the drop at a distance D_e from the apex, D_s. From these two values, the surface tension can be calculated as

$$\overline{\gamma} = \frac{g\Delta\rho D_e^2}{H}, \tag{3.9}$$

where H is a unique function of the ratio D_s/D_e. In [166], accurate values for H calculated by solving Equation (3.5) numerically are tabulated.

The Fordham's method is applied to the current simulation data. To validate the approach, the surface tension of the drop without the particles is calculated and compared to the surface tension prescribed as input parameter to the phase-field method. The surface tension measured with Fordham's method were found to be 0.6% from the input value, as it is demonstrated in validation test 5 in chapter 2. Unlike experiments, simulations are subject to very limited noise in the data, so such good accuracy is not unexpected. In the following the Fordham's method is often referred as "shape-fitting method", although what is actually fitted is the drop curvature at two selected points, not the overall drop shape.

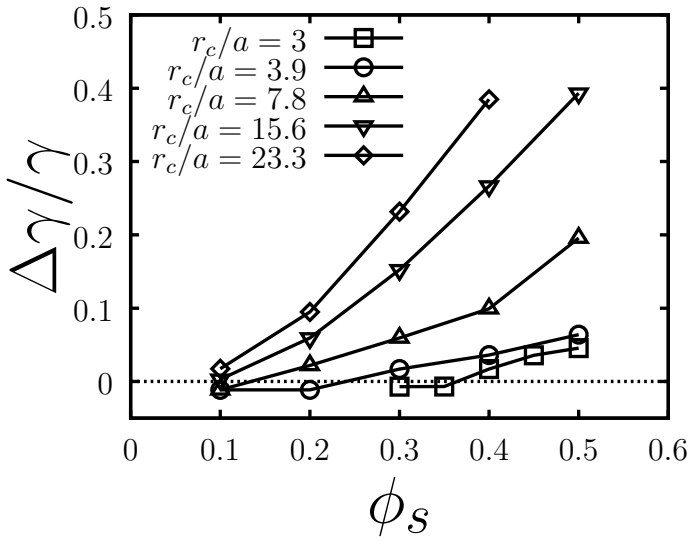

Figure 3.2: Surface tension reduction, $\Delta\gamma = \gamma - \overline{\gamma}$, vs. area fraction for different values of r_c/a; r_c is the cut-off range of the repulsive force and a is the particle radius.

Figure 3.2 shows the surface tension reduction $\Delta\gamma = \gamma - \overline{\gamma}$, calculated by using Fordham's method, for the particle-laden case. The surface tension was calculated at equilibrium, *i.e.* when the drop had reached a steady-state shape. The surface tension reduction is plotted as a function of the area fraction for $\mathcal{F} = 0.707$ and different values of r_c/a. The maximum possible area fraction explored with stable drops is $\phi_s = 0.5$ for $r_c/a < 23.2$ and $\phi_s = 0.4$ for $r_c/a = 23.2$. For each value of r_c/a, increasing the area fraction led to unstable drops, as discussed below.

As expected for purely repulsive inter-particle forces [14], the presence of the particles produce a reduction is surface tension ($\Delta\gamma > 0$). The surface tension reduction is seen to increase faster than linearly with ϕ_s. The tension on an element of composite interface along a given direction is given by the force per unit length along that direction. Part of this force is due to the bare interface. This component does not depend on the deformation. Part is due to the particles.

As ϕ_s increases the inter-particle force increase faster than linearly, and this gives a non-linear relation between $\Delta\gamma$ and ϕ_s.

The curves referring to relatively small values of r_c suggest that the surface tension reduction is very small for a non-zero value of ϕ_s. Because of the finite range of the interparticle force, athermal particles separated by a distance larger than r_c will not interact with each other, giving no effect of the particles at finite surface coverages. In the current study, when the inter particle separation is larger than r_c the surface tension reduction is not strictly zero, but is nevertheless negligibly small.

An estimate can be developed for the relation between cut-off length r_c and critical area fraction to obtain zero effect of the particles on the surface tension. For particles in hexagonal packing on a planar interface, the average interparticle distance is $\ell = \left(\frac{2\pi a^2}{\sqrt{3}\phi_s}\right)^{1/2}$. Setting $\ell = r_c$ the estimated value of the area fraction for which $\Delta\gamma = 0$ is $\phi_{s,min} = \frac{2\pi}{\sqrt{3}}(\frac{a}{r_c})^2$. This estimate gives $\phi_{s,min} \simeq 0.4$ for $r_c/a = 3$, in reasonable agreement with the values of Figure 3.2.

As the cut-off distance r_c approaches the particle diameter, the system approaches the hard disk limit in which the surface tension changes only when the particles are in physical contact. In this limit it is expected that $\Delta\gamma = 0$ for ϕ_s smaller than the value ≈ 0.92 which corresponds to maximum packing. A signature of this behaviour is the fact that the curves in Figure 3.2 become flatter as r_c/a decreases.

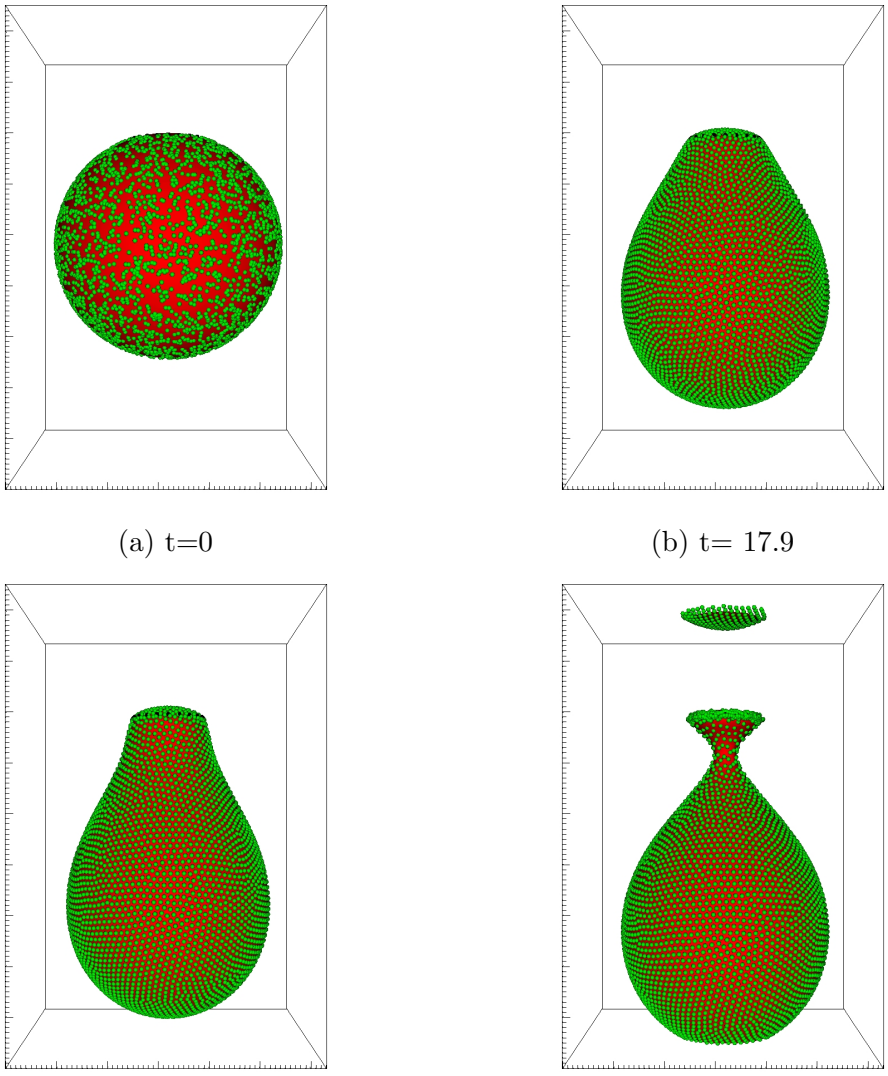

(a) t=0 (b) t= 17.9

(c) t=35.9 (d) t=52.7

Figure 3.3: Time evolution of the drop breakup process for $\phi_s = 0.5$ and $r_c/a = 23.2$. Time is expressed in units of $\sqrt{R/g}$.

If the surface tension reduction is larger than a threshold value, the drop becomes unstable and pinches off, as illustrated in Figure 3.3. This is due to the surface tension forces being unable to support the weight of the drop. Padday and Pitt [183] investigated the stability of axisymmetric menisci. Their results, applied to the current parameters, suggest that for the case of a pendant drop

of fixed volume hinged at a circular boundary, the critical Bond number separating stable and unstable regions is about $Bo = 0.28$. Noticing that $\Delta\gamma$ increases monotonically with ϕ_s, the results of Figure 3.2 for $r_c/a = 23.2$ indicate that for $\phi_s = 0.5$ the surface tension reduction should be larger than 0.4γ. A reduction in surface tension by more than 40% results in a Bond number larger than 0.37. This value is in the unstable region.

The effect of interfacial particles on fluid dynamic events occurring at pinch-off is an intriguing phenomenon that has received some attention only recently [184]. The current simulations refer to phenomena that occur well before pinch off.

3.3.2 Surface Stress by Local Area Averaging

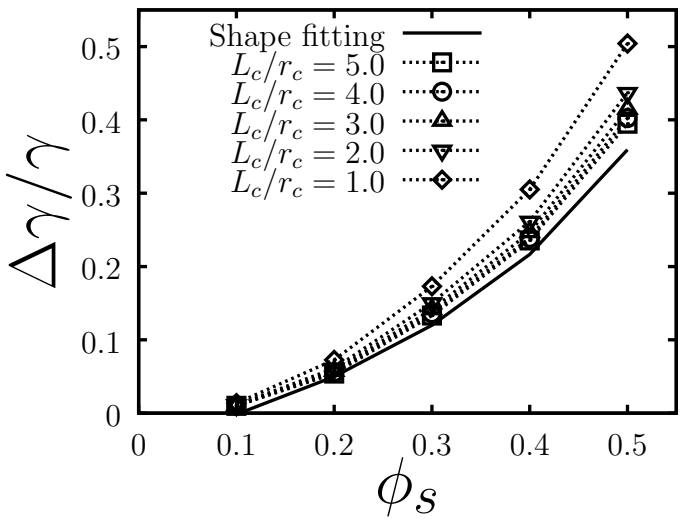

Figure 3.4: Surface pressure at the drop apex calculated by area averaging; L_c is the radius of the averaging control region. The interaction strength parameter is $\mathcal{F} = 1.414$, and $r_c/a = 7.8$. The continuous line corresponding to the value of $\Delta\gamma$ calculated by shape fitting, as in Figure 3.2.

A significant challenge in performing area averaging is choosing the size of the averaging control region. This size must be sufficiently large in comparison to the inter-particle distance and sufficiently small in comparison to the characteristic radius of curvature of the drop. In order not to introduce an artificial cut-off, the size of the control region must also be significantly larger than the interaction range r_c. Each choice for the size of the control region represents a compromise, and will introduce some error. This error is expected to decrease as the inter particle separation and the interaction range are reduced with respect to the drop size.

To illustrate how area-averaged results change as a function of the size of the averaging control region, Figure 3.4 shows the surface pressure at the drop apex for different values of L_c, where L_c is a parameter characterising the size of the control region. Area averaging is carried out by considering a sphere of radius L_c surrounding the apex; the intersection of such sphere with the drop shape defines a curved surface, having approximately the shape of a spherical cap. The area of this surface is used in the denominator of Equation (2.59). In Figure 3.4, the values of $\Delta\gamma$ given by the shape-fitting method are also shown for comparison (solid line).

For an interface having uniform and isotropic surface stress, it is expected that the values of Π_s converge to the values of $\Delta\gamma$. Figure 3.4 shows that as L_c increases the value of Π_s computed by area averaging approaches from above the value of $\Delta\gamma$ calculated with the shape-fitting method. For the parameters explored, a value of L_c larger than about $3r_c$ gives reasonably converged values (this result is in keeping with preliminary tests on a planar monolayer). The absolute deviation between Π_s and $\Delta\gamma$ appears to slightly increase with increasing area fraction. The relative deviation is however roughly constant. Given the incomplete scale separation in the current simulations, the agreement between the results of formula 2.60 and the

shape-fitting method is overall reasonably good. For $L_c/r_c = 5$, the relative error is less than 10%. Within a tolerable error, the shape fitting method and the direct calculation of the stress by the Irving-Kirkwood formula thus give approximately the same surface pressure value.

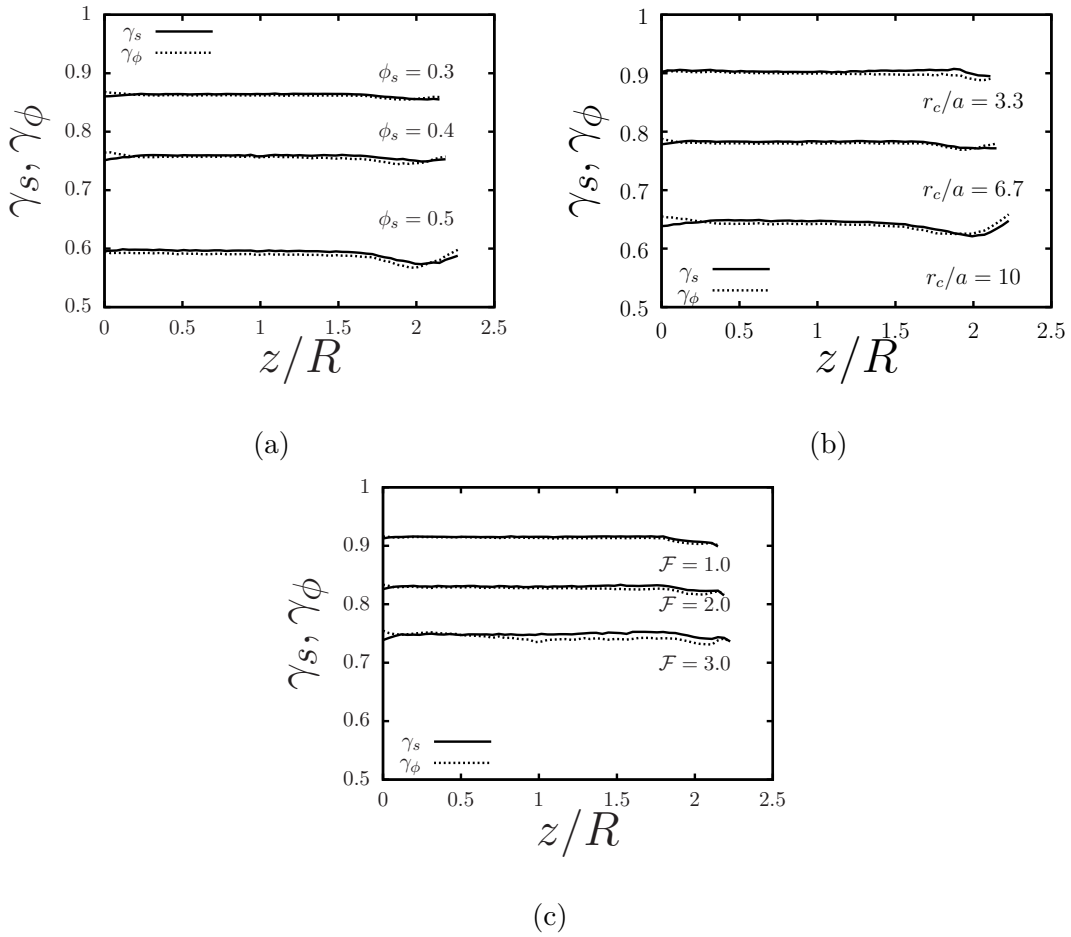

Figure 3.5: Azimuthal and meridian tensions for (a) different area fractions and fixed $\mathcal{F} = 1.414$ and $r_c/a = 7.8$; (b) different interaction ranges and fixed $\phi_s = 0.4$ and $\mathcal{F} = 1.5$; (c) different values of the interaction strength parameter $\mathcal{F}$ and fixed $\phi_s = 0.4$ and $r_c/a = 5$.

Figure 3.5 (a), (b) and (c) show the total azimuthal and meridian tensions, $\gamma_\phi = \gamma + \sigma_{\phi\phi}$ and $\gamma_s = \gamma + \sigma_{ss}$, as a function of the axial coordinate z for a selected range of simulation parameters, corresponding to different combinations of the parameters $\mathcal{F}$, r_c/a and ϕ_s. The magnitude of the deviatoric stress is given by the

spread between the continuous and dashed curves, while the average of these two curves gives the isotropic tension of the composite interface, $\gamma - \Pi_s$. For these results an isotropic filter is used including in the average particles within a sphere of radius $L_c = 4r_c$.

The azimuthal and meridian tensions are seen to be practically constant over the surface of the drop, and very close numerically to each other, suggesting negligible anisotropic effect and practically uniform surface stress. The small fluctuations visible for $z/R > 1.7$ are due to edge effects. The distance between the particles located in this region and the ring of particles pinning the drop is comparable to the filter radius, so the filter "picks up" unphysical force values. Increasing $\mathcal{F}$, ϕ_s, or the interaction range gives a larger surface pressure and therefore a smaller tension. This is not unexpected: increasing these parameters has the effect of increasing the repulsive force between the particles.

In the current simulations the surface stress anisotropy is negligible in the range of parameters in which the drop achieves static equilibrium. Several simulation parameters are explored for searching the range in which anisotropic effects are more marked. It is found that for variations of the simulation parameters in the direction that should give more pronounced anisotropic effects (larger inter particle forces, larger area fraction, and larger deformations), the drop quickly becomes unstable and pinches off.

From a qualitative point of view, this behaviour can be understood from the following argument. In the absence of attractive interactions between the particles, the azimuthal and meridian tensions decrease with increased deformations. To achieve a degree of anisotropy sufficiently large to be measured, the inter-particle forces need to be relatively large and the interface sufficiently stretched in the

direction of gravity. An increase in interparticle forces leads to a surface tension reduction, bringing the system in the range of parameters in which the drop is unstable. Starting from a smaller Bond number, and thus from a smaller initial drop deformation, allows to be farther from the unstable region, but also reduces the anisotropic deformation of the microstructure.

Our results could suggest that in the absence of attractive interactions and for repulsive interactions having a range significantly large in comparison to the particle size, anisotropic stresses in stable pendant drops may be observed only in a very narrow range of parameters.

3.3.2.1 Transient simulations

In this section the emergence of anisotropic effects in transient simulations is illustrated and Bond number is set to $Bo = 0.334$. In these simulations, the surface stress will relax much faster than the drop deformation except near the instant when the drop breaks off.

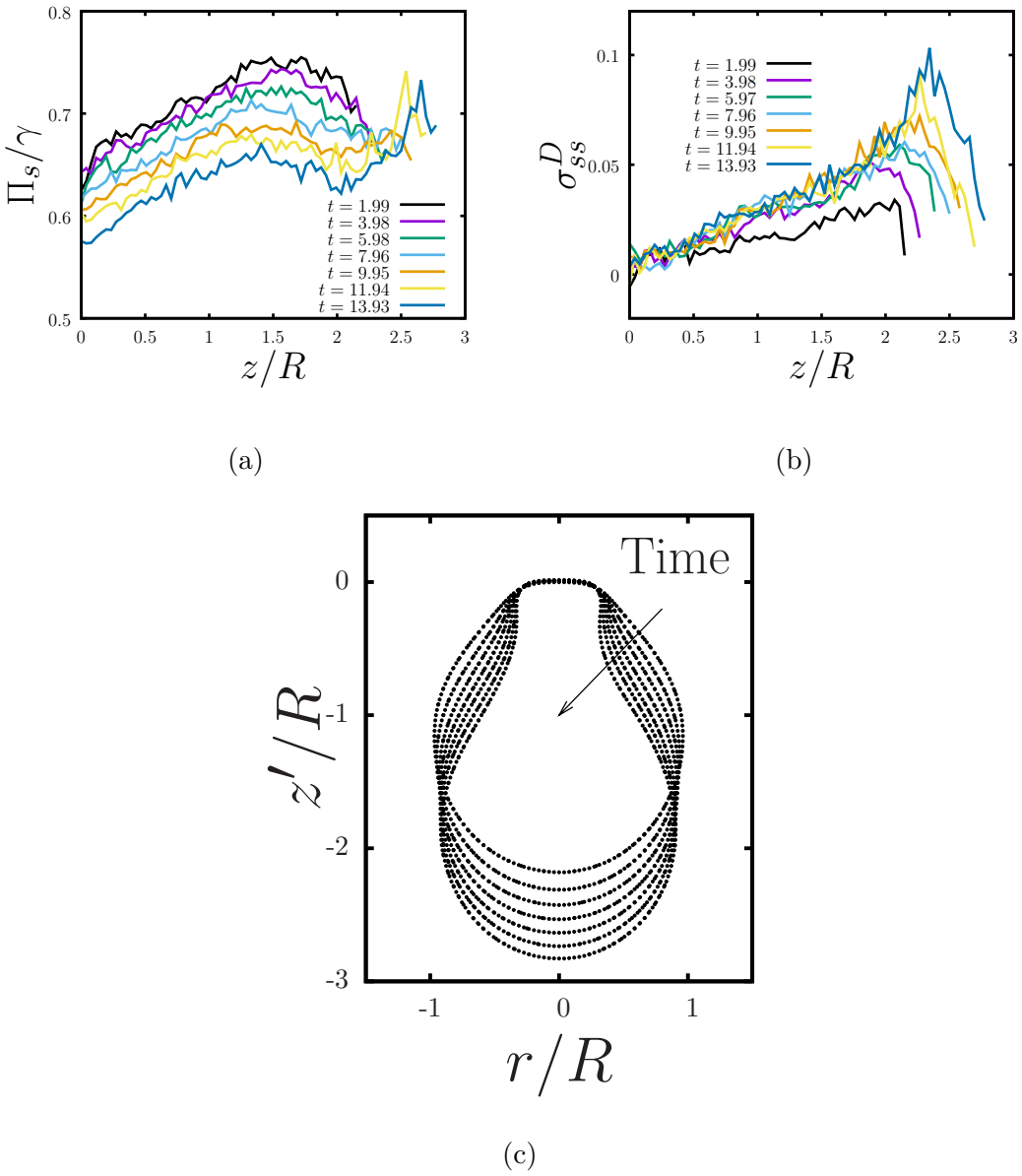

Figure 3.6: Time evolution of the surface pressure, (a), and deviatoric meridian surface stress, (b), for $\phi_s = 0.7$, $r_c/a = 2.5$ and $\mathcal{F} = 6.0$. The origin of the axial coordinate z is the drop apex. Contours of the drop shapes corresponding to the seven time instants of figures (a) and (b) are shown in figure (c). In this last figure z' is an axial coordinate with origin at the top edge of the drop.

Figs.3.6 (a) and (b) show the time evolution of the surface pressure Π_s and the meridian component of the deviatoric surface stress σ^D_{ss}, respectively, for a relatively short-ranged interaction, $r_c = 2.5a$. The area fraction and interaction

strength parameters are $\phi_s = 0.7$ and $\mathcal{F} = 6.0$, respectively. Contours of the corresponding drop shapes, shown in Figure 3.6(c), illustrate how the drop deforms in time.

Owing to the drop deformation and corresponding dilatation of the interface, the surface pressure slowly decreases in time. In the region $z/R < 2.0$, and sufficiently above the drop apex, σ_{ss}^D increases for $t < 4.0$ and then remains approximately constant. This observation is consistent with the change in shape of the drop suggested by the contour plots of Figure 3.6(c): after an initial transient the bottom part of the pendant drop reaches an almost stationary shape that translates downward as a neck gradually forms in the region adjacent to the top edge of the drop.

The deviatoric stress is zero at the apex and increases with z. This suggests that the monolayer in the bottom part of the drop expands approximately isotropically with time, while the drop side deforms in an anisotropic manner.

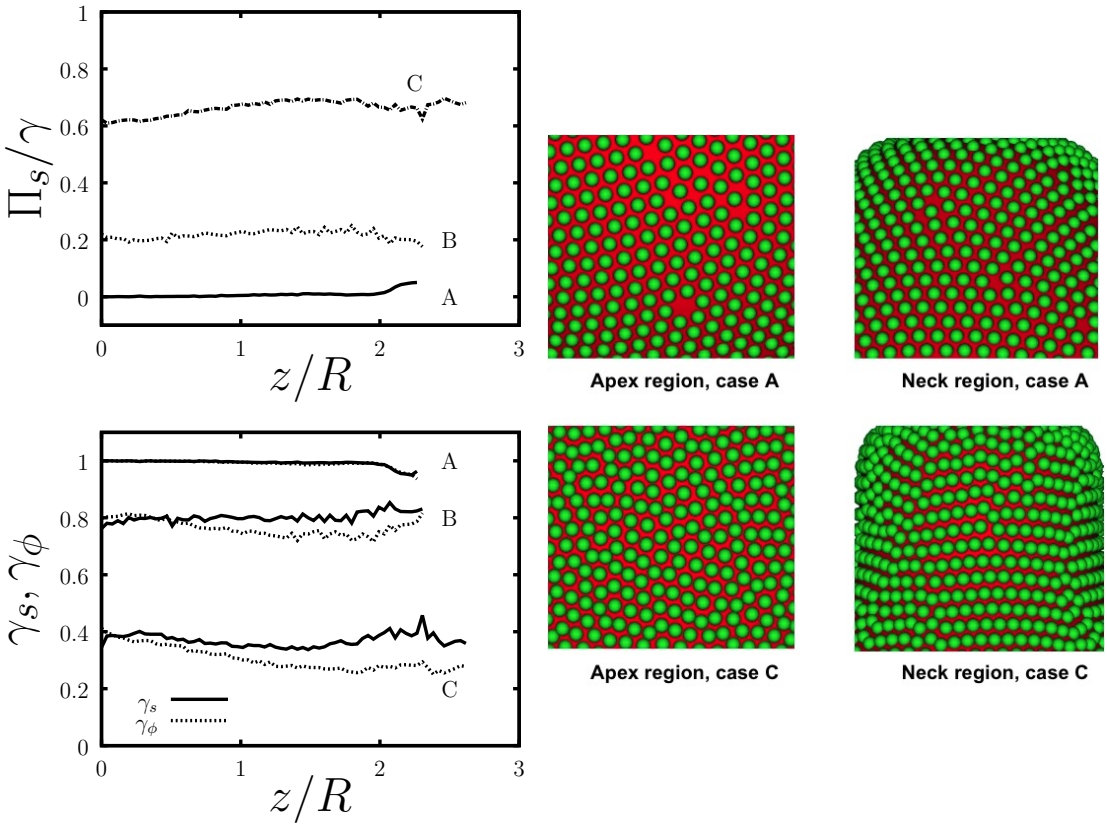

Figure 3.7: Transient simulations. Top-left: surface pressure calculated by area averaging as a function of the axial coordinate for cases "A", $\phi_s = 0.5$, "B", $\phi_s = 0.55$, and "C", $\phi_s = 0.7$. The time instant is $t = 9.95\sqrt{R/g}$. Bottom-left: meridian(solid lines) and azimuthal (dashed lines) components of the corresponding surface stress for cases "A", "B", and "C". Right: snapshots of the monolayer microstructure corresponding to the drop apex and neck regions for cases (A) and (C).

Figure 3.7, top-left panel, shows the surface pressure corresponding to a fixed time, $t = 9.95\sqrt{R/g}$, for three selected cases, labelled "A"," B" and "C". The corresponding total tensions in the azimuthal and meridian directions are shown in Figure 3.7, bottom-left panel. The three cases "A"," B" and "C" correspond to $\phi_s = 0.5, 0.55$ and 0.7, respectively. The interaction range and interaction strength parameters are as in Figure 3.6.

Case "A" illustrates a situation in which the surface stress is approximately

isotropic. Effects of anisotropy are significant in cases "B" and "C". For a fixed time, therefore, the degree of stress anisotropy increases with increasing surface coverage. The azimuthal component of the surface stress is smaller than the meridian component for any value of z. Thus it is expected that the microstructure is more stretched in the meridian direction than in the azimuthal direction. The degree of anisotropy, negligible in the near-apex region, becomes more marked as z increases (because of the axial symmetry, the surface stress must be strictly isotropic at the drop apex). For z slightly larger than $2R$, the absolute difference between γ_ϕ and γ_s appears to decrease slightly. However, it is likely that the values in this region are contaminated by edge effects due to the averaging region overlapping partially with the top edge of the drop.

Snapshots of the local microstructure of the monolayer corresponding to cases "A", and"C" are shown in Figure 3.7, right panel. For each case, two snapshots are shown: one referring to the apex region and one roughly corresponding to the neck region (*i.e.* to the side region where the drop diameter decrease in time). In the region near the apex, the microstructure is seen to be approximately isotropic, while the neck of the drop is on average characterised by a smaller inter-particle distance in the horizontal direction (the azimuthal direction) than in the vertical direction. The smaller inter-particle distance in the azimuthal direction gives rise to a larger repulsive force in this direction. As a consequence, γ_ϕ is smaller than γ_s.

Some of the qualitative features of the curves described in cases "B" and "C" are similar to those discussed in a recent work by Danov *et al.* [40] where experiments with buoyant bubbles featuring anisotropic structured interfaces are shown. Danov *et al.* measured γ_s and γ_ϕ for an interface in contact with a solution of HFBII, a small compact protein molecule; upon adsorption to fluid interfaces, HFBII

produces rigid layers displaying a measurable surface shear elasticity. Qualitative agreement to an extent can be found by comparing Figure 3.7 with Figure 7 in Ref.[40]. Danov*et al.* found that γ_s was larger than γ_ϕ for any given value of z, and that the magnitude of the deviatoric stress increased with z for locations not too close to the lower boundary of the bubble.

A possible difference between the current investigation and the case examined by Danov and collaborators is that in the current work the "bonds" between the particles become weaker as they are stretched (purely repulsive interaction), while in that experimental case some form of short-ranged cohesion between the protein molecules is expected. The competing effect of repulsion and attraction in determining the surface stress in colloidal monolayers embedded in geometrically complex fluid interfaces is an open research question.

3.4 Conclusions

Simulations are performed for a pendant drop presenting an interface covered with repulsive spherical particles. The distribution of the surface stress is analysed and how the components of this tensor change as a function of selected governing parameters is examined. The main parameters explored in the current investigations are the area fraction, the inter-particle interaction strength parameter, and the interaction range. The results for both static and dynamic drop shapes are presented.

For the range of simulated parameters for which the drop had a stable shape, the surface stress was found to be practically isotropic. Anisotropic effects were measurable only in transient simulations, and at relatively high values of the area

fraction. In transient simulations, anisotropic effects were more marked along the sides of the drop, corresponding approximately to the neck region where eventually the drop pinches off. In the case of highly deformed drops, visualisations of the microstructure of the monolayer highlighted marked deviations from an hexagonal arrangement.

It is not excluded that anisotropic effects can be measured on a static drop in a different range of parameters which is not able to be explored for now. The current method could be used to investigate the combined effect of short-range repulsion and long-range attraction. The presence of long-ranged attraction should stabilise the drop against pinch-off for strongly deformed drops.

Chapter 4

Numerical Experiments with FIPI: II-Investigation of the Transition Between Shell Buckling and Particle Desorption in a Particle-Covered Drop

From previous investigations of particle-covered pendant drops, it is evident that repulsive particles have the capability to reduce the surface tension of a fluid interface by creating finite surface pressure. The fluid interface laden with repulsive particles is subject to compression from the particle monolayer. To explore the limit of the compression, simulations of a spherical drop covered with particles having increasing strength of repulsive forces are carried out. The results of the simulations are expected to reveal the details of drop buckling and particle des-

orption.

In this chapter, the transition from buckling to desorption is investigated by carrying out simulations of compressing a spherical drop covered with a monolayer of monodispersed spherical particles. In these simulations, the strength of interparticle repulsive force is modulated in time to determine the compressive surface stress. The investigation follows the time-dependent morphology of the fluid interface and of the particle monolayer, by changing the following non-dimensional parameters: the size ratio between the particle and the drop a/R, the non-dimensional parameter f quantifying the strength of adhesion of the particles to the fluid interface and the ratio between the surface pressure Π_s and the bare surface tension γ. The results of the simulations suggest that desorption can be a result of a small scale monolayer shape instability which may not be easily observed in experiments, pointing to the importance of microscopic rearrangement of particles on the macroscopic dynamics. The result reported here is the first numerical analysis of the transition from buckling to desorption in the context of particle-covered interfaces.

Because the droplet deformation is quasi-static in the current simulations, the results presented in this chapter are independent of whether the fluid inside the particle-covered interface is a gas or a liquid. The current results are thus equally applicable to particle-covered droplets and particle-covered bubbles.

4.1 Simulation Procedure

The simulation domain is a cubic box of side $L = 3\pi$. Periodic boundary conditions are enforced along the three orthogonal directions. The governing equations

are solved with a standard Fourier-spectral method, eliminating the pressure p from the momentum equation by using the incompressibility condition [185]. The domain is discretised using 80 nodes in each orthogonal direction. The fluids inside and outside of the droplet have the same dynamic viscosity μ. At the start of simulations a spherical droplet with radius $R = 0.8\pi$ is placed at the centre of the domain. The particles are initially distributed uniformly on the surface of the droplet, by applying a uniform probability distribution to a spherical coordinate system [186]. The initial particle surface fraction $\phi_s = \frac{N}{4}\frac{a^2}{R^2}$ is equal to 0.5 in all the simulations.

In certain simulations presented in the current study, the parameter f from Equation (2.11) is set to be greater than 2.0 to make sure that the particles do not desorb and to investigate the limit in which the displacement of each particle from the fluid interface is negligible.

For all simulations presented in this chapter, the parameter S from Equation (2.43) governing the strength of diffusion in Cahn-Hilliard equation is set to 0.5, unless specified otherwise. This value has been chosen based on numerical tests with particle-covered drops subject to compressive surface stresses: in these tests for S in the neighborhood of 0.5 the fluid interface thickness was observed to be roughly constant in time and to have approximately the hyperbolic tangent profile expected near equilibrium. Following other authors [137, 150] the Cahn number is set to $Cn = 0.013$. The ratio dx/ϵ of the mesh size to the interface thickness was $2\sqrt{2}/3 \simeq 0.94$ in all simulations. This choice gives about 6 grid nodes across the region where ϕ varies from -0.963 and 0.963.

With the definition of surface pressure of particle monolayer from Equation

(2.60), the total packing energy E_p of a particle monolayer is calculated as

$$E_p = 2\Pi_s A, \tag{4.1}$$

where A is the total surface area of the drop. As we will see next, the time evolution of this quantity can give us insight about the buckling of the particle-covered drop.

During the shrinkage of a particle-laden drop or bubble, buckling or desorption occurs when the surface pressure reaches a threshold value as the surface area decreases [55, 65, 187]. Simulating an increase in surface pressure by reducing the drop volume by removing mass from the inside of the drop is possible, and this possibility is explored in preliminary work. However, this approach has several disadvantages. First of all, when using a computational box of finite size the simulated flow velocity is inevitably affected by the conditions at the outer boundaries. With a cubic box and periodic boundary conditions, for example, the computed velocity field is not spherically symmetric and for an initially spherical drop this leads to a loss of spherical symmetry in the phase field distribution that is not due to a buckling instability. Secondly, identifying the rate of volume reduction for which the process is quasi-steady is challenging. A further disadvantage of increasing the surface pressure by reducing the drop volume is that it is difficult to compare different simulation results for different values of a/R. For example, when comparing two simulations for the same initial drop radius but different particle size, small particles will give buckling for a later time than larger particles so the droplet radius at the moment of buckling will be different in the two cases.

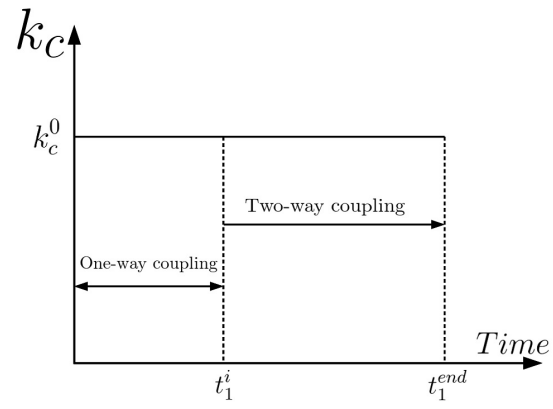

Mode 1

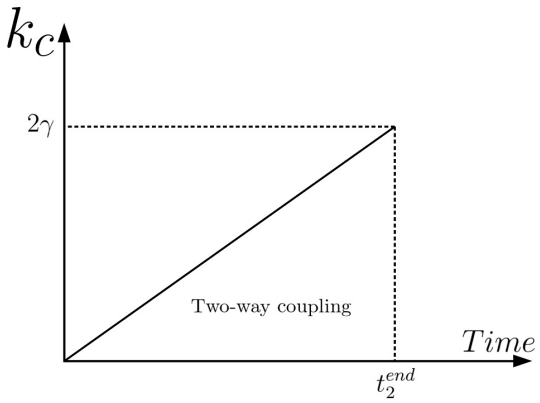

Mode 2

Figure 4.1: Modes of variation with time of the inter-particle force parameter k_c (Equation (2.14)). For the simulations investigating the time evolution for pure buckling mode 1 is used. For the simulations investigating the effect of f and a/R mode 2 is used.

Therefore the drop volume is kept constant, and the surface pressure is changed by varying k_c in equation (2.14). Two modes of variation of k_c with time are used (Figure 4.1):

- Mode 1: k_c is kept to a constant value k_c^0 throughout the simulation, where k_c^0 is chosen so that Π_s is larger than γ. To allow the particles to reorganise themselves on the fluid interface while maintaining a spherical drop, in the initial part of the simulation, i.e. for $t < t_1^i$, the particle forcing terms in Equation (2.16) are disabled. For $t_1^i < t < t_1^{end}$, where t_1^{end} is the simulation

end time, the particle forcing terms are enabled. In this two-way coupling stage the drop shape is affected by the particle distribution.

- Mode 2: The parameter k_c is slowly changed from 0 to 2γ, using for simplicity a linear variation. The slow variation of k_c enables the particles to reorganise themselves on the surface of the drop while the surface pressure builds up. In mode 2, the particle forcing terms in Equation (2.16) are enabled at all times. As far as buckling and desorption are concerned, increasing k_c in time is physically equivalent to shrinking the drop. The proof is shown in Appendix (A.3).

For the simulations investigating the time evolution for pure buckling (in the absence of desorption) the mode 1 is used. For these simulations the aim was to evaluate the effect of Π_s on the emergence of buckling. Thus, it was important to keep k_c, and thus Π_s, constant. The investigations on the effect of f and a/R were instead carried out by using mode 2.

4.2 Results

Time evolution of drop morphology for pure buckling (no desorption). Threshold surface pressure for buckling. Figure 4.2 shows the time evolution of the drop shape and of the particle distribution for an initial surface pressure $\Pi_s = 1.5\gamma$. As here the concern is only about the case in which desorption is absent, f is set to a large value, $f = 10$, to prevent any significant displacement of the particles from the fluid interface. At the beginning of the simulation the particles are randomly distributed on the surface of the drop (Figure 4.2A). Following an initial transient, in which the particles rearrange themselves on the surface of the

drop, a regular particle microstructure characterised by a dominant hexagonal arrangement emerges (Figure 4.2B) [45]. After some time the drop loses its spherical shape and buckles (Figures 4.2C and D).

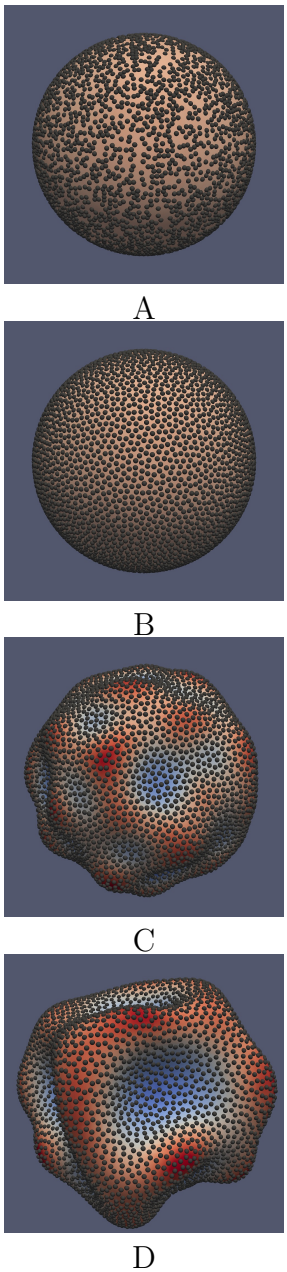

Figure 4.2: Time evolution of drop morphology and particle distribution for $f = 10$, $a/R = 0.02$ and $\Pi_s/\gamma = 1.5$. The labels A, B, C, and D correspond to different times (compare with Fig. 4.3).

To quantify the precise time instant at which the buckling instability develops, the total packing energy of the monolayer E_p (Equation (4.1)) and the corresponding drop surface area A are examined. The time evolution of E_p and A, and the time derivative of these quantities, are shown in Figures 4.3a and b. The labels A, B, C, and D indicate the time instants corresponding to the drop morphologies of Figure 4.2.

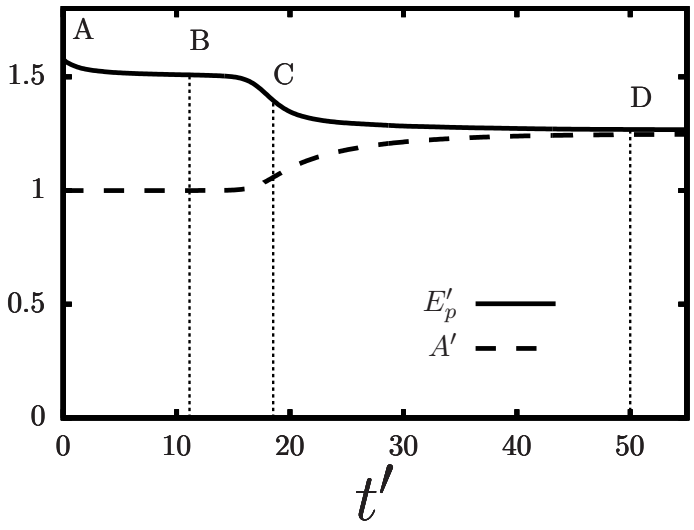

(a)

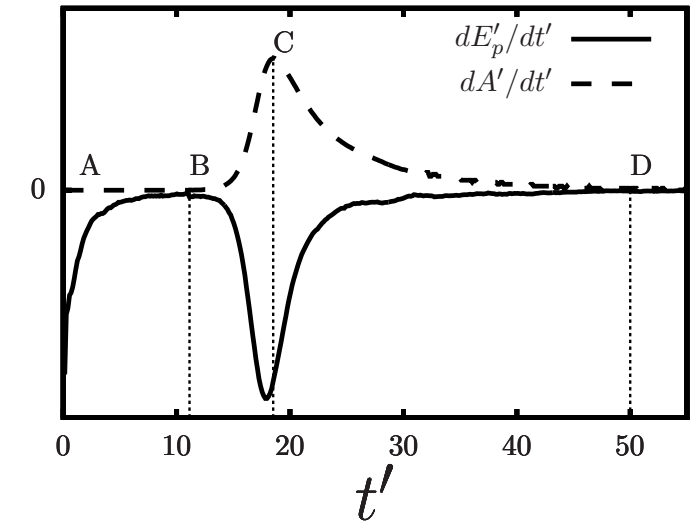

(b)

Figure 4.3: (a) Time history of the non-dimensional packing energy and surface area. (b) Time history of the non-dimensional rates of change of E_p and A with respect to time. Primes indicate dimensionless variables: $t' = t\gamma/(R\mu)$, $A' = A/A_0$ and $E'_p = E_p/(2A_0\gamma)$, where A_0 is the initial drop surface area.

Owing to the initial reorganisation of the particles, from time instant A to B the packing energy decreases, but the surface area remains unchanged. This is

expected, because between time instants A and B the one-way coupling regime ($t < t_1$ in Fig. 4.1), which gives a spherical drop shape, is used. At time instant B, the two-way coupling is switched on. A buckling process characterised by a simultaneous decrease in the packing energy and an increase in the surface area begins. The time derivative of the surface area dA'/dt' (primes denote non-dimensional quantities) reaches its maximum approximately in correspondence to the time instant C. The decrease in E_p and the increase in A are apparently synchronised, with the peak value of dA'/dt' just slightly lagging behind that of dE'_p/dt'. At the time instant D, both E'_p and A' reach a steady state. Interestingly, both ratios converge exactly to the same value. This is due to the fact that the steady state is achieved when $\Pi_s = \gamma$ (by definition $E'_p = \frac{\Pi_s}{\gamma}\frac{A}{A_0}$, hence $E'_p = A'$ as $\Pi_s \to \gamma$).

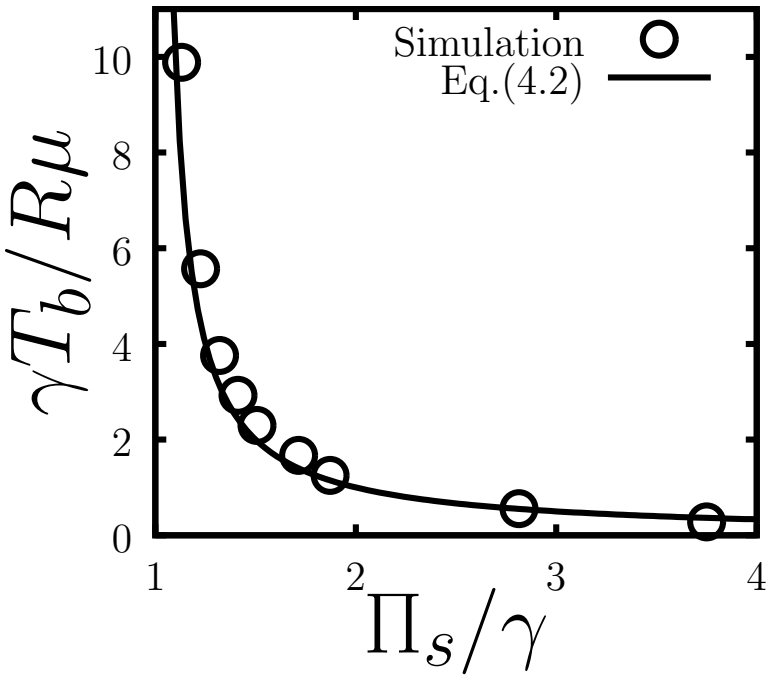

Figure 4.4: Normalised buckling time vs. normalised initial surface pressure for $f = 10.0$. The solid line is the proposed model equation (4.2). The numerical parameter s is here set to 0.01.

The buckling time T_b is defined as the time instant for which dA'/dt' has a peak and T_b is calculated for different values of Π_s/γ. The results are shown in Figure 4.4.

The first observation is that all the data points lie in the region $\Pi_s > \gamma$. For a continuous spherical elastic shell, the critical value of the total (including the contribution from the bare fluid interface) in-plane surface pressure for which buckling occurs is $\Pi_s - \gamma = 2\frac{\kappa}{hR}$ [188], where h is the shell thickness and κ is the bending rigidity of the shell ($\kappa \propto h^3$). In the current simulations κ is negligible, as bond-bending inter-particle interactions are not included. In addition, R is large in comparison to $h \sim a$. Therefore $2\frac{\kappa}{hR} \ll \gamma$. As a consequence, the expected necessary condition for buckling when the particles are strongly bound to the fluid interface ($f \gg 1$) becomes $\Pi_s = \gamma$. This result is confirmed by the simulation results of Figure 4.4.

The buckling time diverges as Π_s approaches γ from above, and decrease as Π_s increases when $\Pi_s > \gamma$. These features can be rationalised with a simple model. For $\Pi_s > \gamma$ the particle-covered interface is subject to a compressive surface stress of magnitude $\Pi_s - \gamma$. Equating the capillary force $\sim (\Pi_s - \gamma)R$ acting on the drop surface to the viscous force $\sim \mu U R$ resisting the motion of the interface, the characteristic normal interfacial velocity U during the evolution of the buckling instability is of $O((\Pi_s - \gamma)/\mu)$. Estimating T_b as the time taken by the interface to move a distance comparable to R yields

$$T_b \simeq \frac{R\mu}{\Pi_s - \gamma}. \tag{4.2}$$

As seen in figure 4.4, equation (4.4) describes the trend of the simulation data remarkably well with no fitting parameters.

Expression (4.2) shows that buckling can be an extremely slow process when Π_s is only slightly larger than γ. This observation is crucial for simulation studies. When simulating particle-laden drops or bubbles, one may have to carry out extremely long simulations to identify the onset of buckling with precision, as it is learned through direct experience. A drop, for example, may be declared not to buckle, when in fact the simulation has just not been run for a sufficiently long time. In this work, Equation (4.2) is used as an important practical guideline to choose the duration of the simulations.

It is found that T_b converges accurately to the value predicted by equation (4.2) as the numerical parameter $s \rightarrow$ to 0 while keeping the fluid interface thickness ϵ constant. This result, which is related to numerical aspects of the phase-field method, is presented in the Supporting Information.

Effect of non-dimensional adhesion strength. In this section the effect of the parameter f appearing in the particle-interface interaction model (2.11) is examined. This non-dimensional quantity is proportional to the work necessary to remove a particle from the fluid interface, normalised by the capillary energy scale γa^2. It can also be interpreted as the work of adhesion of the particle monolayer to the fluid interface normalised with the surface tension. Indeed, the energy associated to N particle-interface capillary bonds distributed over an area A is $E_{tot} = N\frac{1}{2}f\pi a^2\gamma$, thus the work of adhesion is $\Gamma = n_s\frac{1}{2}f\pi a^2\gamma$ where $n_s = N/A$ is the particle surface number density. Introducing the surface area fraction $\phi_s = n_s\pi a^2$ leads to $\frac{\Gamma}{\gamma} = \frac{1}{2}f\phi_s$. For identical spheres near maximum packing, the surface fraction is close to 1 ($\phi_s \simeq 0.92$[189]), thus $\frac{\Gamma}{\gamma} \simeq \frac{1}{2}f$.

The effect of changing f on the drop morphology is illustrated in Figure 4.5. The figure shows the shape of the drop and the corresponding particle distribution

for selected times. In this figure f is varied from 1 to 4, two limits that are representative of weak and strong adhesion.

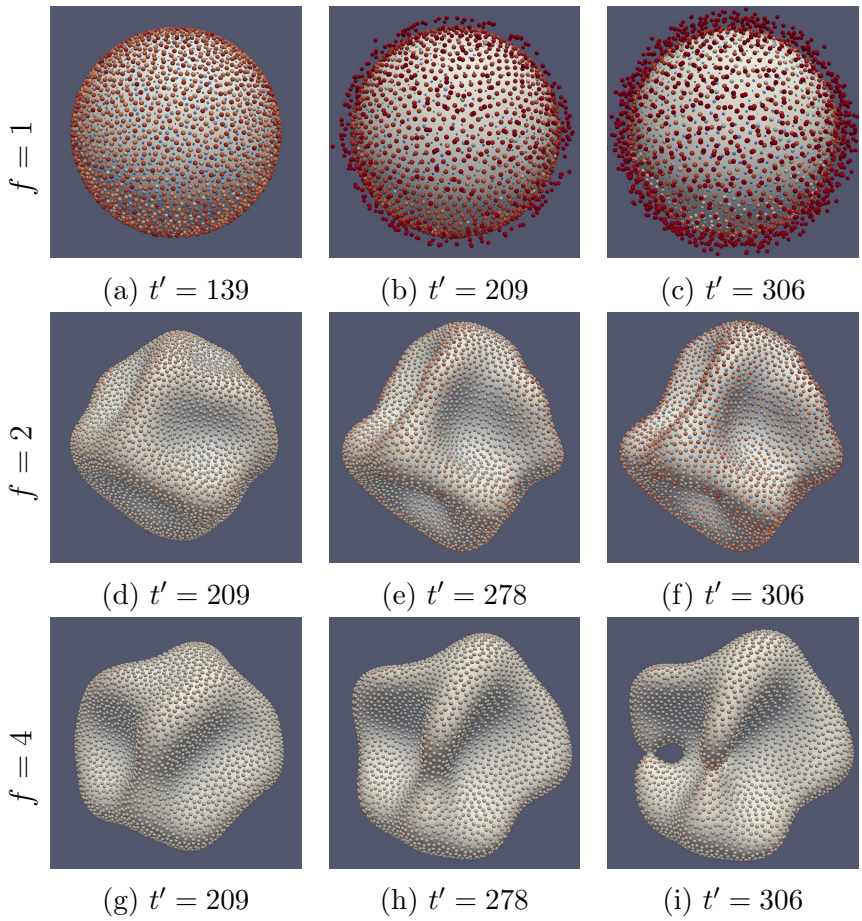

(a) $t' = 139$ (b) $t' = 209$ (c) $t' = 306$

(d) $t' = 209$ (e) $t' = 278$ (f) $t' = 306$

(g) $t' = 209$ (h) $t' = 278$ (i) $t' = 306$

Figure 4.5: Time evolution of the monolayer morphology for $a/R = 0.02$, $s = 0.5$ and different values of f. The particles are colored according to their signed distance from the fluid interface (red: outside of the drop; blue: inside of the drop; grey: embedded in the fluid interface).

For $f = 1.0$ the particles are seen to desorb collectively from the fluid interface for non-dimensional time $t' < 209$. Uniform desorption of nanoparticles upon pendant drop compression was reported in the experiment of Ref.[55]. In that experiment the desorbed particles formed a thin halo adjacent to the drop surface. The halo slowly diffused outwards owing to Brownian motion. The particles eventually were swept by gravity towards the drop's bottom apex. In the current

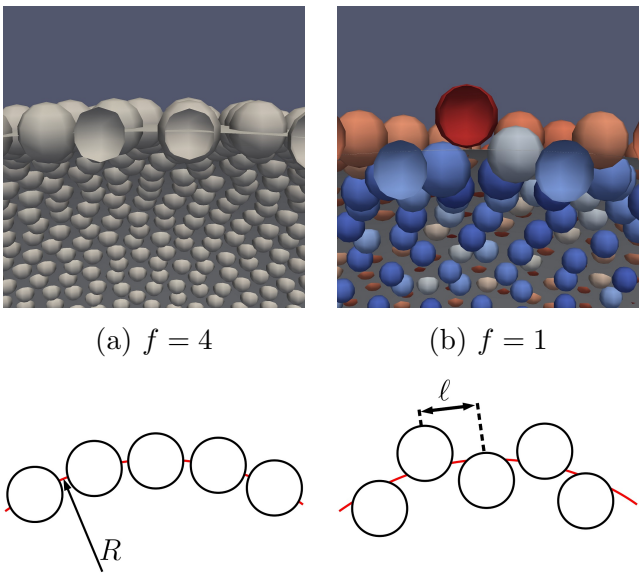

(a) $f = 4$ (b) $f = 1$

(c) Smooth buckling (d) Small-scale wrinkling

Figure 4.6: Top: Enlarged views of monolayer configuration for $t' = 139$. The case $f = 1$ (fig. b) is the enlarged view of fig. 4.5a, focusing on the near-interface region. The meaning of the colours is as in fig. 4.5. Bottom: schematics of monolayer configurations corresponding to the simulation results of the top panel.

simulations Brownian forces and gravity are not accounted for, so the particles remain close to the fluid interface after desorption. In Fig. 4.5a the particle layer appear to be diffused. This effect is simply due to the repulsion between the desorbed particles and the particles that are just undergoing desorption.

For intermediate adhesion strength, $f = 2$, no desorption is observed. The particle-covered fluid interface buckles, producing smooth wrinkles having a characteristic wavelength $\lambda_c \sim R$. For larger adhesion strength, $f = 4$, the fluid interface buckles creating wrinkles qualitatively similar to those obtained for $f = 2$. A notable difference between the simulations for $f = 2$ and $f = 4$ is that for $f = 4$ the ridge of one of the surface folds breaks up locally (figure 4.5i). This breakup is likely due to the larger out-of-plane particle displacement allowed by smaller values of f.

Figure 4.6 provides a detailed view of the structure of the particle monolayer for $f = 1$ and $f = 4$. For $f = 4$ the adhesion between the particles and the fluid interface is relatively strong. As a consequence the particles form a smooth monolayer that conforms closely to the fluid interface. For $f = 1$ the displacement of the particles from the fluid interface is instead larger. Neighbouring particles tend to reside on different sides of the fluid interface, forming small-scale wrinkles with characteristic width ℓ comparable to a. This type of particle monolayer structure, characterised by small-wavelength small-amplitude out-of-plane particle displacement, is defined as *small-scale monolayer wrinkling*. Desorption appears to be highly correlated with the degree of small-scale wrinkling of the particle monolayer.

The visualisations of figure 4.7 compare particle monolayer configurations before and after desorption for $f = 1$ and $f = 2$. These visualisations reveal that the particle monolayers display small-scale wrinkling both before and after desorption. When $f = 1$, the particle monolayer is wrinkled at small scales without the fluid interface showing signatures of "large-scale" buckling. For $f = 2$, the particle monolayer produced small-scale wrinkles only after the fluid interface has buckled significantly. Small-scale wrinkling thus does not follow from buckling, as this surface mode can be superimposed onto a spherical or a buckled interface.

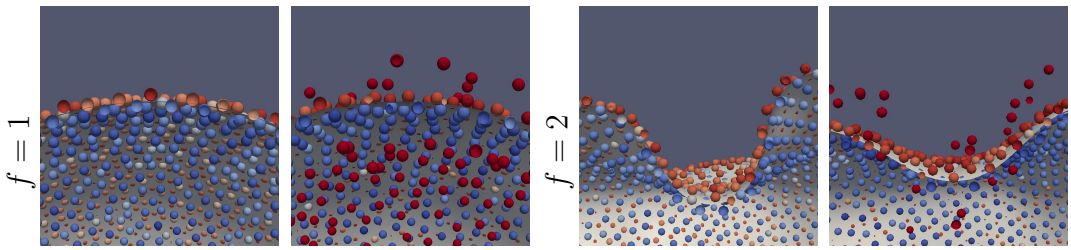

(a) $t' = 139$ (b) $t' = 278$ (c) $t' = 334$ (d) $t' = 361$

Figure 4.7: Enlarged views of particle desorption events for different values of f and $a/R = 0.02$. The panels on the left and on the right refer to before and after desorption, respectively. For the particles bound to the interface, the meaning of the colours is as in fig. 4.5. Desorbed particles are coloured in dark red.

A strong correlation between small-scale wrinkling and desorption is expected from consideration of the magnitude of the force exerted on a given particle in the direction normal to the fluid interface. This normal force is due to the lateral forces exerted by neighbouring particles. For a particle residing on a monolayer having local curvature $\mathcal{C}$, simple geometric arguments [190] enable to estimate the normal force on each particle as

$$F \simeq \frac{1}{2} N_c F_t a \mathcal{C} \tag{4.3}$$

where N_c is the local coordination number and $F_t \simeq 2\pi\Pi_s a$ is the average tangential inter-particle force (in the derivation it is assumed $a\mathcal{C} \ll 1$ to obtain the dominant-order scaling). For a buckled monolayer, the observed wavelength $\lambda_c \sim R$ gives $F \simeq \frac{1}{2} N_c F_t \frac{a}{R}$. For a monolayer displaying small-scale wrinkles - whether long-wavelength buckling occurs or not - the observed wavelength $\lambda_c \sim \ell$ gives $F \simeq \frac{1}{2} N_c F_t \frac{a}{\ell}$ to leading order. Recalling that $\ell \sim a$, the local normal force acting *locally* on the particles in the case of small-scale wrinkling is thus $O(R/a)$ larger than for buckling. Because $a \ll R$, the normal force in the case of a particle monolayer with small-scale wrinkles can thus be much larger, for the same value of the surface

pressure, than in the case of a monolayer presenting smooth folds. The coupling between normal force and curvature is thus a mechanism that predicts enhanced probability of desorption as a/R increases.

Effect of size ratio. The visualisations in figure 4.8 show the effect of changing a/R on the drop morphology for $a/R = 0.01$, 0.04 and 0.08. In the current simulations, the drop radius R is fixed while the particle radius a is increased. Increasing a has several consequences in the framework of FIPI: first the capillary force between fluid interface and particle will be stronger and the particle can remain farther from fluid interfaces while still being attached by capillary force (Equation (2.11)); secondly the particle-particle solid contact forces will be larger according to the model of Equation (2.14); thirdly the hydrodynamic drag (Equation (2.12)) experienced by the particle is larger. All three forces mentioned above experienced by particles scale linearly with the particle radius a. It should be noted that in the current simulations the surface area occupied by all the particles is kept as constant, therefore increasing a will quadratically reduce the number of particles on the surface of the drop.

A morphological transition occurs as a/R is increased, from a buckled drop shape for $a/R = 0.01$ to an almost spherical drop shape for 0.08. This qualitative observation is confirmed in figure 4.9, where the sphericity parameter $\Psi = \frac{\pi^{\frac{1}{3}}(6V)^{\frac{2}{3}}}{A}$ is plotted as a function of a/R (V is the volume of the region comprised within the fluid interface and A the surface area of this region). The sphericity parameter is defined so that the larger the deviation from a spherical shape, the smaller the value of Ψ. A perfectly spherical shape corresponds to $\Psi = 1$.

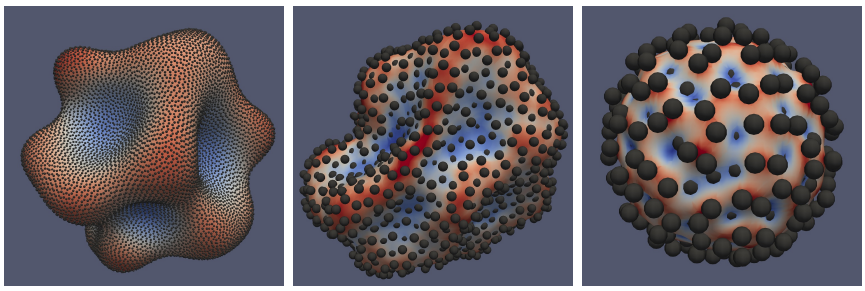

(a) $a/R = 0.01$ (b) $a/R = 0.04$ (c) $a/R = 0.08$

Figure 4.8: Surface morphology for different values of a/R and $f = 2.0$. The time instant is $t\gamma/(R\mu) = 278$. The fluid interface is coloured according to its local curvature.

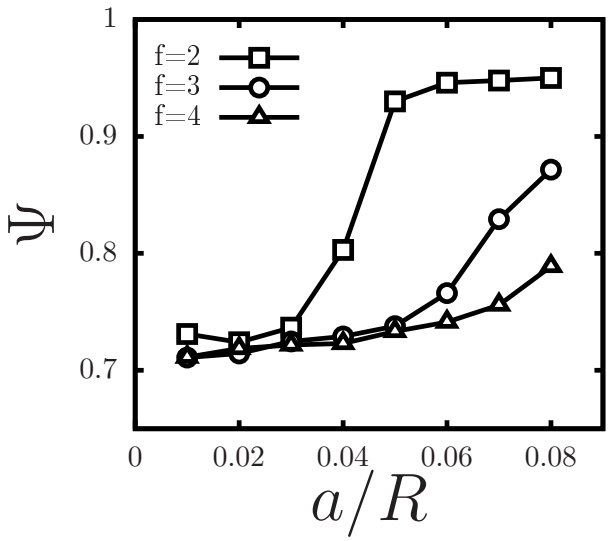

Figure 4.9: Sphericity parameter as a function of a/R for different value of f and $t\gamma/(R\mu) = 278$.

The critical range of values of a/R for which the transition occurs, and how strong the dependence of Ψ on a/R is, depend sensitively on f. For $f = 2$ a transition from an almost spherical ($\Psi \simeq 0.95$) to a non-spherical shape occurs for a/R in the range $0.03 - 0.05$. As f increases, the transition becomes less sharp, the maximum value of Ψ is reduced, and the critical range of values of a/R for which the most marked change in Ψ occurs shifts to the right. The possibility of

observing of a spherical shape despite the surface pressure value $\Pi_s > \gamma$ is easy to explain. For relatively small values of f, the particles can release the surface stress by moving slightly outwards towards larger value of d. This displacement reduces the surface pressure below the buckling value $\Pi_s = \gamma$, hence the drop maintains a spherical shape. Of course, this effect is only possible if Π_s is only slightly larger than γ. However, It is found from the simulations that values of Π_s significantly larger than γ are difficult to obtain when small-scale monolayer wrinkling takes place, because the particles tend to desorb before such relatively large surface pressure values are reached.

The results in Figure 4.8 and 4.9 give an indication of the overall shape of the drop, but do not characterise the displacement of the particle monolayer surface from the fluid interface. To address this point, the mean value $\langle d \rangle$ averaged across all the particles on the drop surface and the corresponding standard deviation $d_{std} = (\langle (d - \langle d \rangle)^2 \rangle)^{1/2}$ of the out-of-plane displacement d are shown in Figure 4.10. These statistics are computed by averaging, for a fixed time $t\gamma/(R\mu) = 278$, over all the particles in the monolayer.

Figure 4.10a shows that the mean value of the displacement increases with a/R. Equation (4.3) indicates that a linear relation holds between the average value of F and the average value of $\mathcal{C}$, which in turn would suggest $\frac{\langle d \rangle}{a} \propto a/R$ (the restoring capillary force in the current model is linear in the displacement). A linear relation between $\frac{\langle d \rangle}{a}$ and a/R indeed holds, although approximately, suggesting the validity of Equation (4.3) in an average sense.

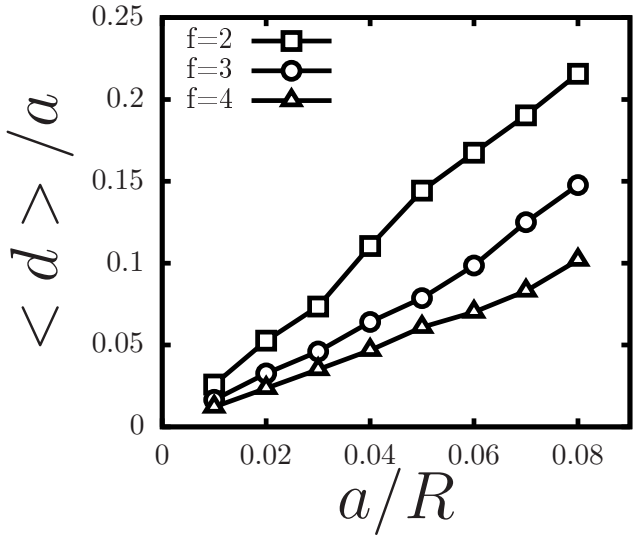

(a)

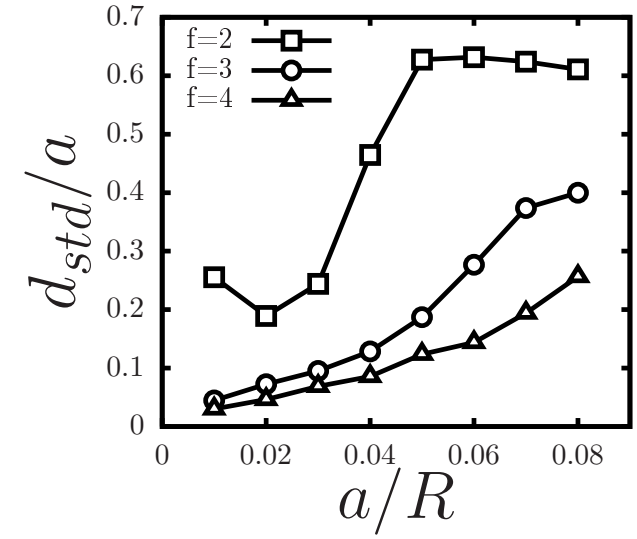

(b)

Figure 4.10: Statistics of the out-of-plane displacement field d for $t\gamma/(R\mu) = 278$: (a) mean value averaged over all the particles on the drop surface; (b) the corresponding standard deviation.

The standard deviation of the displacement also increases with a/R (figure 4.10b). This effect is stronger for $f = 2$ than for $f = 4$, so it cannot be attributed to buckling. It is the manifestation of the appearance of small-scale undulations

in the particle monolayer, hence of small-scale monolayer wrinkling.

Interestingly, small-scale monolayer wrinkling, as measured by d_{std}/a, appear to increase with a/R. Thin elastic sheets on curved substrates develop buckling patterns whose amplitude and spatial distribution depend on the substrate curvature [191]. From a continuum perspective, a particle-covered drop can be viewed as an incompressible thin sheet (the particle monolayer) adhered to a soft curved surface (the drop), so a dependence of the amplitude and wavelength of the buckling pattern on the curvature of the drop is conceivable.

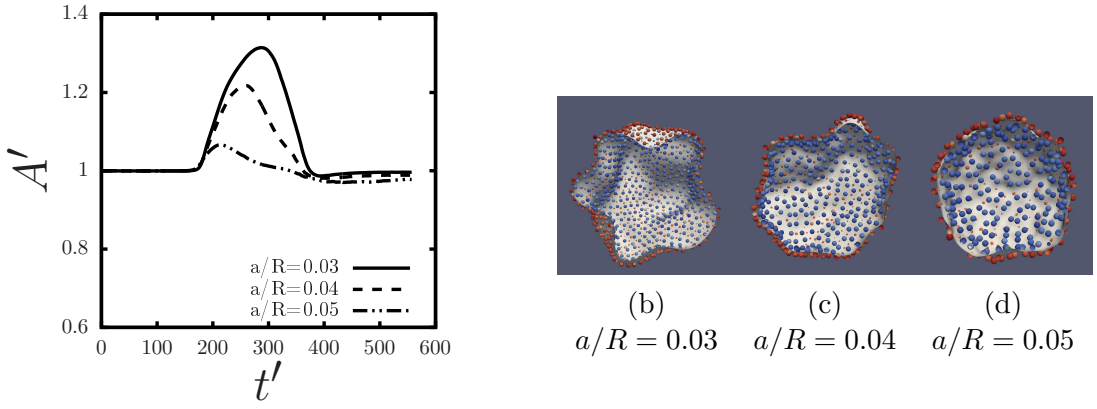

(a)

(b) $a/R = 0.03$ (c) $a/R = 0.04$ (d) $a/R = 0.05$

Figure 4.11: (a) Time evolution of the normalised surface area $A' = A/A_0$ for different values of a/R and $f = 2.0$. The surface area is normalised by its initial value A_0. Time is normalised by the capillary time scale $t' = t\gamma/(R\mu)$. (b)-(d) Cross-sectional views of particle monolayer and fluid interface for different values of a/R. For each value of a/R, the time instant chosen correspond to just before the onset of desorption. Particles are coloured according to their signed distances from the fluid interface.

In Figure 4.11a the effect of changing a/R on the time evolution of the non-dimensional surface area $A' = A/A_0$ is examined. The following cases are considered: $a/R = 0.03$, 0.04 and 0.05. This is the range of values of a/R for which the largest variation in the sphericity parameter and d_{std} is observed. For $t' < 200$, roughly, A' is constant. For this range of values of t' the inter-particle force param-

eter k_c increases, following the linear variation of mode 2, but because the surface pressure does not exceed the buckling threshold the drop remains spherical. For $t' > 200$, A' increases, indicating that $\Pi_s > \gamma$. The non-dimensional surface area decreases after reaching a maximum that depends on a/R. This decrease is due to particle desorption, which enables the drop to slowly recover the original spherical shape.

The visualisations of figure 4.11b show the drop shape and the monolayer configuration for the time instant for which A' has a peak. These figures show that the monolayer displays small-scale wrinkling before desorption (red and blue colours refer to particles inside and outside the monolayer).

Although figure 4.11b and others presented in this study do not strictly speaking prove a causality relation between small-scale monolayer wrinkling and desorption, a strong correlation between these events appear to exist. A particle-level mechanisms exists. For a fixed value of Π_s/γ, small-scale monolayer wrinkling increases the normal force on each particle due to local particle monolayer curvature effects, and this makes particle expulsion more likely.

4.3 Discussion

The simulation results presented in the previous sections suggest a complex dependence of the drop morphology and desorption dynamics on the non-dimensional parameters Π_s/γ, a/R and f, of which only a few selected values are explored. In figure 4.12 a configuration diagram is proposed that could help understand this dependence for a broader range of parameter values.

For buckling to occur the surface pressure induced by the particles must be

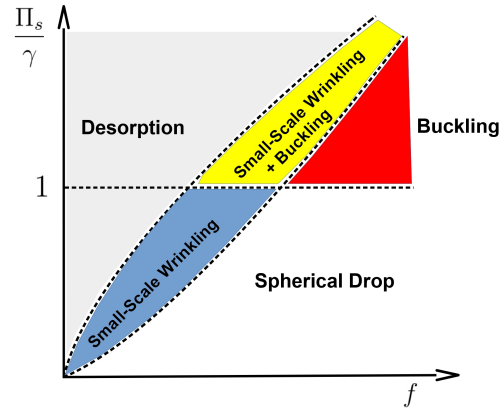

(a)

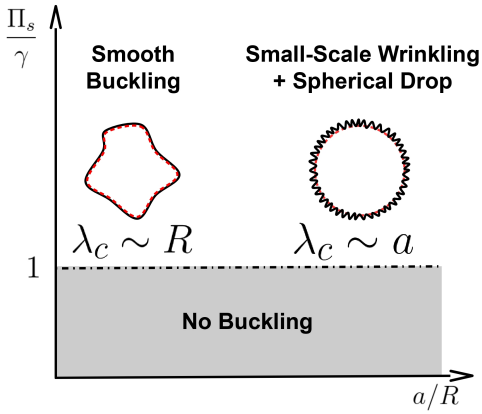

(b)

Figure 4.12: Configuration diagrams of the qualitative dependence of the monolayer configuration on: (a) Π_s/γ and f, for intermediate and small values of a/R ; (b) Π_s/γ and a/R, for intermediate and large values of f. In (b) the continuous line (black) represents the particle monolayer and the dashed line (red) represents the fluid interface.

larger than the bare surface tension γ (Figure 4.12a). This is true whatever the value of f. The loss of the spherical symmetry for $\Pi_s = \gamma$ is intuitive. For $\Pi_s = \gamma$ the particle-covered interface becomes a tensionless, floppy membrane that can buckle under any small perturbation (unless there is a mechanism that endows the particle-covered interface with a finite bending rigidity; in this last case buckling is expected to occur for a surface pressure slightly larger than γ). Buckling for values of Π_s smaller than γ has been reported for Langmuir trough experiments,

but this effect has been ascribed to cohesiveness (which implies attractive inter-particle interactions, which are absent in the current simulation) or to experimental difficulties in measuring the "true" surface pressure [66]. These difficulties are associated to the fact that in Langmuir trough experiments the deformation is uni-directional, the surface pressure probe can disturb the surface displacement field, and the film can deform plastically. The surface stress can therefore be nonuniform and anisotropic even if the deformation is relatively simple.

For $\Pi_s < \gamma$, buckling cannot occur. Therefore the possible non-trivial outcomes of the interface compression are small-scale monolayer wrinkling or particle desorption. Desorption tend to occur when f is relatively small (see e.g. the uniform desorption of figure 4.5), because in this case the particles are very weakly attached to the fluid interface. Small-scale monolayer wrinkling can occur for intermediate values of f. In this case, even though Π_s is smaller than γ the surface pressure can be sufficiently large to push the particles slightly out of the of the fluid interface. For large values of f small-scale monolayer wrinkling is negligible. Because $\Pi_s < \gamma$, the particle-covered drop remains spherical and the particle monolayer conforms to the spherical drop surface.

For $\Pi_s > \gamma$, two limiting behaviours separated by an intermediate regime can arise. Particle desorption takes place for "small" values of f. Pure buckling takes place for "large" values of f (in this case the monolayer is strongly bound to the fluid interface, so the surface pressure can only be released by out-of-plane buckling of the particle-covered fluid interface). An intermediate behaviour characterised by smooth buckling superimposed on small-scale monolayer wrinkling can occur. The diffuse transition region corresponding to this intermediate behaviour is indicated in yellow in Fig. 4.12. In the transition region f is not small enough to give desorption, but is sufficiently small to allow a significant particle displacement

from the fluid interface.

The range of critical values of f separating desorption from pure buckling should somewhat depend on the surface pressure. Equation (4.3) suggests that the critical value of the normal force giving desorption, $f\gamma a$, is reached for $f \sim \frac{\Pi_s}{\gamma}\frac{a}{R}$. This estimate suggests a linear relation between f and Π_s in the transition region (this estimate assumes uniform interface curvature, and is thus just a rough approximation). In the absence of more information, the transition region is indicated as a diffuse region around a line in the $\Pi_s - f$ plane.

Figure 4.5 suggests a significant morphological transition for f between 1 and 2. This range of values for f correspond to a relatively small change in contact angle, between 72° and 90° (Figure 2.2). This result suggests that different experiments with slightly different contact angles could give widely different outcomes when one examines the occurrence of buckling versus desorption.

For $\Pi_s > \gamma$ the particle monolayer displays different surface patterns depending on the value a/R (Figure 4.12b). In the case of "small" values of a/R, the simulations suggest a pure buckling pattern characterised by long-wavelength $\lambda_c \sim R$ folds. For "large" values of a/R the overall shape of the drop is spherical, and the monolayer displays small-scale wrinkling, with ridges separated by a characteristic wavelength $\lambda_c \sim a$ (as in Fig. 4.8c). A mixed behaviour (not illustrated in Figure 4.12b) may occur for intermediate values of a/R, whereby small-scale monolayer wrinkling is accompanied by smooth buckling. This physical picture is characteristic of intermediate and large values of f. For small values of f the particles will desorb and the drop will remain spherical.

Particle desorption in correspondence to particle monolayer ridges may be interpreted as a stress focusing mechanism [192] channeling the average macroscopic

overstress $\Pi_s - \gamma$ into surface features having spatial extent much smaller than the surface of the drop. A curvature-dependent "wrinkle-to-crumple" transition from smooth, long-wavelength wrinkles to localised deformation is a generic feature that have been shown to occur for a variety of highly bendable and incompressible thin sheets [193].

The literature often refers to the particle-laden interface as if it was made up by a unique entity, neglecting the distinction between the particle phase and the fluid interface. It is believed that this distinction is essential, as small deformations of the monolayer with respect to the fluid interface can result in relatively large local normal forces owing to the local monolayer curvature, in certain cases causing particle expulsion.

If the desorption process involves many neighbouring particles, the detachment of a particle monolayer from a fluid interface is akin to a buckling-induced delamination between two continuous sheets. The difficulty in applying continuum-level results [194–196] to particle desorption is the granular nature of the particle monolayer, which makes the desorption dynamics sensitive to the presence of defects, and the stress in the monolayer non-uniform and difficult to predict.

4.4 Conclusions

The simulations with the FIPI method [197] of the compression of a particle-covered drop are presented to understand the parameters affecting the change in morphology of the particle monolayer and of the fluid interface, and the conditions leading to particle desorption. The simulations are analysed as a function of the non-dimensional capillary adhesion strength f (which in experimental settings is

primarily a function of the contact angle), the particle-to-drop size ratio a/R and the ratio Π_s/γ between the particle-induced surface pressure and the bare surface tension.

A general conclusion from the current observation is that particle desorption is always associated to relatively low values of f. This conclusion agrees with the results of Langmuir trough experiments on planar interfaces [60, 66]. In experiments, low values of f are the result of contact angles values for which the particle resides mostly in the subphase. While it could be assumed that contact angles for which the particle resides mostly in the superphase could also give desorption, gravity can keep the particles close to the interface [66], reducing the probability of observing desorption. In the current model gravity is absent, but the curvature of the drop introduces an asymmetry, causing the particles to be expelled mostly from the interior of the drop outwards. Dimensional analysis of the current mathematical model makes it clear that what is important is not intrinsically the particle size, the surface tension, or the adsorption energy , but the non-dimensional ratio f of these quantities.

A mode of deformation of the monolayer is identified, which is termed small-scale monolayer wrinkling. It is a term used to describe the appearance of small amplitude, small-wavelength $\lambda_c \sim a$ undulation in the surface of the particle monolayer, which can be superimposed onto a smooth monolayer surface.

An important question is whether small-scale monolayer wrinkling could be observed in experiments. The current simulations are carried out under ideal conditions: the particles have identical size, identical wetting properties (f is constant), and can slide freely past each other because of the absence of tangential inter-particle interactions. As a consequence, under a spherically symmetric com-

pression of the drop (mimicked in out simulation through an increase in Π_s), the properties of a point in the monolayer surface are identical in an average sense to those of any other point. The uniformity of particle properties and the isotropic geometry of the drop lead to a relatively uniform and isotropic small-scale surface pattern. In contrast, under realistic experimental conditions it is expected that particle size polydispersity, small differences in contact angle, and non-uniform interparticle interactions, will lead to a more inhomogeneous small-scale monolayer wrinkling and, in the limiting case of extreme inhomogeneity, to the appearance of "surface defects" in the monolayer arrangement. However, the basic conclusions, that an increase in surface pressure leads to small-scale out-of-plane monolayer deformations, and that such out-of-plane deformations are precursors to particle desorption, are expected to be valid even in relatively complex experimental conditions.

Chapter 5

Fluidisation of Cohesive Powder

Fluidisation has always been a classic problem studied with simulations using discrete element methods [198–200]. As a side project in collaboration with GlaxoSmithKline, the problem of fluidisation of cohesive powder has been investigated in this chapter, using both continuum level simulations and particle tracking code adopted from the FIPI. It was reported previously [201] that cohesive powders can be fluidised in a way that the powder particles form agglomerates leaving the bed chunk by chunk. The aim of this project is to understand the correlation between the agglomerate sizes and the properties of the powder materials.

5.1 Overall Methodology

The air velocity field inside the channel filled with powder is simulated with PorousSimpleFoam solver in OpenFoam by the modelling the powder bed as a chunk of porous media. For investigations of fracture mechanics of the powder bed, we have adopted two approaches: the first approach is to treat powder bed as a continuum

solid chunk and study the stress profile by using solid stress analysis solver from OpenFoam; the second approach is to simulate fracture dynamics by our in-house code with a recipe for handling cohesive interactions between the particles. The overall methodology are summarised in Figure 5.1.

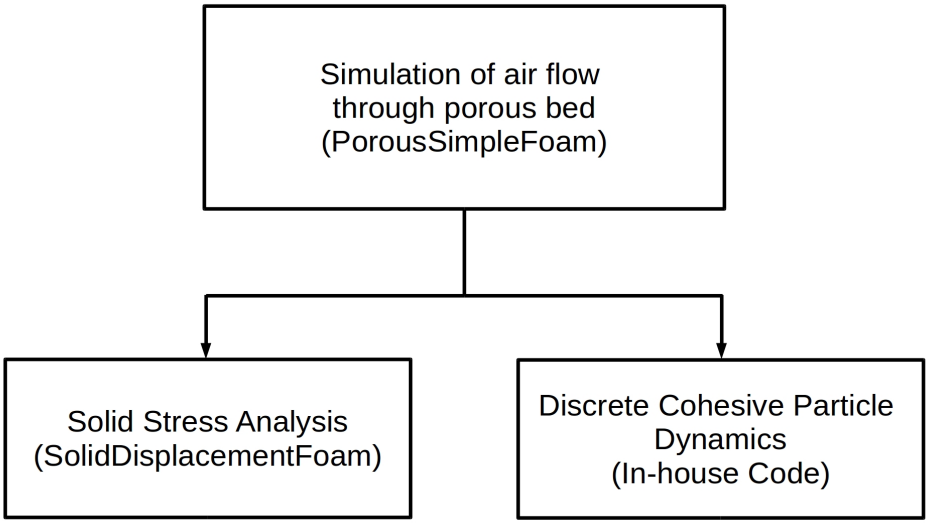

Figure 5.1: Methodologies for investigating fracture of powder bed inside channel of DPI.

5.2 Simulation of Air Flows Passing Through Porous Media

In PorousSimpleFoam, the air velocity field inside channel is computed by solving Darcy-Brinkman-Forchheimer equation

$$\rho\frac{\partial \mathbf{U}}{\partial t} + \mathbf{U}\cdot\nabla\mathbf{U} = -\nabla p + \mu\nabla^2\mathbf{U} - \mathbf{S}, \tag{5.1}$$

where **S** accounts for drag forces coming from the porous media. The **S** is modelled as

$$\boldsymbol{S} = \frac{\mu}{K}\boldsymbol{U} + \frac{\rho}{K_i}\left|\boldsymbol{U}\right|\boldsymbol{U}, \tag{5.2}$$

where the two terms on the right hand side are Darcy term and Forchheimer term, representing viscous and inertial drag from porous media respectively. K and K_i are the apparent permeability and inertial permeability of the porous material. We approximate their values by $K = a^2$ and $K_i = a$ where a is the radius of the particles within the powder bed. The ratio of the inertial drag over viscous drag is indeed particle Reynolds number:

$$Re_p = \frac{\text{Forchheimer term}}{\text{Darcy term}} = \frac{a\rho U}{\mu} \tag{5.3}$$

For a powder bed filled with lactose particles with $50\mu m$ radius in a typical inhaler with air velocity of $20m/s$, the particle Reynolds number is approximately 120. The inertial drag dominates the viscous drag and will be the major driving force for breaking up the lactose powder bed.

The simulations of air flow passing through porous powder bed inside U-shape channel have been performed with different bed height. The overall qualitative results with sketch of simulation domain geometry are illustrated in Figure 5.2. The simulations are done by imposing a total pressure drop of $3000Pa$ between inlet and outlet of the U-shape channel. The channel has a square-shape cross section of $2mm \times 2mm$. The stream-wise length of bottom channel is $6mm$. The height of the inlet channel $8mm$ to allow the air flow fully develops before reaching the powder bed at bottom.

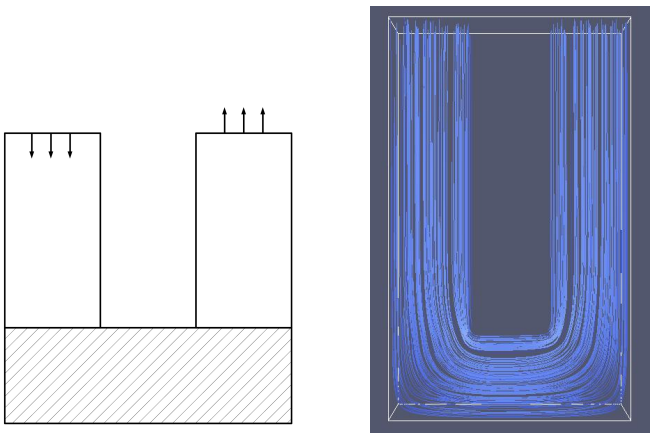

(a) Full channel filled with powder

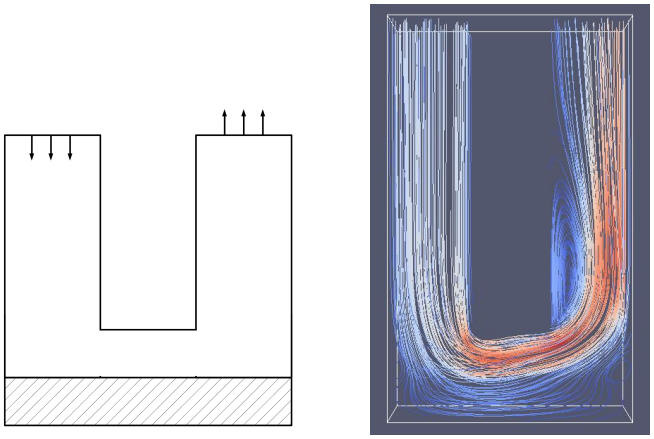

(b) Half channel filled with powder

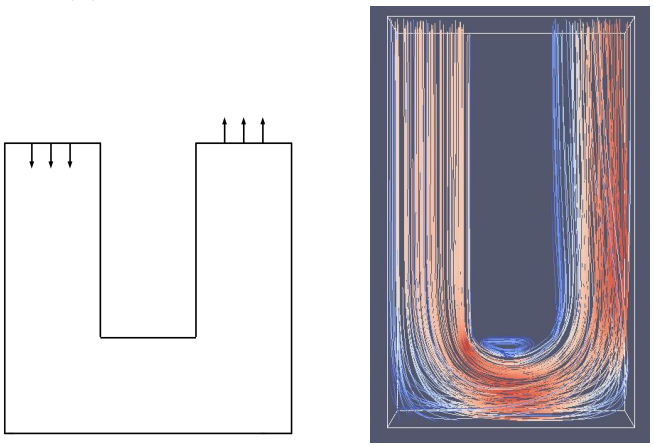

(c) Channel without powder bed

Figure 5.2: Left: Sketch of domain geometry for simulations of air flow passing through U-shape channel filled with powder bed of different height. The hatched regions correspond to porous powder bed and white region is air. Right: Corresponding snapshots of streamlines of air velocity field coloured according to the magnitude of velocity. The pressure difference between inlet and outlet is 3000 Pa and the permeability of porous powder bed is set to $10^{-8}m^2$.

The volumetric flow rate of air passing through the channel is measured as a function of the permeability of the powder bed. The results are shown in Figure 5.3. The air flow rate passing through the channel is more influenced by the permeability of the powder bed when the bottom channel is partially or fully blocked by the powder bed. Typical human inhalation flow rate referred by the industry is $60L/min$. By comparing this reference value with our simulation results, it is evident that only less than 20% of the air flow can pass through the channel in the best case scenario (when there is no powder inside channel). The maximum volume flow rate passing the channel can also be estimated by calculating the possible maximum velocity inside the channel. This is done by using Bernoulli equation. Neglecting gravity, with a total head drop of $\Delta p = 3000Pa$, the maximum velocity inside channel should satisfy $\frac{1}{2}\rho U_{max}^2 = \Delta p$. For air this gives $U_{max} \approx 70m/s$. The average air flow velocity of a cross stream section is approximately $0.5U_{max}$.

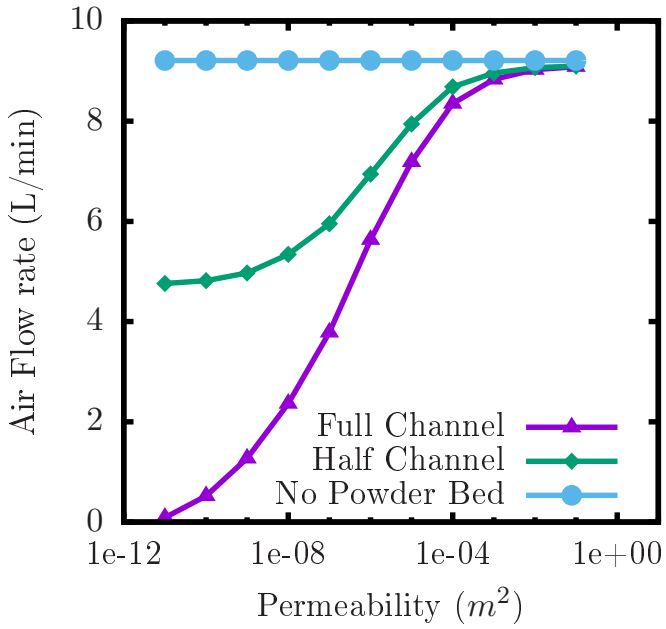

Figure 5.3: Volumetric flow rate of air passing through the channel under the pressure difference of 3000 Pa.

5.3 Continuum Solid Stress Analysis

In OpenFoam, solid stress analysis is done within the framework of linear continuum elasticity. The displacement field **D** within the powder bed is computed by solving the Cauchy stress equation incorporated the porous drag term **S** in Equation 5.1.

$$\rho\frac{\partial^2\mathbf{D}}{\partial t^2} - \nabla\cdot\left[\mu_s\nabla\mathbf{D} + \mu_s\left(\nabla\mathbf{D}\right)^T + \lambda_s\mathbf{I}tr\left(\nabla\mathbf{D}\right)\right] = \mathbf{S} \tag{5.4}$$

where μ_s and λ_s are Lame first and second parameter respectively. The stress tensor inside the powder bed can be calculated as:

$$\sigma = \lambda_s\left(\nabla\cdot\mathbf{D}\right)\mathbf{I} + 2\mu_s\epsilon, \tag{5.5}$$

where

$$\epsilon = \frac{1}{2}\left[\nabla\mathbf{D} + \left(\nabla\mathbf{D}\right)^T\right]. \tag{5.6}$$

The simulation is done by using the solver SolidDisplacementFoam. To calculate the additional forcing term due to the porous drag, the results of air velocity field from fluid simulation are subtracted and used as the initial condition for the simulation of solid displacement field. The boundary conditions are set according to the outside media in contact with the boundaries, as shown in Figure 5.4.

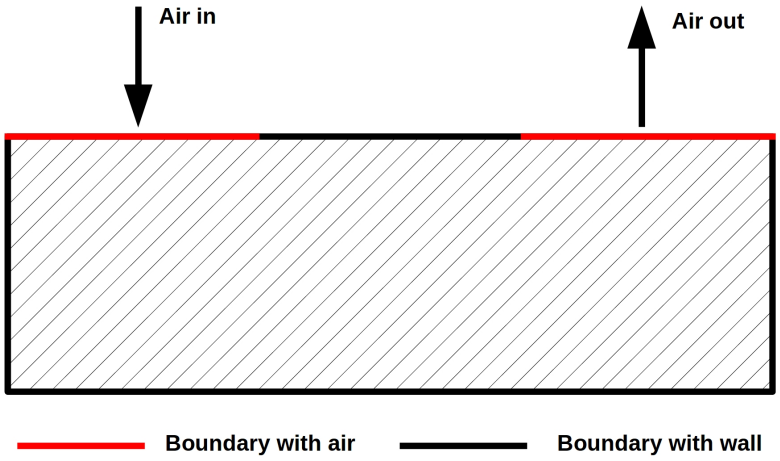

Figure 5.4: Sketch of domain of powder bed used in solid stress analysis.

The free traction boundary condition is assigned to the boundaries with air. There are two options for the boundary conditions with channel wall: one is free-slip, the other is no-slip. The choice of boundary conditions for channel wall really depends on the interactions between the powder particles and the channel wall. If the powder particles are firmly attached to the wall and have zero degree of freedom to move, then no-slip BC should be employed. Otherwise if powder particles can slide along the wall then free-slip or partial-slip would be more appropriate. Depending on the cohesion strength between channel wall and powder particles, powder particles can detach from channel wall given that the air flow is strong enough. In reality the real boundary conditions can be dynamically changing between each cases under different aerodynamic loading.

To be practical, simulations with different boundary conditions are performed. The resulting stress profiles inside powder bed are dramatically different between

each case, which are illustrated in Figure 5.5.

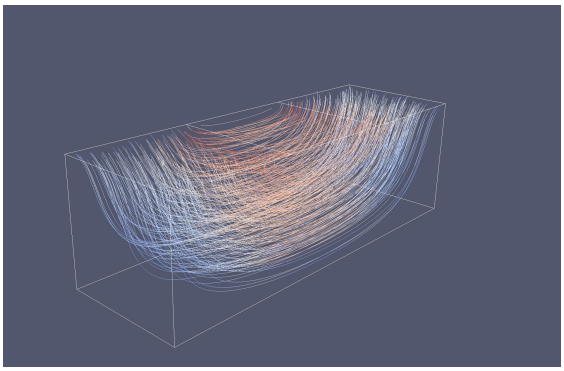

(a) Streamline of air flow coloured with magnitude of velocity.

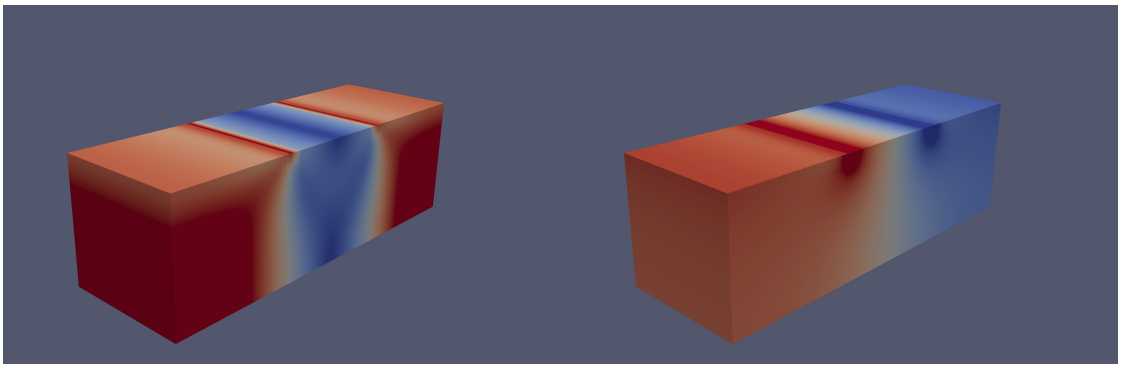

(b) Free-slip boundary condition. Left: Von Mises stress. Right: Tension.

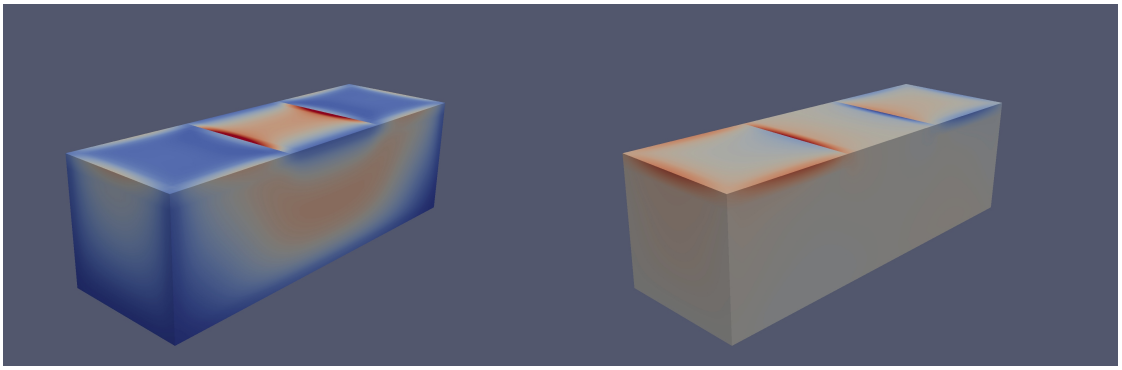

(c) No-Slip boundary condition. Left: Von Mises stress. Right: Tension.

Figure 5.5: Different boundary conditions give different stress distribution inside powder bed.

Air flow passing through the powder bed is visualised by streamlines in Figure 5.5(a), showing the magnitude of velocity is larger around the inner corner of U-shape channel. Von Mises stress is the equivalent tensile stress when the material

is under multiaxial loading and tension is the measure of the hydrostatic loading condition. The two stresses are independent from each other. We suppose that the fracture will occur when either Von Mises stress or tension reaches a critical value.

When free-slip BC is employed, high Von Mises stress is concentrated around the bottom corners of the powder bed. Within middle section there is negligible Von Mises stress. The tension is positive in the upstream half and negative in the downstream half of the powder bed. While when no-slip BC is employed, both Von Mises stress and tension are largely suppressed in the bulk region of the powder bed. The highest Von Mises stress and tension appear near the inner corner of the channel at the top of the powder bed.

From the current results of continuum solid stress analysis, it is evident that the stress distribution inside powder bed is highly dependent on the boundary conditions between the powder and the channel wall. The importance of the boundary conditions have been neglected in the previous studies. We believed that since the particles comprising the powder are cohesive, there will be cohesion between the particles and the channel walls to an extent as well.

The investigations by performing continuum stress analysis did not give information about the chunk sizes distribution from fracture fluidisation. But it is an essential step which made us realise the importance of the boundary conditions. In the following studies, we performed the simulations of fracture fluidisation with our in-house code in which particle-wall cohesions are included.

5.4 Cohesive Discrete Particle Dynamics

To gain details about the fracture fluidisation of the powder bed, it is essential to do simulations within the framework of discrete particles. There are already many well established Discrete Element Methods (DEM) for simulations of granular material, which employs Coulomb type friction for particle-particle interactions. However, the performance of these methods to predict the dynamics of cohesive powder is subject to debates. For Coulomb type friction models, the tangential cohesion force is zero when normal force is zero between two particles, which is not always correct for cohesive contacts in reality. In many cases, there are resistances to sliding within a cohesive contact even when the normal force is not present (duck tape, etc). To simulate the fracture fluidisation of cohesive powder bed, we have proposed a new particle-particle interaction model for cohesive particles.

5.4.1 Particle-Particle Interaction Model

Along the normal direction between two spherical particles, we follow the standard DEM approach where a spring dash-pot model combined with adhesion is used.

$$\boldsymbol{F}_n = \begin{cases} -F^{max}_{adhesion}\hat{\boldsymbol{d}} - k_n\delta_n\hat{\boldsymbol{d}} - \eta\boldsymbol{u_n}, \text{ when } \delta_n < 0 \\ -F^{max}_{adhesion}\hat{\boldsymbol{d}} + \dfrac{F^{max}_{adhesion}}{r_n}\delta_n\hat{\boldsymbol{d}} - \eta\boldsymbol{u_n}, \text{ when } 0 < \delta_n < r_n \\ \boldsymbol{0}, \text{ when } \delta_n > r_n \end{cases} \tag{5.7}$$

where $\delta_n = d - (R_1 + R_2)$ is the gap between two particles, $\hat{\boldsymbol{d}}$ is the unit distance vector pointing from nearby particle to the current particle, r_n is the range of cohesive interaction and $F^{max}_{adhesion}$ is the maximum cohesive force allowed between particles. The magnitude of this force is estimated from the tensile strength of the

powder assuming cubic packing as shown in (a) of Figure 5.6.

$$F_{adhesion}^{max} = \sigma_t D^2 \tag{5.8}$$

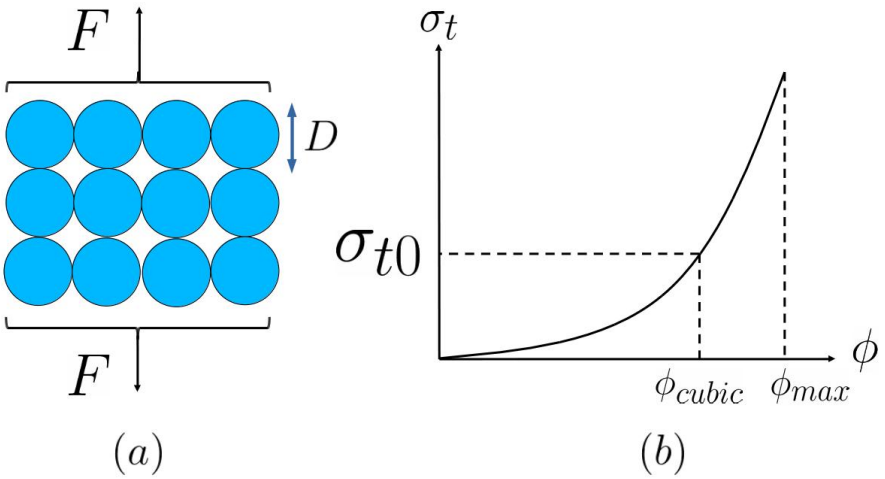

Figure 5.6: Left: Sketch of the cubic packing used for estimating cohesion forces between particles from global tensile strength. Right: Qualitative plot of real tensile strength as a function of packing volume fraction of powder.

As depicted in (b) of Figure 5.6, the real tensile strength of the powder should depends on the packing volume fraction of the powder. From now on we will refer the tensile strength σ_t as the tensile strength estimated from cubic packing σ_{t0} from our model.

Along the tangential direction we discard the coulomb type friction scheme since it is not appropriate for modelling the sliding between adhesive surfaces. For two adhesive surfaces in contact there is strong resistance to shearing or sliding

even without normal load applied.

$$\boldsymbol{F}_t = \begin{cases} -0.57F^{max}_{adhesion}\hat{\boldsymbol{\delta}}_t + k_t\boldsymbol{\delta}_t - \eta\boldsymbol{u}_t, \text{ when } |\boldsymbol{\delta}_t| < r_t \text{ and } \delta_n < r_n \\ \text{Reset } \boldsymbol{\delta}_t \text{ to } \mathbf{0}, \text{ when } |\boldsymbol{\delta}_t| > r_t \text{ and } \delta_n < r_n \\ \mathbf{0}, \text{ when } \delta_n > r_n \end{cases} \tag{5.9}$$

where

$$\boldsymbol{\delta}_t = \int_{t_0}^{t} \boldsymbol{u_t} dt \tag{5.10}$$

The pre-factor 0.57 takes into account the relation between shear strength and tensile strength according to Von Mises criterion.

From experimental observation we can see the collisions between lactose particles are highly dissipative. The rate of dissipation during collisions is dictated by damping coefficient η which is calculated as

$$\eta = 2\gamma\sqrt{mk_n} \tag{5.11}$$

where γ can be determined from the restitution coefficient e in absence of cohesion between particles

$$\gamma = -\frac{\log e}{\pi\sqrt{1 + \frac{(\log e)^2}{\pi^2}}} \tag{5.12}$$

We set $e = 0.8$ for all simulations of fluidisation of lactose powder.

The time step of the simulation is chosen to be several times smaller than the period of oscillation of the spring mass system $t = 2\pi\sqrt{\frac{m}{k_n}}$.

Overall, the particle-particle interaction can be summarised with the sketch shown in Fig.5.7. The red solid line is the solid boundary of the current test par-

ticle. When a nearby particle is overlapping with the region enclosed by dotted line defined according to r_n, there will be attractive force bringing the neighbour particle to get contact with the test particle physically. Once the neighbour particle is overlapping with the solid boundary of the test particle, attractive force is replaced by a strong repulsive contact force which will separate them apart. As long as part of the neighbour particle remains in dotted circle, there will always be tangential spring resistance force which tries to bring two particles back to their original relative angular positions when they first get into contact.

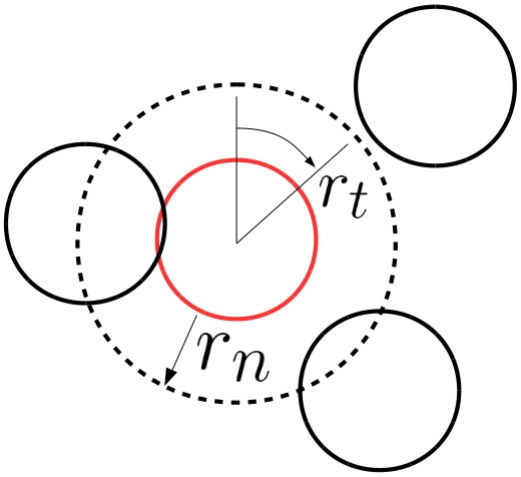

Figure 5.7: Sketch of the range of interaction between particles.

As we have learnt from continuum solid stress analysis, the boundary conditions between powder bed and channel walls have dramatic effects on the stress distribution inside powder bed. Here we are treating the particle-wall interactions exactly the same with particle-particle interactions. The particles in contact with the wall will remain attached to the wall under zero or moderate external forces. If the external forces is stronger than the cohesion strength between the wall and the particles, the particles can slide or detach from the walls.

5.4.2 Simulation Set-up

The simulation set-up can be summarised in Figure 5.8. Initially, the air velocity inside channel is set to 0. The powder particles are distributed with uniform probability inside bottom section of the channel. The particles are allowed to free sediment for $0.02s$ to ensure the powder bed reaches a static condition at the bottom. Afterwards, the air velocity inside the channel starts to ramp up linearly for $0.1s$ before reaching the air velocity field that is interpolated from the results of simulations of air flow through porous media.

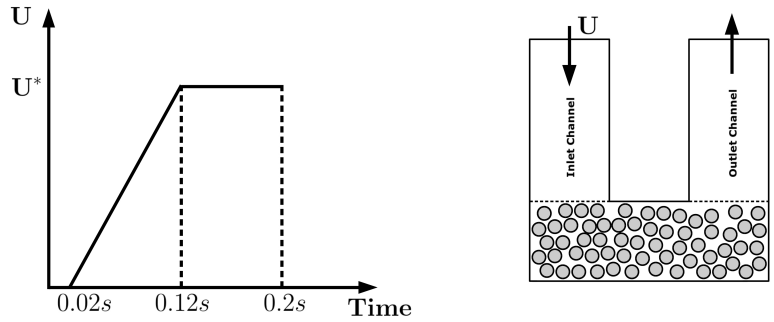

(a) (b)

Figure 5.8: Simulation setup: (a) Time evolution of ramping up air flow velocity inside channel to the prescribed $\mathbf{U}^*$. (b) Sketch of the geometrical domain of the simulations.

The interpolated air velocity field U^* is generated by a pressure drop of $3kPa$ when the powder bed fully occupies the bottom of the channel. The ramp-up period is set to $0.1s$ to reproduce the same conditions in previous experimental studies in which the pressure drop increases at a rate of $30kPa/s$.

5.4.3 Result

First inspection of the fracture process Depending on the tensile strength prescribed to the powder, the fracture can occur at different time instant or do not occur at all. One typical example is shown in Figure 5.9. For $\sigma_t = 100Pa$, The powder breaks up horizontally into two chunks near the inlet inner corner of the channel at $t = 0.08s$. At $t = 0.12$ most of the bulk region of the powder bed has already moved into the outlet channel with lots of smaller chunks created by powder bed breaking up vertically. For $\sigma_t = 200Pa$, the initial fracture occurs at a much later instant. The primary break-up is still at inner corner of inlet channel. For $\sigma_t = 300Pa$, no fracture is observed during the simulation time span.

The fracture of powder bed encountered during our simulations can be approximately categorised into two types: horizontal fracture and vertical fracture (illustrated in Figure 5.10). The horizontal fracture happens usually at the inner corner of the channel near the inlet. The vertical fracture happens usually in the region of the powder bed directly facing the outlet channel.

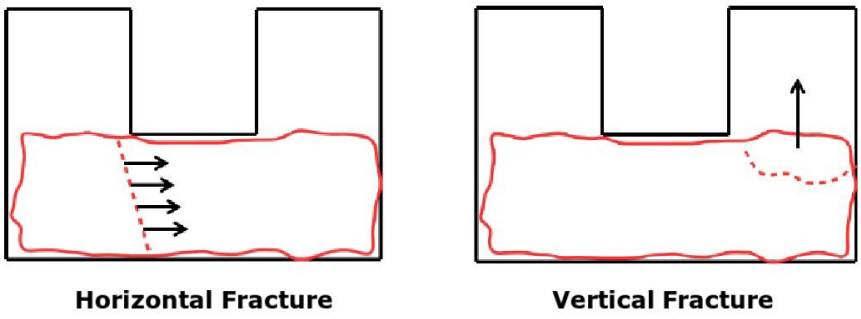

Figure 5.10: Two types of fracture modes observed during the simulations.

The size of the largest chunk The largest chunk size generated by fracture fluidisation inside outlet channel is measured using a clustering algorithm. The particles that are bounded by attraction forces are grouped and recognised as a

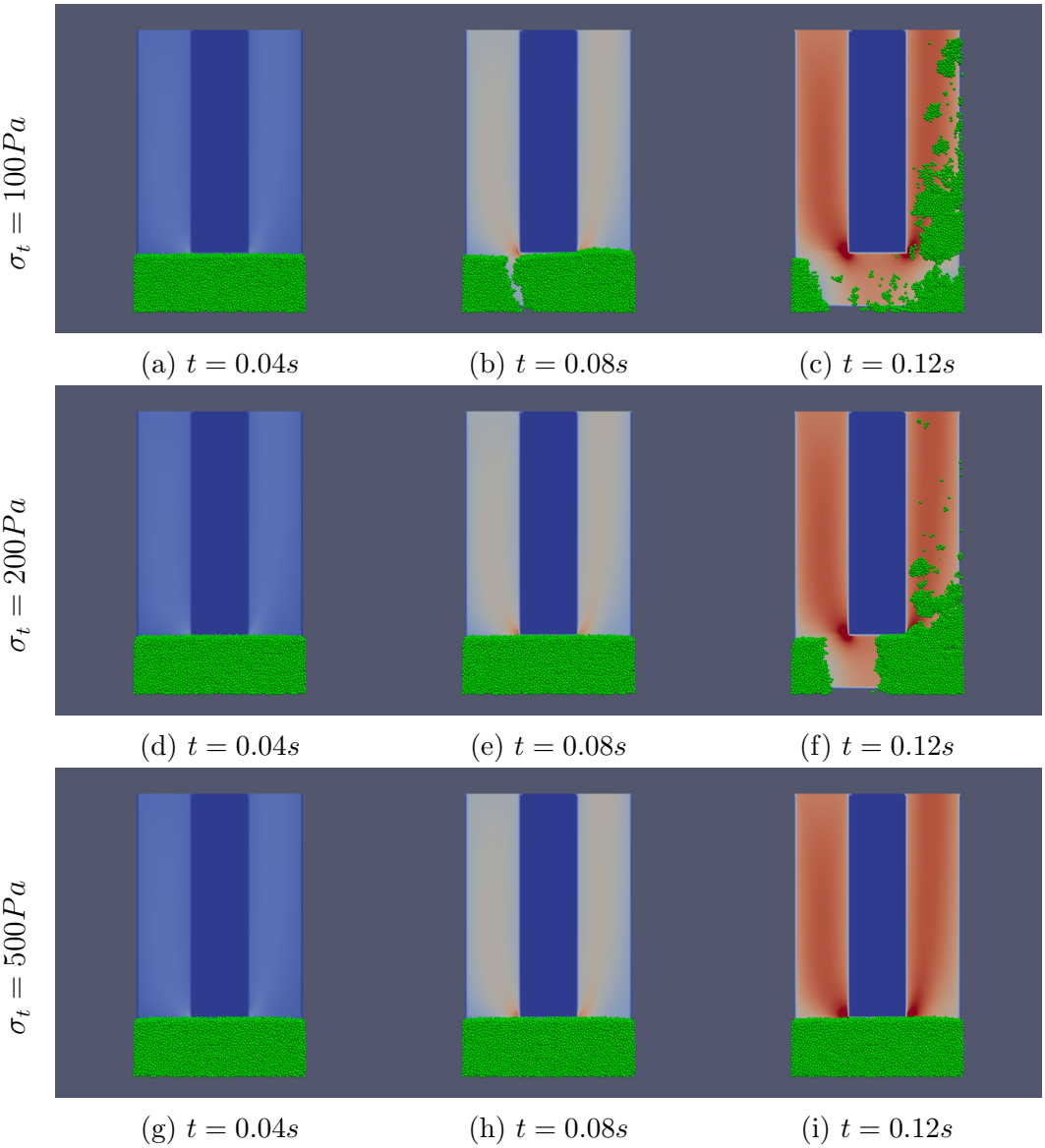

(a) $t = 0.04s$ (b) $t = 0.08s$ (c) $t = 0.12s$

(d) $t = 0.04s$ (e) $t = 0.08s$ (f) $t = 0.12s$

(g) $t = 0.04s$ (h) $t = 0.08s$ (i) $t = 0.12s$

Figure 5.9: Simulations of fracture fluidisations for powder bed of volume fraction $\phi = 0.48$ with different tensile strength.

single chunk. The size of the largest chunk generated by powder bed is measured as a function of ϕ and σ_t. The result is illustrated in Figure 5.11 as a heat map. The range of σ_t and ϕ explored are $50 - 500Pa$ and $0.3 - 0.5$ respectively.

From the heat map it is evident that there is a threshold in σ_t beyond which the fracture does not occur and no powder chunk will exit the channel. This threshold

is lower for higher ϕ. The highest chunk size is usually achieved by loosely packed powder bed with moderate tensile strength (when $\phi \approx 0.3$ and $\sigma_t = 250 - 350Pa$). The largest chunk size from all the simulations is approximately around $3mm^3$ regardless of the tensile strength and volume fraction.

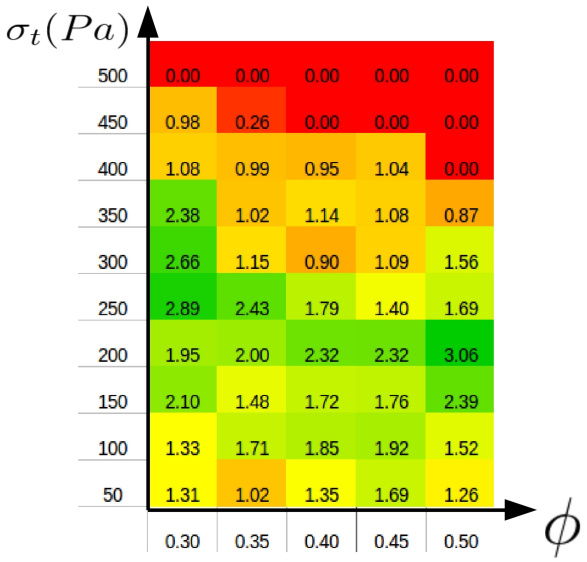

Figure 5.11: Heat map of the size of largest chunk generated with powder bed of different ϕ and σ_t. The size of the chunk is in unit of mm^3 and the volume accounts for space occupied by powder particles only (excluding the void space inside the chunk).

Intuitively one would expect the chunk size to increase with the tensile strength. It is true when σ_t is in range of $50 - 200Pa$. In this range of tensile strength, the powder is easier to be fragmented if the cohesion is weak and hence the resulting chunk size is small. Upon further increasing tensile strength, the cohesion of particle-particle and particle-wall becomes so strong that the bulk of the powder bed is stuck at the bottom channel. Only few smaller chunks can break from bulk

powder through vertical fracture at outlet channel. If the tensile strength is further increased, the powder behaves much more like a solid and no fracture can be initiated under the prescribed air flow.

Distribution of the sizes of powder chunks The distribution of the size of powder chunks shows clear dependence on the tensile strength for $\sigma_t = 100Pa - 300Pa$ but is quite independent of the volume fraction. The probability of finding the powder chunk within a certain size range for different volume fraction is shown in Figure 5.12. There is a clear trend of change of probability distribution by increasing the tensile strength. As the tensile strength increases, there will be less small size chunks in range of $0 - 0.1mm^3$ and more chunks of larger sizes.

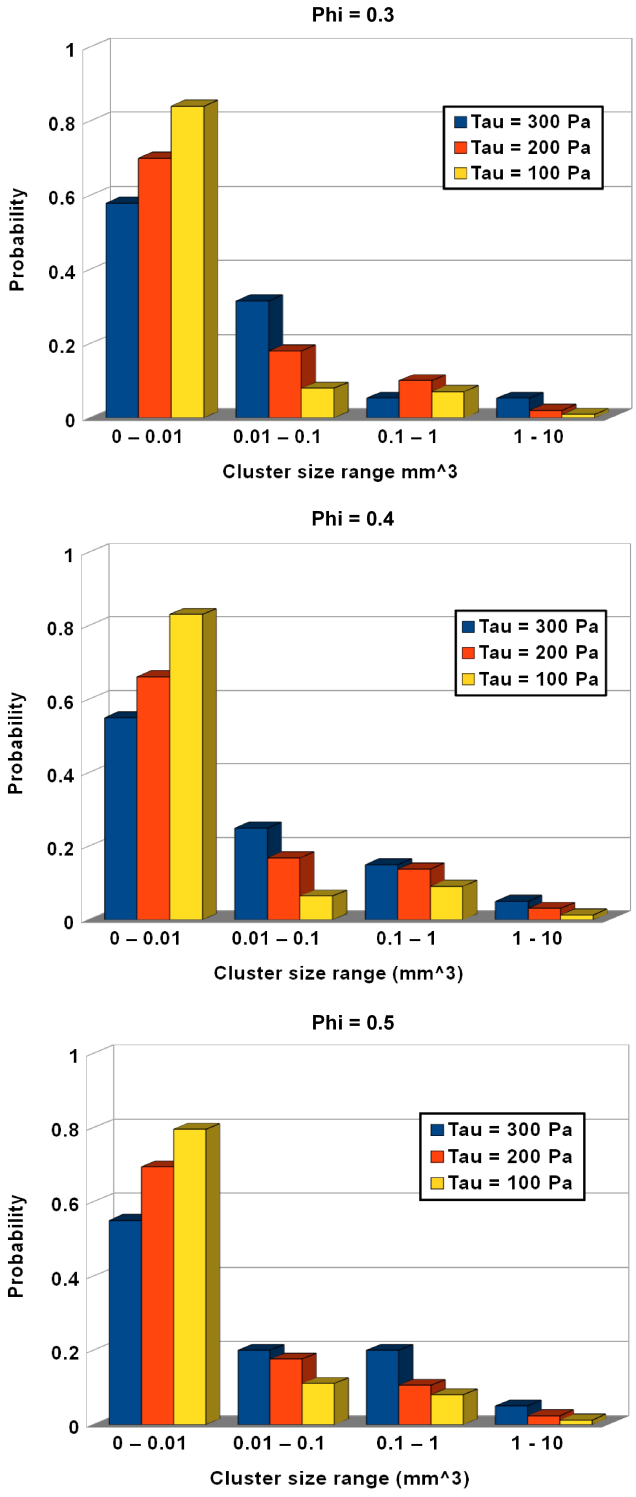

Figure 5.12: Probability of finding powder chunks within different size ranges for $\phi = 0.3$, $\phi = 0.4$ and $\phi = 0.5$.

From Figure 5.12 we would like to postulate that the sizes of chunks generated by fracture fluidisation should follow an exponential distribution. The probability density function with basis in logarithmic form can be written as

$$f(D;\lambda) = \lambda \exp(-\lambda \log \frac{D}{D_{min}}) \tag{5.13}$$

where D_{min} is the size of the elementary particle which sets the lower bound for the size of the powder chunks. The parameter λ should be inversely proportional to the tensile strength σ_t. The distribution function is plotted with $\log \frac{D}{D_{min}}$ as basis for different λ in Figure 5.13. There should also be an upper bound for the size of powder chunks since they can not exceed the size of the channel. As a result, the probability density value for $D > D_{min}$ should be kept as close to 0 as possible. It is better not to truncate the PDF for $D > D_{min}$ since the integral of the PDF will be less than 1.

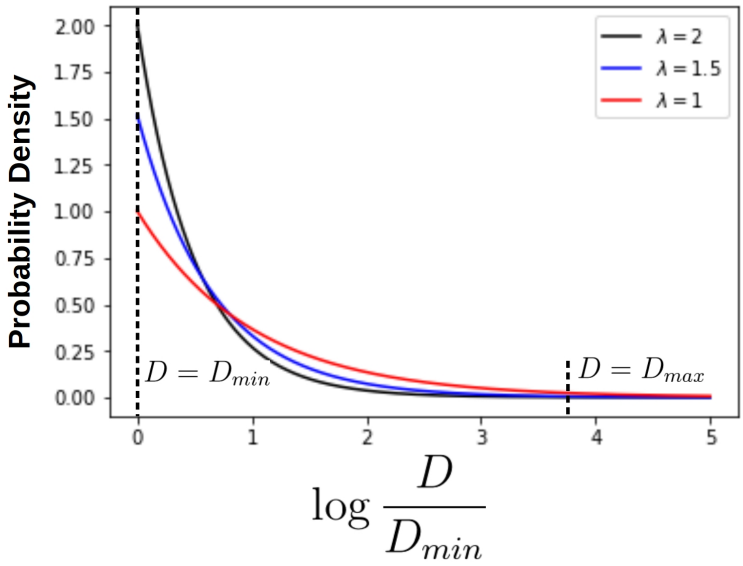

Figure 5.13: The size distribution of powder chunks can be best described by an exponential distribution.

5.5 Conclusion

More information on the material of the channel wall is needed, as it is essential for modelling the particle-wall interaction accurately.

Our current simulation using cohesive discrete particle dynamics is only applicable for studying the initialisation of the fracture fluidisation. The prescribed air velocity field is the result of simulation of air flow passing through a stationary powder bed in OpenFoam. To capture the accurate fluidisation behaviour after initial break-up of powder bed, a two-way coupled cohesive particles dynamics simulation is highly recommended.

Only monodispersed particles are used in current simulations. In reality the powder is highly polydispersed, the size of the chunks can be much more smaller than the elementary particle used in simulations.

Chapter 6

Conclusions and Future Work

The main outputs of the Ph.D project are two: the development of the FIPI and the investigations of the behaviours of the particle-covered drops under gravity and isotropic compression. In the current chapter, the results and achievements are reviewed and discussed, directions for future work and improvements are also given at the end.

6.1 Conclusions

The development of FIPI method is motivated by the demand for a fast numerical formulation that can enable fast simulations of fluid interfaces covered with a large number of particles.

One of the most important contributions made during the development of FIPI is that the capillary interactions between particles and fluid interfaces are modelled by spring forces. Physically this force depends on the moving contact line and the dynamic contact angle that are hard to resolve numerically. This spring force model

avoids the necessity of the information of the unresolved features and makes the interactions solely depend on the distances from particle centres to fluid interfaces. The distances can be calculated locally at particle centres without resorting to complex algorithms thanks to the adoption of phase field method.

FIPI method has demonstrated its capability to capture the influences of absorbed solid particles on the mechanical properties of fluid interfaces. The results of the simulations done so far have justified the adoption of the point-force modelling strategy. With pairwise interactions between articles, it is possible to modulate the surface tension of the particle-laden fluid interface. It is the first numerical formulation that can be used to simulate collective behaviour of particle-laden fluid interfaces without resolving particle scale features.

The numerical studies with FIPI comprise the investigations of two physical problems related to the drops covered with a monolayer of particles.

In the first numerical experiment, the simulations of a pendant drop covered with a monolayer of repulsive spherical particles have been performed for different surface coverages, interaction ranges and interaction strengths. The studies have demonstrated the advantage of FIPI: the stress distribution on the fluid interface can be calculated for interfaces with complex morphologies, provided that there are enough particles around the location of interest.

The surface stress was calculated by local area averaging, using a formula that is analogous to the Irving-Kirkwood formula of molecular dynamics. Reasonably good agreement was found between the predictions for the surface pressure given by this formula and the surface tension reduction calculated by measuring the drop curvature at two points and fitting to a solution of the Young-Laplace equation (method of Fordham, [166]).

Simulations in which the particles are represented as discrete elements are exceedingly useful when interfacial constitutive equations are not available. This is the case when the interfacial suspensions is polydispersed, or particle adsorption changes the surface tension on a time scale comparable to that of the drop deformation. Also in experiments it is not always possible to access the details related to the local particle arrangements. The new numerical formulation presented in this thesis is ideally suited to studying these and other phenomena, for instance monolayer fracture and dislocation dynamics.

Anisotropic stress is found for drops covered with particles having short-range interactions at high surface fraction. The anisotropic effects are most evident in the neck region of the drop. The monolayer microstructure in the neck region deviates significantly from a hexagonal packing, indicating that the drop surface sustains a higher stress along the azimuthal direction than meridional direction. The presence of the anisotropic stress shows that the fluid interface now has finite shear elasticity. The result of the investigation of anisotropic surface stress has demonstrated that drop deformation, particle arrangement and the resulting change in surface stress are highly coupled.

The emergence of accurate simulation of particles adhered to geometrically complex and time-dependent interface morphologies opens new research opportunities in areas such as interfacial rheology, microfluidic generation of drops and bubbles with structured interfaces, and production of anisotropic Pickering emulsions. By giving insights into the local microstructure/surface stress relation, the FIPI method could help in the analysis of pendant drop experiments. For instance, the simulated shape of the drop can be fitted to the experimental shape by tuning the inter-particle pair potential to obtain information on colloidal interactions at interfaces. While results for curved surfaces are more difficult to interpret than

those obtained on a planar surface, they are also more realistic, as they account for the coupling between particle distribution and interface shape.

In a second numerical experiment, simulations have been performed to investigate the outcomes of a spherical drop covered with particles when the drop is under compression from the particle monolayer.

Characteristics of a drop having zero surface tension has been studied. In the absence of bending rigidity of the monolayer, the drop can buckle as long as the surface pressure of the particle monolayer is larger than the surface tension of the bare fluid interface. The speed of buckling is proportional to the surface overpressure $\Pi_s - \gamma$.

However, the surface pressure of the monolayer can not always surpass the surface tension of the fluid interface. When the adsorption of particles on fluid interfaces is weak, the particle monolayer can presents small-scale undulations which greatly amplifies the normal forces exerted on the particles and increases the probability of particle desorption.

A large number of small-wavelength undulations of particle monolayer can produce a significant increase in surface area without the drop surface deviating significantly from a sphere. Detecting monolayer wrinkling experimentally can thus be challenging, as the drop or bubble presenting small-scale wrinkling will look macroscopically spherical. This is a major discovery from the current studies done by numerical simulations using FIPI: small-scale surface roughness can be created in addition to the global curvature of the fluid interface and will have impact on the integrity of particle monolayers on fluid interface.

Another important contribution of the current work is the exploration of cur-

vature effects. It is found that relatively large values of a/R favour small-scale monolayer undulations, which in turn induces desorption when the surface pressure increases further. Small values of a/R tend to give pure buckling. This result is in qualitative agreement with the observations accompanying figure 1.6.

6.2 Future Work

There are several potential improvements of FIPI. First, the undisturbed fluid velocity in Equation (2.12) could be better modelled to approximately include global undisturbed flow velocity and disturbance flows from other particles. The difficulty lies in the fact that the fluid velocity interpolated at the location of a particle contains also the disturbance caused by the particle itself, and it is not trivial to subtract this unwanted disturbance. The Stokeslet can be used to do the job in single phase Stokes flows but is no more valid when fluid interfaces are present. As an example shown in Figure 6.1, the flow streamlines caused by a particle moving across a fluid interface is not symmetric with respect to the horizontal passing through the particle centre.

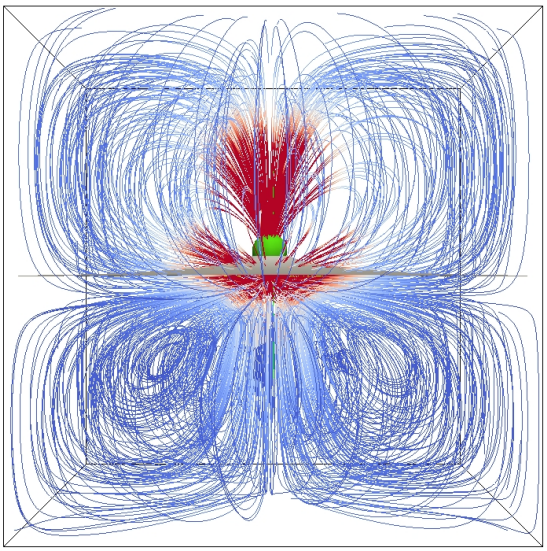

Figure 6.1: The streamlines of flow field caused by a particle moving across a fluid interface. The disturbance field is definitely not symmetric with respect to the fluid interface.

At the moment, it is feasible to take the flow velocity interpolated at the location of a particle as the undisturbed flow velocity seen by that particle. It requires particle sizes to be significantly smaller than the grid sizes, or forces from particles to be negligibly small compared to other forces acting on the flow. This approach is common in the simulations of single phase particle-laden turbulent flows [202, 203]. However, this greatly reduces the versatility of FIPI since the particles must be much smaller than any relevant interfacial features.

A possible approach to tackle this problem is to implement a numerical scheme similar to the force coupling method (FCM). In FCM, the velocities of particles are updated by interpolation through a properly fitted kernel only instead of solving Newton's equation of motion. The conventional FCM scheme has to be reevaluated for flow containing fluid interfaces.

Secondly, more accurate hydrodynamic drag models could be implemented.

The currently employed Stokes drag model is only strictly appropriate when the particle suspension is dilute, which is not the case when the solid particles are packed closely on the fluid interface. A possible improvement of the method would be to make the hydrodynamic drag force on each particle a function of the local solid volume fraction.

In a similar principle, the attachment force between each solid particle and the fluid interface could also be a function of local solid surface coverage. The force holding a particle in a densely packed monolayer might be different from the force estimated by the adsorption energy of a single particle, since the neighbouring area of the particle on the interface is occupied mostly by solid instead of fluid. In the current implementation of FIPI this effect is assumed to be small.

Thirdly, depending on the specific physics, different particle-particle interaction models could be adopted. For solid-solid contacts between particles, Hertzian model would be a more appropriate choice and the parameters of the model must be adjusted to reflect the correct elasticity of the particle materials. For colloidal particles in ionic liquids, an interaction model adhering to DLVO theory might give more realistic simulation results. Different particle-particle interaction models could result in different monolayer packing geometries, giving different mechanical properties of the monolayers [42].

From the perspective of the physics of particle-laden interfaces, it is interesting to use FIPI in the future to explore additional factors that have great influences on the arrangement of particle monolayer, some of them are already mentioned such as polydispersity in particle size, differences in contact angle, the presence of inter-particle adhesion or the effect of gravity.

With FIPI some initial numerical experiments are carried out introducing inter-

particle attraction and tangential inter-particle forces in addition to short range repulsion, to mimic cohesive particle layers. These initial tests reveal that the system's behaviour is much more complex than for pure repulsion, because with attractive interactions the surface stress can become non-uniform even when the fluid interface is spherical or flat. This features makes the theoretical analysis of the problem extremely challenging.

The difference in contact angle can also increase the complexity of particle monolayers on fluid interface. As monolayers will manifest small-scale undulations described in chapter 4 even without compression. The capability of exploring the behaviours of monolayers composed of more realistic particles will be the focus of the development of FIPI in the future.

References

[1] Yves Chevalier and Marie-Alexandrine Bolzinger. Emulsions stabilized with solid nanoparticles: Pickering emulsions. *Colloids and Surfaces A: Physicochemical and Engineering Aspects*, 439:23–34, 2013.

[2] AD Dinsmore, Ming F Hsu, MG Nikolaides, Manuel Marquez, AR Bausch, and DA Weitz. Colloidosomes: selectively permeable capsules composed of colloidal particles. *Science*, 298(5595):1006–1009, 2002.

[3] EM Herzig, KA White, AB Schofield, WCK Poon, and PS Clegg. Bicontinuous emulsions stabilized solely by colloidal particles. *Nature materials*, 6(12):966–971, 2007.

[4] Vincent Poulichet and Valeria Garbin. Cooling particle-coated bubbles: destabilization beyond dissolution arrest. *Langmuir*, 31(44):12035–12042, 2015.

[5] Rammile Ettelaie and Sergey V Lishchuk. Detachment force of particles from fluid droplets. *Soft Matter*, 11(21):4251–4265, 2015.

[6] Eric Dickinson. Food emulsions and foams: stabilization by particles. *Current Opinion in Colloid & Interface Science*, 15(1):40–49, 2010.

[7] Pierre-Gilles De Gennes, Françoise Brochard-Wyart, and David Quéré. *Capillarity and wetting phenomena: drops, bubbles, pearls, waves*. Springer Science & Business Media, 2013.

[8] Bernard P Binks. Particles as surfactants-similarities and differences. *Current Opinion in Colloid & Interface Science*, 7(1):21–41, 2002.

[9] Valeria Garbin, John C Crocker, and Kathleen J Stebe. Nanoparticles at fluid interfaces: Exploiting capping ligands to control adsorption, stability and dynamics. *Journal of colloid and interface science*, 387(1):1–11, 2012.

[10] Bernard P Binks and Tommy S Horozov. *Colloidal particles at liquid interfaces*. Cambridge University Press, 2006.

[11] BP Binks and SO Lumsdon. Pickering emulsions stabilized by monodisperse latex particles: effects of particle size. *Langmuir*, 17(15):4540–4547, 2001.

[12] Bernard P Binks and Anaïs Rocher. Effects of temperature on water-in-oil emulsions stabilised solely by wax microparticles. *Journal of colloid and interface science*, 335(1):94–104, 2009.

[13] Robert Aveyard, Bernard P Binks, and John H Clint. Emulsions stabilised solely by colloidal particles. *Advances in Colloid and Interface Science*, 100:503–546, 2003.

[14] Heng Fan and Alberto Striolo. Mechanistic study of droplets coalescence in Pickering emulsions. *Soft Matter*, 8(37):9533–9538, 2012.

[15] Sonia Melle, Mauricio Lask, and Gerald G Fuller. Pickering emulsions with controllable stability. *Langmuir*, 21(6):2158–2162, 2005.

[16] KV Edmond, AB Schofield, Manuel Marquez, JP Rothstein, and AD Dins-

more. Stable jets of viscoelastic fluids and self-assembled cylindrical capsules by hydrodynamic focusing. *Langmuir*, 22(21):9052–9056, 2006.

[17] Molly K Mulligan and Jonathan P Rothstein. Deformation and breakup of micro-and nanoparticle stabilized droplets in microfluidic extensional flows. *Langmuir*, 27(16):9760–9768, 2011.

[18] Anthony P Kotula and Shelley L Anna. Probing timescales for colloidal particle adsorption using slug bubbles in rectangular microchannels. *Soft Matter*, 8(41):10759–10772, 2012.

[19] Ghislain Bournival, Seher Ata, and Erica J Wanless. The roles of particles in multiphase processes: Particles on bubble surfaces. *Advances in colloid and interface science*, 2015.

[20] Pietro Cicuta, Edward J Stancik, and Gerald G Fuller. Shearing or compressing a soft glass in 2D: time-concentration superposition. *Physical review letters*, 90(23):236101, 2003.

[21] Joe W Tavacoli, Job HJ Thijssen, Andrew B Schofield, and Paul S Clegg. Bijel Capsules: Novel, Robust, and Versatile Bijels of Nitromethane, Ethanediol, and Colloidal Silica: Capsules, Sub-Ten-Micrometer Domains, and Mechanical Properties . *Advanced Functional Materials*, 21(11):1949–1949, 2011.

[22] Jun-Yee Leong, Beng-Ti Tey, Chin-Ping Tan, and Eng-Seng Chan. Nozzleless Fabrication of Oil-Core Biopolymeric Microcapsules by the Interfacial Gelation of Pickering Emulsion Templates. *ACS applied materials & interfaces*, 7(30):16169–16176, 2015.

[23] Kevin Stratford, Ronojoy Adhikari, Ignacio Pagonabarraga, J-C Desplat, and Michael E Cates. Colloidal jamming at interfaces: A route to fluid-bicontinuous gels. *Science*, 309(5744):2198–2201, 2005.

[24] Michael E Cates and Paul S Clegg. Bijels: a new class of soft materials.

Soft Matter, 4(11):2132–2138, 2008.

[25] Bernard P Binks and SO Lumsdon. Influence of particle wettability on the type and stability of surfactant-free emulsions. *Langmuir*, 16(23):8622–8631, 2000.

[26] GK Batchelor. The effect of brownian motion on the bulk stress in a suspension of spherical particles. *Journal of fluid mechanics*, 83(1):97–117, 1977.

[27] Zhiping Du, Maria P Bilbao-Montoya, Bernard P Binks, Eric Dickinson, Rammile Ettelaie, and Brent S Murray. Outstanding stability of particle-stabilized bubbles. *Langmuir*, 19(8):3106–3108, 2003.

[28] Stig E Friberg. Foams from non-aqueous systems. *Current Opinion in Colloid & Interface Science*, 15(5):359–364, 2010.

[29] Eunhye Kim, Kevin Stratford, and Michael E Cates. Bijels containing magnetic particles: A simulation study. *Langmuir*, 26(11):7928–7936, 2010.

[30] Pascale Aussillous and David Quéré. Liquid marbles. *Nature*, 411(6840):924–927, 2001.

[31] P McEleney, GM Walker, IA Larmour, and SEJ Bell. Liquid marble formation using hydrophobic powders. *Chemical Engineering Journal*, 147(2-3):373–382, 2009.

[32] David E Tambe and Mukul M Sharma. The effect of colloidal particles on fluid-fluid interfacial properties and emulsion stability. *Advances in colloid and interface science*, 52:1–63, 1994.

[33] Lorenzo Botto, Eric P Lewandowski, Marcello Cavallaro, and Kathleen J Stebe. Capillary interactions between anisotropic particles. *Soft Matter*, 8(39):9957–9971, 2012.

[34] Anand Bala Subramaniam, Manouk Abkarian, L Mahadevan, and Howard A Stone. Mechanics of interfacial composite materials. *Langmuir*, 22(24):10204–

10208, 2006.

[35] Cécile Monteux, John Kirkwood, Hui Xu, Eric Jung, and Gerald G Fuller. Determining the mechanical response of particle-laden fluid interfaces using surface pressure isotherms and bulk pressure measurements of droplets. *Physical Chemistry Chemical Physics*, 9(48):6344–6350, 2007.

[36] Alma J Mendoza, Eduardo Guzmán, Fernando Martínez-Pedrero, Hernán Ritacco, Ramón G Rubio, Francisco Ortega, Victor M Starov, and Reinhard Miller. Particle laden fluid interfaces: Dynamics and interfacial rheology. *Advances in colloid and interface science*, 206:303–319, 2014.

[37] SV Lishchuk and I Halliday. Effective surface viscosities of a particle-laden fluid interface. *Physical Review E*, 80(1):016306, 2009.

[38] Anand Bala Subramaniam, Manouk Abkarian, L Mahadevan, and Howard A Stone. Colloid science: Non-spherical bubbles. *Nature*, 438(7070):930–930, 2005.

[39] Peter Fischer and Philipp Erni. Emulsion drops in external flow fields - the role of liquid interfaces. *Current Opinion in Colloid & Interface Science*, 12(4):196–205, 2007.

[40] Krassimir D Danov, Rumyana D Stanimirova, Peter A Kralchevsky, Krastanka G Marinova, Nikola A Alexandrov, Simeon D Stoyanov, Theodorus BJ Blijdenstein, and Eddie G Pelan. Capillary meniscus dynamometry–method for determining the surface tension of drops and bubbles with isotropic and anisotropic surface stress distributions. *Journal of colloid and interface science*, 440:168–178, 2015.

[41] Alan M Luo, Leonard MC Sagis, Hans Christian Öttinger, Cristiano De Michele, and Patrick Ilg. Modelling the rheology of anisotropic particles adsorbed on a two-dimensional fluid interface. *Soft matter*, 11(22):4383–4395, 2015.

[42] Dominic Vella, Pascale Aussillous, and L Mahadevan. Elasticity of an inter-

facial particle raft. *EPL (Europhysics Letters)*, 68(2):212, 2004.

[43] Eric Dickinson. Computer simulation of particle gel formation. *Journal of the Chemical Society, Faraday Transactions*, 90(1):173–180, 1994.

[44] Robert Aveyard, John H Clint, Dieter Nees, and Vesselin N Paunov. Compression and structure of monolayers of charged latex particles at air/water and octane/water interfaces. *Langmuir*, 16(4):1969–1979, 2000.

[45] William TM Irvine, Vincenzo Vitelli, and Paul M Chaikin. Pleats in crystals on curved surfaces. *Nature*, 468(7326):947–951, 2010.

[46] William TM Irvine and Vincenzo Vitelli. Geometric background charge: dislocations on capillary bridges. *Soft Matter*, 8(39):10123–10129, 2012.

[47] Vinothan N Manoharan. Colloidal matter: Packing, geometry, and entropy. *Science*, 349(6251):1253751, 2015.

[48] Donald Allen Drew. Mathematical modeling of two-phase flow. *Annual review of fluid mechanics*, 15(1):261–291, 1983.

[49] T Bo Anderson and Roy Jackson. Fluid mechanical description of fluidized beds. Equations of motion. *Industrial & Engineering Chemistry Fundamentals*, 6(4):527–539, 1967.

[50] R Jackson. Locally averaged equations of motion for a mixture of identical spherical particles and a Newtonian fluid. *Chemical Engineering Science*, 52(15):2457–2469, 1997.

[51] Prabhu R Nott, Elisabeth Guazzelli, and Olivier Pouliquen. The suspension balance model revisited. *Physics of Fluids (1994-present)*, 23(4):043304, 2011.

[52] Arthur R Deemer and John C Slattery. Balance equations and structural models for phase interfaces. *International Journal of Multiphase Flow*, 4(2):171–192, 1978.

[53] WG Gray and SM Hassanizadeh. Averaging theorems and averaged equa-

tions for transport of interface properties in multiphase systems. *International Journal of Multiphase Flow*, 15(1):81–95, 1989.

[54] Gretchen M Mavrovouniotis and Howard Brenner. A micromechanical investigation of interfacial transport processes. I. Interfacial conservation equations. *Philosophical Transactions of the Royal Society of London A: Mathematical, Physical and Engineering Sciences*, 345(1675):165–207, 1993.

[55] Valeria Garbin, John C Crocker, and Kathleen J Stebe. Forced desorption of nanoparticles from an oil–water interface. *Langmuir*, 28(3):1663–1667, 2011.

[56] Vincent Poulichet and Valeria Garbin. Ultrafast desorption of colloidal particles from fluid interfaces. *Proceedings of the National Academy of Sciences*, 112(19):5932–5937, 2015.

[57] Anand Bala Subramaniam, Cecile Mejean, Manouk Abkarian, and Howard A. Stone. Microstructure, morphology, and lifetime of armored bubbles exposed to surfactants. *Langmuir*, 22(14):5986–5990, 2006.

[58] A Vidal and L Botto. Slip flow past a gas–liquid interface with embedded solid particles. *Journal of Fluid Mechanics*, 813:152–174, 2017.

[59] Francois Xavier Sicard and Alberto Striolo. Buckling in armored droplets. *Nanoscale*, 2017.

[60] Sepideh Razavi, Kathleen D Cao, Binhua Lin, Ka Yee C Lee, Raymond S Tu, and Ilona Kretzschmar. Collapse of particle-laden interfaces under compression: buckling vs particle expulsion. *Langmuir*, 31(28):7764–7775, 2015.

[61] MG Basavaraj, GG Fuller, Jan Fransaer, and Jan Vermant. Packing, flipping, and buckling transitions in compressed monolayers of ellipsoidal latex particles. *Langmuir*, 22(15):6605–6612, 2006.

[62] Tommy S Horozov, Bernard P Binks, Robert Aveyard, and John H Clint. Effect of particle hydrophobicity on the formation and collapse of fumed

silica particle monolayers at the oil–water interface. *Colloids and Surfaces A: Physicochemical and Engineering Aspects*, 282:377–386, 2006.

[63] NID Fenwick, F Bresme, and N Quirke. Computer simulation of a Langmuir trough experiment carried out on a nanoparticulate array. *The Journal of Chemical Physics*, 114(16):7274–7282, 2001.

[64] N Tsapis, ER Dufresne, SS Sinha, CS Riera, JW Hutchinson, L Mahadevan, and DA Weitz. Onset of buckling in drying droplets of colloidal suspensions. *Physical review letters*, 94(1):018302, 2005.

[65] Sujit S Datta, Ho Cheung Shum, and David A Weitz. Controlled buckling and crumpling of nanoparticle-coated droplets. *Langmuir*, 26(24):18612–18616, 2010.

[66] Sándor Bordács, Attila Agod, and Zoltán Hórvölgyi. Compression of langmuir films composed of fine particles: collapse mechanism and wettability. *Langmuir*, 22(16):6944–6950, 2006.

[67] Hui Xu, Sonia Melle, Konstantin Golemanov, and Gerald Fuller. Shape and buckling transitions in solid-stabilized drops. *Langmuir*, 21(22):10016–10020, 2005.

[68] Sebastian Knoche, Dominic Vella, Elodie Aumaitre, Patrick Degen, Heinz Rehage, Pietro Cicuta, and Jan Kierfeld. Elastometry of deflated capsules: Elastic moduli from shape and wrinkle analysis. *Langmuir*, 29(40):12463–12471, 2013.

[69] Vincent Poulichet, Axel Huerre, and Valeria Garbin. Shape oscillations of particle-coated bubbles and directional particle expulsion. *Soft matter*, 13(1):125–133, 2017.

[70] Ruben Scardovelli and Stéphane Zaleski. Direct numerical simulation of free-surface and interfacial flow. *Annual review of fluid mechanics*, 31(1):567–603, 1999.

[71] Francis H Harlow and J Eddie Welch. Numerical calculation of time-dependent viscous incompressible flow of fluid with free surface. *The physics of fluids*, 8(12):2182–2189, 1965.

[72] Murilo F Tome and Sean McKee. Gensmac: A computational marker and cell method for free surface flows in general domains. *Journal of Computational Physics*, 110(1):171–186, 1994.

[73] Cyril W Hirt and Billy D Nichols. Volume of fluid (vof) method for the dynamics of free boundaries. *Journal of computational physics*, 39(1):201–225, 1981.

[74] Denis Gueyffier, Jie Li, Ali Nadim, Ruben Scardovelli, and Stéphane Zaleski. Volume-of-fluid interface tracking with smoothed surface stress methods for three-dimensional flows. *Journal of Computational physics*, 152(2):423–456, 1999.

[75] Nasser Ashgriz and JY Poo. Flair: Flux line-segment model for advection and interface reconstruction. *Journal of computational physics*, 93(2):449–468, 1991.

[76] William J Rider and Douglas B Kothe. Reconstructing volume tracking. *Journal of computational physics*, 141(2):112–152, 1998.

[77] Yuriko Renardy and Michael Renardy. Prost: a parabolic reconstruction of surface tension for the volume-of-fluid method. *Journal of computational physics*, 183(2):400–421, 2002.

[78] Salih Ozen Unverdi and Grétar Tryggvason. A front-tracking method for viscous, incompressible, multi-fluid flows. *Journal of computational physics*, 100(1):25–37, 1992.

[79] Grétar Tryggvason, Bernard Bunner, Asghar Esmaeeli, Damir Juric, N Al-Rawahi, W Tauber, J Han, S Nas, and Y-J Jan. A front-tracking method for the computations of multiphase flow. *Journal of Computational Physics*,

169(2):708–759, 2001.

[80] Stéphane Popinet and Stéphane Zaleski. A front-tracking algorithm for accurate representation of surface tension. *International Journal for Numerical Methods in Fluids*, 30(6):775–793, 1999.

[81] Mark Sussman, Peter Smereka, and Stanley Osher. A level set approach for computing solutions to incompressible two-phase flow. *Journal of Computational physics*, 114(1):146–159, 1994.

[82] Stanley Osher and Ronald P Fedkiw. Level set methods: an overview and some recent results. *Journal of Computational physics*, 169(2):463–502, 2001.

[83] Douglas Enright, Ronald Fedkiw, Joel Ferziger, and Ian Mitchell. A hybrid particle level set method for improved interface capturing. *Journal of Computational physics*, 183(1):83–116, 2002.

[84] Daniel M Anderson, Geoffrey B McFadden, and Adam A Wheeler. Diffuse-interface methods in fluid mechanics. *Annual review of fluid mechanics*, 30:139–165, 1998.

[85] David Jacqmin. Calculation of two-phase navier–stokes flows using phase-field modeling. *Journal of Computational Physics*, 155(1):96–127, 1999.

[86] Pengtao Yue, James J Feng, Chun Liu, and Jie Shen. A diffuse-interface method for simulating two-phase flows of complex fluids. *Journal of Fluid Mechanics*, 515:293–317, 2004.

[87] V.E. Badalassi, H.D. Ceniceros, and S. Banerjee. Computation of multiphase systems with phase field models. *Journal of Computational Physics*, 190(2):371 – 397, 2003.

[88] Shiyi Chen and Gary D Doolen. Lattice boltzmann method for fluid flows. *Annual review of fluid mechanics*, 30(1):329–364, 1998.

[89] Xiaowen Shan and Hudong Chen. Lattice boltzmann model for simulating flows with multiple phases and components. *Physical Review E*, 47(3):1815,

1993.

[90] Michael R Swift, E Orlandini, WR Osborn, and JM Yeomans. Lattice boltzmann simulations of liquid-gas and binary fluid systems. *Physical Review E*, 54(5):5041, 1996.

[91] Howard H Hu, Neelesh A Patankar, and MY Zhu. Direct numerical simulations of fluid–solid systems using the arbitrary lagrangian–eulerian technique. *Journal of Computational Physics*, 169(2):427–462, 2001.

[92] Jungwoo Kim, Dongjoo Kim, and Haecheon Choi. An immersed-boundary finite-volume method for simulations of flow in complex geometries. *Journal of Computational Physics*, 171(1):132–150, 2001.

[93] Markus Uhlmann. An immersed boundary method with direct forcing for the simulation of particulate flows. *Journal of Computational Physics*, 209(2):448–476, 2005.

[94] Rajat Mittal and Gianluca Iaccarino. Immersed boundary methods. *Annu. Rev. Fluid Mech.*, 37:239–261, 2005.

[95] Charles S Peskin. The fluid dynamics of heart valves: experimental, theoretical, and computational methods. *Annual review of fluid mechanics*, 14(1):235–259, 1982.

[96] EA Fadlun, R Verzicco, P_ Orlandi, and J Mohd-Yusof. Combined immersed-boundary finite-difference methods for three-dimensional complex flow simulations. *Journal of computational physics*, 161(1):35–60, 2000.

[97] D Goldstein, R Handler, and L Sirovich. Modeling a no-slip flow boundary with an external force field. *Journal of Computational Physics*, 105(2):354–366, 1993.

[98] Roland Glowinski, T-W Pan, Todd I Hesla, and Daniel D Joseph. A distributed lagrange multiplier/fictitious domain method for particulate flows. *International Journal of Multiphase Flow*, 25(5):755–794, 1999.

[99] Neelesh A Patankar, Pushpendra Singh, Daniel D Joseph, Roland Glowinski, and T-W Pan. A new formulation of the distributed lagrange multiplier/fictitious domain method for particulate flows. *International Journal of Multiphase Flow*, 26(9):1509–1524, 2000.

[100] Frank Baaijens. A fictitious domain/mortar element method for fluid–structure interaction. *International Journal for Numerical Methods in Fluids*, 35(7):743–761, 2001.

[101] S Elghobashi. On predicting particle-laden turbulent flows. *Applied scientific research*, 52(4):309–329, 1994.

[102] Qunzhen Wang and Kyle D Squires. Large eddy simulation of particle-laden turbulent channel flow. *Physics of Fluids*, 8(5):1207–1223, 1996.

[103] Antonino Ferrante and Said Elghobashi. On the physical mechanisms of two-way coupling in particle-laden isotropic turbulence. *Physics of fluids*, 15(2):315–329, 2003.

[104] Yasufumi Yamamoto, Matthias Potthoff, Toshitsugu Tanaka, Tsui Kajishima, and Yutaka Tsuji. Large-eddy simulation of turbulent gas–particle flow in a vertical channel: effect of considering inter-particle collisions. *Journal of Fluid Mechanics*, 442:303–334, 2001.

[105] Kyle D Squires and John K Eaton. Preferential concentration of particles by turbulence. *Physics of Fluids A: Fluid Dynamics*, 3(5):1169–1178, 1991.

[106] Tristan M Burton and John K Eaton. Fully resolved simulations of particle-turbulence interaction. *Journal of Fluid Mechanics*, 545:67–111, 2005.

[107] Yiming Li, John B McLaughlin, K Kontomaris, and L Portela. Numerical simulation of particle-laden turbulent channel flow. *Physics of Fluids*, 13(10):2957–2967, 2001.

[108] S Elghobashi. Particle-laden turbulent flows: direct simulation and closure models. *Applied Scientific Research*, 48(3-4):301–314, 1991.

[109] J F Brady and G Bossis. Stokesian dynamics. *Annual Review of Fluid Mechanics*, 20(1):111–157, 1988.

[110] Sangtae Kim and Seppo J Karrila. *Microhydrodynamics: principles and selected applications*. 2005.

[111] Bloen Metzger, Maxime Nicolas, and Élisabeth Guazzelli. Falling clouds of particles in viscous fluids. *Journal of Fluid Mechanics*, 580:283–301, 2007.

[112] ML Ekiel-Jeżewska, B Metzger, and E Guazzelli. Spherical cloud of point particles falling in a viscous fluid. *Physics of Fluids*, 18(3):038104, 2006.

[113] Florian Günther, Florian Janoschek, Stefan Frijters, and Jens Harting. Lattice Boltzmann simulations of anisotropic particles at liquid interfaces. *Computers & Fluids*, 80:184–189, 2013.

[114] Young Joon Choi and Patrick D Anderson. Cahn–Hilliard modeling of particles suspended in two-phase flows. *International Journal for Numerical Methods in Fluids*, 69(5):995–1015, 2012.

[115] Tian-Le Cheng and Yu U Wang. Shape-anisotropic particles at curved fluid interfaces and role of Laplace pressure: A computational study. *Journal of colloid and interface science*, 402:267–278, 2013.

[116] RGM van der Sman and MBJ Meinders. Mesoscale models of dispersions stabilized by surfactants and colloids. *Advances in colloid and interface science*, 211:63–76, 2014.

[117] Yi Sui, Hang Ding, and Peter DM Spelt. Numerical simulations of flows with moving contact lines. *Annual Review of Fluid Mechanics*, 46, 2014.

[118] P Singh and DD Joseph. Fluid dynamics of floating particles. *Journal of Fluid Mechanics*, 530:31–80, 2005.

[119] C Pozrikidis. Particle motion near and inside an interface. *Journal of Fluid Mechanics*, 575:333–357, 2007.

[120] Krassimir D Danov, Rumiana Dimova, and Bernard Pouligny. Viscous drag

of a solid sphere straddling a spherical or flat surface. *Physics of Fluids*, 12(11):2711–2722, 2000.

[121] Anthony JC Ladd. Numerical simulations of particulate suspensions via a discretized boltzmann equation. part 1. theoretical foundation. *Journal of fluid mechanics*, 271:285–309, 1994.

[122] Fabian Jansen and Jens Harting. From bijels to pickering emulsions: A lattice boltzmann study. *Physical Review E*, 83(4):046707, 2011.

[123] Paul C. Millett and Yu U. Wang. Diffuse-interface field approach to modeling arbitrarily-shaped particles at fluid-fluid interfaces. *Journal of Colloid and Interface Science*, 353(1):46 – 51, 2011.

[124] Françoise Fenouillot, Philippe Cassagnau, and J-C Majesté. Uneven distribution of nanoparticles in immiscible fluids: morphology development in polymer blends. *Polymer*, 50(6):1333–1350, 2009.

[125] Lucio Isa, Esther Amstad, Konrad Schwenke, Emanuela Del Gado, Patrick Ilg, Martin Kröger, and Erik Reimhult. Adsorption of core-shell nanoparticles at liquid–liquid interfaces. *Soft Matter*, 7(17):7663–7675, 2011.

[126] Xuan-Cuong Luu, Jing Yu, and Alberto Striolo. Nanoparticles adsorbed at the water/oil interface: coverage and composition effects on structure and diffusion. *Langmuir*, 29(24):7221–7228, 2013.

[127] Konrad Schwenke, Lucio Isa, and Emanuela Del Gado. Assembly of nanoparticles at liquid interfaces: crowding and ordering. *Langmuir*, 30(11):3069–3074, 2014.

[128] L Botto, L Yao, RL Leheny, and KJ Stebe. Capillary bond between rod-like particles and the micromechanics of particle-laden interfaces. *Soft Matter*, 8(18):4971–4979, 2012.

[129] Lu Yao, Lorenzo Botto, Marcello Cavallaro Jr, Blake J Bleier, Valeria Garbin, and Kathleen J Stebe. Near field capillary repulsion. *Soft Matter*, 9(3):779–

786, 2013.

[130] Xuan-Cuong Luu and Alberto Striolo. Ellipsoidal Janus Nanoparticles Assembled at Spherical Oil/Water Interfaces. *The Journal of Physical Chemistry B*, 118(47):13737–13743, 2014.

[131] E Kim, K Stratford, R Adhikari, and ME Cates. Arrest of fluid demixing by nanoparticles: A computer simulation study. *Langmuir*, 24(13):6549–6556, 2008.

[132] Florian Günther, Stefan Frijters, and Jens Harting. Timescales of emulsion formation caused by anisotropic particles. *Soft matter*, 10(27):4977–4989, 2014.

[133] TA Johnson and VC Patel. Flow past a sphere up to a reynolds number of 300. *Journal of Fluid Mechanics*, 378:19–70, 1999.

[134] Rajat Mittal, Haibo Dong, Meliha Bozkurttas, FM Najjar, Abel Vargas, and Alfred von Loebbecke. A versatile sharp interface immersed boundary method for incompressible flows with complex boundaries. *Journal of computational physics*, 227(10):4825–4852, 2008.

[135] Duck-Gyu Lee and Ho-Young Kim. Sinking of small sphere at low reynolds number through interface. *Physics of Fluids*, 23(7):072104, 2011.

[136] Jingzhi Zhu, Long-Qing Chen, Jie Shen, and Veena Tikare. Coarsening kinetics from a variable-mobility cahn-hilliard equation: Application of a semi-implicit fourier spectral method. *Physical Review E*, 60(4):3564, 1999.

[137] Pengtao Yue, Chunfeng Zhou, James J Feng, Carl F Ollivier-Gooch, and Howard H Hu. Phase-field simulations of interfacial dynamics in viscoelastic fluids using finite elements with adaptive meshing. *Journal of Computational Physics*, 219(1):47–67, 2006.

[138] Xavier Chateau and Olivier Pitois. Quasistatic detachment of a sphere from a liquid interface. *Journal of colloid and interface science*, 259(2):346–353,

2003.

[139] SBG O'brien. The meniscus near a small sphere and its relationship to line pinning of contact lines. *Journal of colloid and interface science*, 183(1):51–56, 1996.

[140] Pierre-Gilles De Gennes. Wetting: statics and dynamics. *Reviews of modern physics*, 57(3):827, 1985.

[141] Yutaka Tsuji, Toshihiro Kawaguchi, and Toshitsugu Tanaka. Discrete particle simulation of two-dimensional fluidized bed. *Powder technology*, 77(1):79–87, 1993.

[142] HP Zhu, ZY Zhou, RY Yang, and AB Yu. Discrete particle simulation of particulate systems: theoretical developments. *Chemical Engineering Science*, 62(13):3378–3396, 2007.

[143] Junseok Kim. A continuous surface tension force formulation for diffuse-interface models. *Journal of Computational Physics*, 204(2):784–804, 2005.

[144] Weatherburn CE. On differential invariants in geometry of surfaces, with some applications to mathematical physics. *Quarterly of Pure and Applied Mathematics*, 50:230–269, 1925.

[145] JU Brackbill, Douglas B Kothe, and Charles Zemach. A continuum method for modeling surface tension. *Journal of computational physics*, 100(2):335–354, 1992.

[146] Heng Fan and Alberto Striolo. Nanoparticle effects on the water-oil interfacial tension. *Physical Review E*, 86(5):051610, 2012.

[147] Claudio Canuto, Alfio Quarteroni, M Yousuff Hussaini, and Thomas A Zang. *Fundamentals of Fluid Dynamics*. Springer, 2007.

[148] Matteo Frigo and Steven G Johnson. Fftw: An adaptive software architecture for the fft. In *Acoustics, Speech and Signal Processing, 1998. Proceedings of the 1998 IEEE International Conference on*, volume 3, pages

1381–1384. IEEE, 1998.

[149] Robert Sugden Rogallo. Numerical experiments in homogeneous turbulence. 1981.

[150] Pengtao Yue, Chunfeng Zhou, and James J Feng. Sharp-interface limit of the cahn–hilliard model for moving contact lines. *Journal of Fluid Mechanics*, 645:279–294, 2010.

[151] VV Khatavkar, PD Anderson, and HEH Meijer. On scaling of diffuse–interface models. *Chemical engineering science*, 61(8):2364–2378, 2006.

[152] Pengtao Yue, Chunfeng Zhou, and James J Feng. Spontaneous shrinkage of drops and mass conservation in phase-field simulations. *Journal of Computational Physics*, 223(1):1–9, 2007.

[153] JM Nitsche and GK Batchelor. Break-up of a falling drop containing dispersed particles. *Journal of Fluid Mechanics*, 340:161–175, 1997.

[154] Gunther Machu, Walter Meile, Ludwig C Nitsche, and UWE Schaflinger. Coalescence, torus formation and breakup of sedimenting drops: experiments and computer simulations. *Journal of Fluid Mechanics*, 447:299–336, 2001.

[155] Kyle D Squires and John K Eaton. Particle response and turbulence modification in isotropic turbulence. *Physics of Fluids A: Fluid Dynamics*, 2(7):1191–1203, 1990.

[156] Enrico Calzavarini, Romain Volk, Mickaël Bourgoin, Emmanuel Lévêque, J-F Pinton, and Federico Toschi. Acceleration statistics of finite-sized particles in turbulent flow: the role of faxén forces. *Journal of Fluid Mechanics*, 630:179–189, 2009.

[157] Damian WI Rouson and John K Eaton. On the preferential concentration of solid particles in turbulent channel flow. *Journal of Fluid Mechanics*, 428:149–169, 2001.

[158] Michael P Allen and Dominic J Tildesley. *Computer simulation of liquids*.

Oxford university press, 2017.

[159] Shivshankar Sundaram and Lance R Collins. Numerical considerations in simulating a turbulent suspension of finite-volume particles. *Journal of Computational Physics*, 124(2):337–350, 1996.

[160] GI Taylor. The formation of emulsions in definable fields of flow. *Proceedings of the Royal Society of London. Series A*, 146(858):501–523, 1934.

[161] JM Rallison. The deformation of small viscous drops and bubbles in shear flows. *Annual Review of Fluid Mechanics*, 16(1):45–66, 1984.

[162] Howard A Stone. Dynamics of drop deformation and breakup in viscous fluids. *Annual Review of Fluid Mechanics*, 26(1):65–102, 1994.

[163] Y Rotenberg, Lr Boruvka, and AWilhelm Neumann. Determination of surface tension and contact angle from the shapes of axisymmetric fluid interfaces. *Journal of colloid and interface science*, 93(1):169–183, 1983.

[164] FK Hansen and G Rødsrud. Surface tension by pendant drop: I. a fast standard instrument using computer image analysis. *Journal of colloid and interface science*, 141(1):1–9, 1991.

[165] Clyde E Stauffer. The measurement of surface tension by the pendant drop technique. *The journal of physical chemistry*, 69(6):1933–1938, 1965.

[166] S Fordham. On the calculation of surface tension from measurements of pendant drops. In *Proceedings of the Royal Society of London A: Mathematical, Physical and Engineering Sciences*, volume 194, pages 1–16. The Royal Society, 1948.

[167] Xinfeng Zhang, Hui Sun, and Shihe Yang. Self-limiting Assembly of Two-Dimensional Domains from Graphene Oxide at the Air/Water Interface. *The Journal of Physical Chemistry C*, 116(35):19018–19024, 2012.

[168] Philipp Erni, Huda A Jerri, Kenneth Wong, and Alan Parker. Interfacial viscoelasticity controls buckling, wrinkling and arrest in emulsion drops un-

dergoing mass transfer. *Soft Matter*, 8(26):6958–6967, 2012.

[169] Elodie Aumaitre, Sebastian Knoche, Pietro Cicuta, and Dominic Vella. Wrinkling in the deflation of elastic bubbles. *The European Physical Journal E*, 36(3):1–5, 2013.

[170] Liana Vaccari, Daniel B. Allan, Nima Sharifi-Mood, Aayush R. Singh, Robert L. Leheny, and Kathleen J. Stebe. Films of bacteria at interfaces: three stages of behaviour. *Soft Matter*, 11:6062–6074, 2015.

[171] Theo D Kassuga and Jonathan P Rothstein. Buckling of particle-laden interfaces. *Journal of colloid and interface science*, 448:287–296, 2015.

[172] C Powell, N Fenwick, F Bresme, and N Quirke. Wetting of nanoparticles and nanoparticle arrays. *Colloids and Surfaces A: Physicochemical and Engineering Aspects*, 206(1):241–251, 2002.

[173] Valeria Garbin, Ian Jenkins, Talid Sinno, John C. Crocker, and Kathleen J. Stebe. Interactions and Stress Relaxation in Monolayers of Soft Nanoparticles at Fluid-Fluid Interfaces. *Phys. Rev. Lett.*, 114:108301, Mar 2015.

[174] Olivier Pitois and Xavier Chateau. Small particle at a fluid interface: Effect of contact angle hysteresis on force and work of detachment. *Langmuir*, 18(25):9751–9756, 2002.

[175] N Sinn, M Alishahi, and S Hardt. Detachment of particles and particle clusters from liquid/liquid interfaces. *Journal of colloid and interface science*, 458:62–68, 2015.

[176] Alan J Hurd. The electrostatic interaction between interfacial colloidal particles. *Journal of Physics A: Mathematical and General*, 18(16):L1055, 1985.

[177] A Moncho-Jordá, F Martínez-López, AE González, and R Hidalgo-Alvarez. Role of long-range repulsive interactions in two-dimensional colloidal aggregation: Experiments and simulations. *Langmuir*, 18(24):9183–9191, 2002.

[178] Bum Jun Park, John P Pantina, Eric M Furst, Martin Oettel, Sven Reynaert, and Jan Vermant. Direct measurements of the effects of salt and surfactant on interaction forces between colloidal particles at water-oil interfaces. *Langmuir*, 24(5):1686–1694, 2008.

[179] Mark J Bowick, Luca Giomi, Homin Shin, and Creighton K Thomas. Bubble-raft model for a paraboloidal crystal. *Physical Review E*, 77(2):021602, 2008.

[180] Mark J Bowick and Luca Giomi. Two-dimensional matter: order, curvature and defects. *Advances in Physics*, 58(5):449–563, 2009.

[181] Shi-Yow Lin, Li-Jen Chen, Jia-Wen Xyu, and Wei-Jiunn Wang. An examination on the accuracy of interfacial tension measurement from pendant drop profiles. *Langmuir*, 11(10):4159–4166, 1995.

[182] Bihai Song and Jürgen Springer. Determination of interfacial tension from the profile of a pendant drop using computer-aided image processing: 1. Theoretical. *Journal of colloid and interface science*, 184(1):64–76, 1996.

[183] JF Padday and AR Pitt. The stability of axisymmetric menisci. *Philosophical Transactions of the Royal Society of London A: Mathematical, Physical and Engineering Sciences*, 275(1253):489–528, 1973.

[184] Kevin W Connington, Marc Z Miskin, Taehun Lee, Heinrich M Jaeger, and Jeffrey F Morris. Lattice Boltzmann simulations of particle-laden liquid bridges: Effects of volume fraction and wettability. *International Journal of Multiphase Flow*, 76:32–46, 2015.

[185] Stephen B Pope. Turbulent flows, 2001.

[186] George Marsaglia et al. Choosing a point from the surface of a sphere. *The Annals of Mathematical Statistics*, 43(2):645–646, 1972.

[187] Elodie Aumaitre, Sebastian Knoche, Pietro Cicuta, and Dominic Vella. Wrinkling in the deflation of elastic bubbles. *EPL*, 2012.

[188] Th Von Karman. The buckling of spherical shells by external pressure.

Journal of the Aeronautical Sciences, 7(2):43–50, 1939.

[189] Kenneth Stephenson. *Introduction to circle packing: The theory of discrete analytic functions*. Cambridge University Press, 2005.

[190] Olivier Pitois, Matthieu Buisson, and Xavier Chateau. On the collapse pressure of armored bubbles and drops. *The European Physical Journal E*, 38(5):1–7, 2015.

[191] Norbert Stoop, Romain Lagrange, Denis Terwagne, Pedro M Reis, and Jörn Dunkel. Curvature-induced symmetry breaking determines elastic surface patterns. *Nature materials*, 14(3):337–342, 2015.

[192] TA Witten. Stress focusing in elastic sheets. *Reviews of Modern Physics*, 79(2):643, 2007.

[193] Hunter King, Robert D Schroll, Benny Davidovitch, and Narayanan Menon. Elastic sheet on a liquid drop reveals wrinkling and crumpling as distinct symmetry-breaking instabilities. *Proceedings of the National Academy of Sciences*, 109(25):9716–9720, 2012.

[194] Dominic Vella, José Bico, Arezki Boudaoud, Benoit Roman, and Pedro M Reis. The macroscopic delamination of thin films from elastic substrates. *Proceedings of the National Academy of Sciences*, 106(27):10901–10906, 2009.

[195] Yuri Ebata, Andrew B Croll, and Alfred J Crosby. Wrinkling and strain localizations in polymer thin films. *Soft Matter*, 8(35):9086–9091, 2012.

[196] Evan Hohlfeld and Benny Davidovitch. Sheet on a deformable sphere: Wrinkle patterns suppress curvature-induced delamination. *Physical Review E*, 91(1):012407, 2015.

[197] Chuan Gu and Lorenzo Botto. Direct calculation of anisotropic surface stresses during deformation of a particle-covered drop. *Soft matter*, 12(3):705–716, 2016.

[198] T Kawaguchi, T Tanaka, and Y Tsuji. Numerical simulation of two-dimensional

fluidized beds using the discrete element method (comparison between the two-and three-dimensional models). *Powder technology*, 96(2):129–138, 1998.

[199] MJ Rhodes, XS Wang, M Nguyen, P Stewart, and K Liffman. Use of discrete element method simulation in studying fluidization characteristics: influence of interparticle force. *Chemical Engineering Science*, 56(1):69–76, 2001.

[200] KD Kafui, C Thornton, and MJ Adams. Discrete particle-continuum fluid modelling of gas–solid fluidised beds. *Chemical Engineering Science*, 57(13):2395–2410, 2002.

[201] Rob Tuley, John Shrimpton, Matthew D Jones, Rob Price, Mark Palmer, and Dave Prime. Experimental observations of dry powder inhaler dose fluidisation. *International journal of pharmaceutics*, 358(1-2):238–247, 2008.

[202] S Balachandar. A scaling analysis for point–particle approaches to turbulent multiphase flows. *International Journal of Multiphase Flow*, 35(9):801–810, 2009.

[203] S Balachandar and John K Eaton. Turbulent dispersed multiphase flow. *Annual Review of Fluid Mechanics*, 42:111–133, 2010.

Appendix A

Supporting Information

A.1 Derivation of the Surface Stress Tensor

In analogy to the three-dimensional case [48], the area average of a continuous quantity f at the surface point $\mathbf{x}_s$ can be defined as

$$\langle f \rangle (\mathbf{x}_s) = \int_{\Omega} f(\mathbf{y}_s) G(\mathbf{x}_s - \mathbf{y}_s) dA_{\mathbf{y}_s}. \tag{A.1}$$

Here the surface points $\mathbf{x}_s$ and $\mathbf{y}_s$ belong to the surface Ω (the total surface of the composite interface). The function G is a scalar filter function with compact support in a control region surrounding $\mathbf{x}_s$; G is assumed to be a regular function with suitable properties of smoothness [49, 50]. The filter function is normalised so that $\int_{\Omega} G(\mathbf{x}_s - \mathbf{y}_s) dA_{\mathbf{y}_s} = 1$.

The definition of the surface stress tensor follows from the balance of the forces acting on the particles in the direction tangential to the composite interface. Let $\mathbf{F}_\alpha$ denote the net tangential force acting on a particle located at position $\mathbf{y}_s^\alpha$. From

Equation (A.1), the area-averaged tangential force acting on the particles contained in an area element of particle monolayer centred at $\mathbf{x}_s$ can be expressed as $\langle \mathbf{F} \rangle = \int_\Omega \sum_{\alpha=1}^{N_p} \mathbf{F}_\alpha \delta(\mathbf{y}_s - \mathbf{y}_s^\alpha) G(\mathbf{x}_s - \mathbf{y}_s) dA_{\mathbf{y}_s}$, or equivalently as $\langle \mathbf{F} \rangle = \sum_{\alpha=1}^{N_p} \mathbf{F}_\alpha G(\mathbf{x}_s - \mathbf{y}_s^\alpha)$. The tangential force at a surface point is thus a weighted average of the force acting on the particles surrounding that point, where the weight is given by the filter function evaluated at the centre of each particle.

For pairwise interactions, $\mathbf{F}_\alpha = \mathbf{F}_\alpha^e + \sum_{\beta \neq \alpha} \mathbf{F}_{\alpha\beta}$. Here $\mathbf{F}_\alpha^e$ is the average force due to an external field (e.g. the particle weight) or to particle inertia, and the summation term corresponds to the force on particle α due to lateral inter-particle forces. Substituting this decomposition in the expression for the average force derived above yields

$$\langle \mathbf{F} \rangle = \langle \mathbf{F}^e \rangle + \sum_{\alpha=1}^{N_p} \sum_{\beta \neq \alpha}^{N_p} \mathbf{F}_{\alpha\beta} G(\mathbf{x}_s - \mathbf{y}_s^\alpha). \tag{A.2}$$

Newton's action-reaction principle requires $\mathbf{F}_{\alpha,\beta} = -\mathbf{F}_{\beta,\alpha}$. However, because particles α and β are weighted differently by the filter function according to their location, the forces in the summation term of Equation (A.2) do not cancel out identically. To exploit the symmetry introduced by the action-reaction principle, we perform a Taylor expansion of the filter function about the location of particle α:

$$G(\mathbf{x}_s - \hat{\mathbf{y}}_s^{\alpha\beta}) \simeq G(\mathbf{x}_s - \mathbf{y}_s^\alpha) + \nabla_{\mathbf{y}_s} G(\mathbf{x}_s - \mathbf{y}_s^\alpha) \cdot (\hat{\mathbf{y}}_s^{\alpha\beta} - \mathbf{y}_s^\alpha), \tag{A.3}$$

where $\hat{\mathbf{y}}_s^{\alpha\beta}$ denotes the midpoint between particles α and β. Using this expansion

in Equation (A.2) the inter-particle interaction term can be written as

$$\begin{aligned}\sum_{\alpha=1}^{N_p}\sum_{\beta\neq\alpha}^{N_p}\mathbf{F}_{\alpha\beta}G(\mathbf{x}_s-\mathbf{y}_s^{\alpha}) = &\sum_{\alpha=1}^{N_p}\sum_{\beta\neq\alpha}^{N_p}\mathbf{F}_{\alpha\beta}G(\mathbf{x}_s-\hat{\mathbf{y}}_s^{\alpha\beta}) \\ &-\nabla_{\mathbf{y}_s}\cdot\sum_{\alpha=1}^{N_p}\sum_{\beta\neq\alpha}^{N_p}\mathbf{F}_{\alpha\beta}(\hat{\mathbf{y}}_s^{\alpha\beta}-\mathbf{y}_s^{\alpha})G(\mathbf{x}_s-\mathbf{y}_s^{\alpha}).\end{aligned} \tag{A.4}$$

Since $\hat{\mathbf{y}}_s^{\alpha\beta}=\hat{\mathbf{y}}_s^{\beta\alpha}$, the first double summation on the right-hand side of Equation (A.4) is identically zero. Thus

$$\sum_{\alpha=1}^{N_p}\sum_{\beta\neq\alpha}^{N_p}\mathbf{F}_{\alpha\beta}G(\mathbf{x}_s-\mathbf{y}_s^{\alpha}) = \nabla_{\mathbf{x}_s}\cdot\left[\frac{1}{2}\sum_{\alpha=1}^{N_p}\sum_{\beta\neq\alpha}^{N_p}\mathbf{F}_{\alpha\beta}(\mathbf{y}_s^{\beta}-\mathbf{y}_s^{\alpha})G(\mathbf{x}_s-\mathbf{y}_s^{\alpha})\right], \tag{A.5}$$

where we have used the fact that $\hat{\mathbf{y}}_s^{\alpha\beta}=(\mathbf{y}_s^{\alpha}+\mathbf{y}_s^{\beta})/2$ and $\nabla_{\mathbf{x}_s}=-\nabla_{\mathbf{y}_s}$. The expression in square parenthesis in Equation (A.5) defines the surface stress due to the particles, correct up to the first order in the inter-particle separation.

A.2 Proof of Independence of Surface Pressure on Particle Size for a Linear Inter-Particle Force Relation

For a hexagonal array, the relation between the average inter-particle separation and ϕ_s is

$$l=\left(\frac{2\sqrt{3}\pi a^2}{3\phi_s}\right)^{1/2}. \tag{A.6}$$

Assuming nearest neighbour interactions within hexagonal packing, the packing

energy can be estimated as

$$\begin{aligned} E_p &\simeq N_c N \langle F_{pi} \rangle l \\ &= N_c \frac{4\pi R^2 \phi_s}{\pi a^2} \langle F_{pi} \rangle \left(\frac{2\sqrt{3}\pi a^2}{3\phi_s} \right)^{1/2} \\ &= N_c \frac{12 R^2 \phi_s}{a} \left(\frac{2\sqrt{3}\pi}{3\phi_s} \right)^{1/2} \langle F_{pi} \rangle. \end{aligned} \tag{A.7}$$

The coordination number N_c is independent of a. Therefore $\Pi_s \approx \frac{E_p}{2A} \propto \phi_s^{1/2} \langle F_{pi} \rangle / a$, which proves that Π_s is approximately independent of a when $\langle F_{pi} \rangle \propto a$ for fixed ϕ_s. The linear inter-particle force model (2.14) enjoys this property as it allows to investigate the effects caused by changing only the particle size.

A.3 Equivalence Between Increasing the Spring Constant k_c at Fixed Liquid Volume and Decreasing Liquid Volume at Fixed Spring Constant k_c

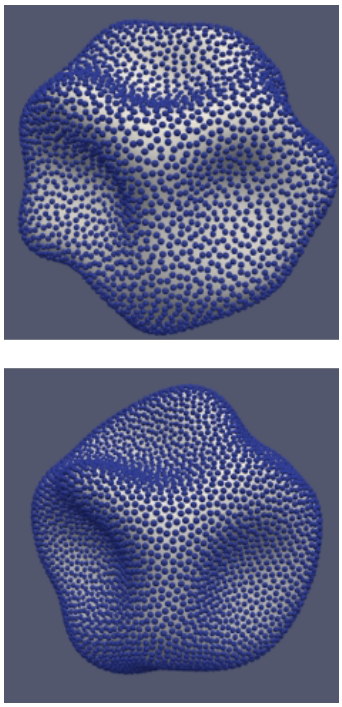

Figure 1.1: Buckled morphology for (TOP) the case in which the spring constant k_c is increased and the volume of the drop is kept constant and (BOTTOM) for the case in which the spring constant k_c is kept fixed and the drop volume is reduced.

In current simulations, changing the volume of the drop at fixed spring constant k_c or increasing k_c for fixed liquid volume leads, qualitatively, to the same results. The reason for this behaviour is that the pressure in an incompressible fluid is a Lagrange multiplier that depends - for a given value of the energy associated to the particle-covered interface - only on the volume of the fluid comprised within the interface. In other words, the value of the pressure across the interface adjusts

itself to the drop volume and the configuration of the particle monolayer with respect to the fluid interface, regardless of whether the drop volume is reduced by keeping the monolayer fixed, or the monolayer area is artificially "expanded" by keeping the volume fixed and increasing the surface pressure.

Figure 1.1 shows snapshots from two simulations. In one simulation (Fig. 1.1 TOP), the volume of the drop is kept fixed and the surface pressure is increased by increasing k_c. In the other, the spring constant is kept constant and the volume of the drop slowly decreased in a quasi-static manner. The essential geometric features of the two buckled morphologies are the same in the two figures. The author do not expect, of course, to obtain identical morphologies, as the buckling instability is highly sensitive to the exact configuration of each particle.